POLITECNICO
MILANO 1863

SCUOLA DI INGEGNERIA INDUSTRIALE
E DELL'INFORMAZIONE

Experimental and numerical analysis of hybrid CFRP/aluminum laminates response under high-velocity impacts

Tesi di Laurea Magistrale in
Aeronautical Engineering - Ingegneria Aeronautica

Author: **Francisco Javier Sanchez Olivera**

Student ID: 958992
Advisor: Prof. Paolo Astori
Co-advisors: Ivan Colamartino, Luca Scampini
Academic Year: 2022-23

Abstract

The following study addresses the high-velocity impact response of fiber-metal laminates, in particular carbon-aluminum laminates. The work was divided into different stages, the first being the characterization of the materials. The following stage was focused on experimental analysis using a pressurized gas gun to impact carbon-reinforced plastic, aluminum, and carbon-aluminum laminates. This stage is dedicated to finding the minimum thickness necessary to stop a spherical projectile shot at 120 m s^{-1}, identifying the failure modes and energy absorption of the laminates.

A numerical analysis in the commercial finite element software LS-Dyna followed where the model of the materials and the impact were built considering the data from the previous phases. Finally, a comparison between the experimental and numerical results was carried out to validate the numerical models.

Keywords: Energy absorption, high-velocity response, fiber-metal laminate, failure modes, spherical projectile.

Abstract in lingua italiana

Il seguente lavoro tratta la risposta all'impatto ad alta velocità dei laminati in fibra-metallo, in particolare i laminati in carbonio-alluminio. Lo studio è diviso in diverse fasi, la prima fase è la caratterizzazione dei materiali. La seguente fase si è focalizzata sull'analisi sperimentale utilizzando una pistola a gas pressurizzata per colpire laminati in plastica rinforzata con carbonio, alluminio e carbonio-alluminio. Questa fase è dedicata a trovare il minimo spessore necessario per fermare un proiettile sferico a 120 m s^{-1}, identificare modalità di guasto e assorbimento di energia dei laminati.

È seguita un'analisi numerica nel software commerciale agli elementi finiti LS-Dyna dove è stato costruito il modello dei materiali e dell'impatto considerando i dati dalle fasi precedenti. Finalmente è stato effettuato un confronto tra i risultati sperimentali e numerici per validare i modelli numerici.

Parole chiave: Assorbimento di energia, risposta ad alta velocità, laminato fibra-metallo, modalità di guasto, proiettile sferico

Acknowledgements

I would like to thank Professor Paolo Astori for all of his guidance, advice, and work throughout this thesis journey. You have been one of the kindest people I have met since coming to Politecnico di Milano and I'm grateful for getting a chance to get to work with you. I would also like to thank Eng. Scampini and Eng. Colamartino for the help through the experimental campaign. Likewise, I would like to thank Eng. Rigamonti, Eng. Rubini, Eng. Monzani and Eng. Ferretti for their crucial role while preparing and manufacturing the specimens used in this work.

I am grateful to my family for their never-ending love and unconditional support throughout my entire academic career, in particular to Marcela, Daniel, and Renée. To my Mom, you have shown me that we can always find light in the middle of the darkness and that we can choose to be gentle in a harsh world. Dad, you are an example of hard work and discipline, thanks for listening to me and giving advice every time I have needed it, you have been my rock and my backbone throughout my life and it is a privilege to be called your son.

To my friends back home Jose Luis, Ingrid, Edahi, Diego, Octavio, and Gamaliel thanks for being such wonderful friends and being for me every time I needed you whether to have fun or some help, you were always there. Zeynep, you have been my best friend and companion through this whole process and I am very thankful for having you in my life. Finally, to my friends/study buddies Osvaldo, Gabriel, Jesus, Daniil, Alam, and Thomas thanks for the moments of joy, the nights filled with problem sets, and the study sessions, we made it.

List of Figures

List of Tables

Nomenclature

Variable	Description	SI Units
A	Cross-sectional Area	m^2
X	Final Strength	MPa
E	Young Modulus	MPa
σ	Stress	MPa
τ	Shear Stress	MPa
G	Shear Modulus	MPa
γ	Shear Strain	
ϵ	Strain	
ν	Poisson Ratio	
ASTM	American Society for Testing and Materials	
FEM	Finite Element Method	
CFRP	Carbon Fiber Reinforced Plastic	
FML	Fiber Metal Laminate	

Contents

1 | Introduction

The intention of this work is to build a numerical model of a carbon-aluminum laminate, determine experimentally the minimum thickness to stop a spheric projectile, and corroborate the numerical model with experimental results. In this chapter, a brief overview of Fiber Metal Laminates (FML) is presented. Firstly, the main characteristics of a FML are presented. Moving on, the objectives and the motivations of the work are discussed.

1.1. Fiber Metal Laminates

In the last decades, the use of composite materials has increased in various structural applications. Especially in the aerospace industry, composites have a preferred role over conventional materials due to their high specific strength, high stiffness, and good fatigue resistance. The rising need of improving the properties of these materials resulted in the creation of a hybrid material made up of thin metal sheets and fiber-reinforced adhesives. FML are composed by alternatively stacking metal and fiber-reinforced composite layers, producing a material that benefits from the characteristics of both materials.

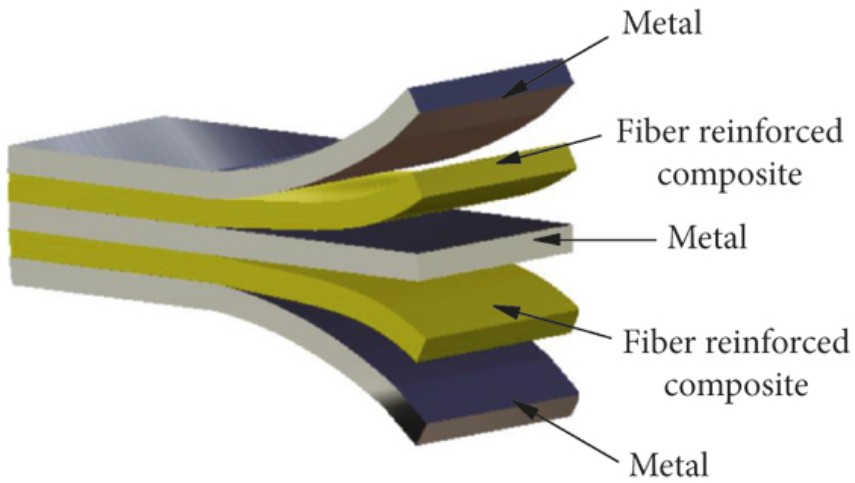

Figure 1.1: FML Composition

The traditional FML configuration is depicted in Figure 1.1. Even though the initial goal of creating FML was to improve the fatigue behavior of composites there are several other advantages compared to their constituents. Some major advantages of FML are: high specific strength, better damage tolerance to fatigue crack growth, fire resistance, blunt notch strength, formability, and repairability [8]. For example, high fatigue resistance is achieved by fiber bridging of fatigue cracks [10]. If a crack has initiated in the aluminum alloy layers, some limited delamination will occur at the interfaces between the metal and the fibers. That will accommodate stress re-distribution from the metal to unbroken fibers in the wake of a crack.

One of the main advantages of the FML is the high energy absorption due to fiber breakage and shear failure in metallic plates, and high impact resistance. The impact response is of particular interest in the aerospace industry, impact damage of aircraft is caused by sources such as runway debris, hail, maintenance damage or dropped tool, collisions between service cars or cargo and the structure, bird strikes, ice from propellers striking the fuselage, engine debris, tire shrapnel from tread separation, tire rupture and ballistic impact [11].

1.2. Objectives

The objectives for the present work are to find the minimum thickness of carbon, aluminum and carbon aluminum laminates to stop a projectile at a high speed, and develop a numerical model of a carbon/aluminum laminate using the commercial software LS-Dyna and data found from experimental testing.

1.3. Motivation

The characteristics of FML under impact loading and the ways to improve their properties to withstand this type of loading could be of particular importance in aerospace structures and other applications. This work develops a numerical model that can help design laminates to withstand high-velocity impacts and gives us an insight into the failure modes and energy absorption mechanisms of FML and their constituents. Also, the following work is planned as a first approach to High-Velocity Impact Response on FML for the LAST Lab at Politecnico di Milano.

2 | State of the Art

In this chapter, a brief overview of the FML history is given, providing the historical background. In addition, the context of the research is established by providing a view of the work done on Carbon-Aluminum (CARAL) laminates, the different studies done on High-Velocity impacts in FML including experimental and numerical approaches, and the latest work done on CARAL laminates.

2.1. Historical Background

During the life of an aircraft, fatigue, corrosion, and incidental (impact) damage can harm the structure. These types of damage have to be considered during the design process for reasons of safety. It is also important for economic reasons because the damage has to be detected and repaired during maintenance. In view of these problems, FML are promising materials.

The origins of the development of FML can be traced back to the bonded plywood wing structure introduced by Anthony Fokker in 1916. By bonding various layers of plywood, he could position the fiber orientation of the wood in the optimal directions for which strength was required. This avoided the problem that a sheet made from one single piece of wood would have its fibers running in only one direction [55]. In 1974 Fokker started work on the fracture toughness of bonded sheet laminated material. The fracture toughness of the laminated material was some 25% larger than for the monolithic material. Fatigue crack growth in laminated sheet material was studied by Schijve et al [51]. in the 1970s. The crack growth rate through the thickness cracks was systematically lower than for monolithic material of the same thickness.

The real breakthrough was introduced in 1978 in the Faculty of Aerospace Engineering at TU Delft: not simply reinforce the adhesive layers, but develop an effective crack-bridging function of the fibers. It then became clear that intensifying crack bridging requires sheet metal layers with a significantly low thickness.

A new hybrid material was obtained by an optimal combination of thin metal sheets with high-strength fiber composite layers: a marriage between two different materials with different properties resulting in a FML combining the best properties of both constituents to combat fatigue, corrosion, and impact. Originally, aramid fibers were used, and so ARALL was created. In Figure 2.1 we can see the cross-section of an ARALL laminate.

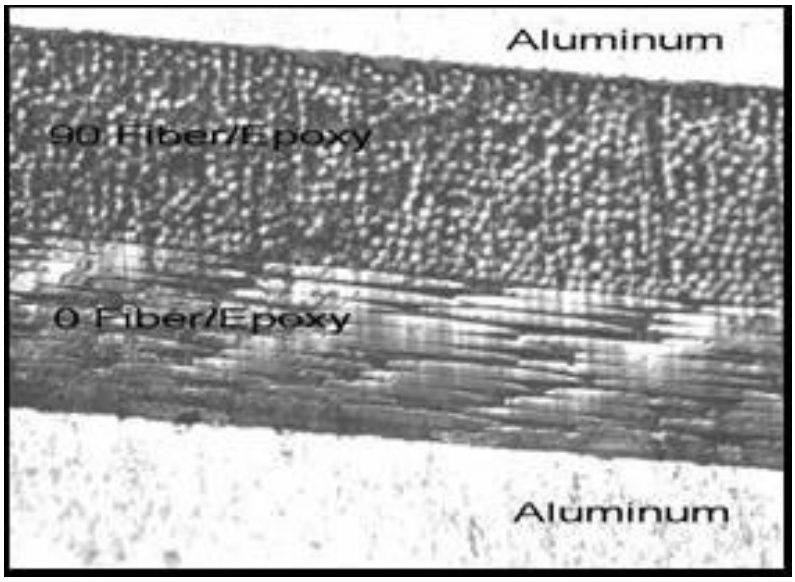

Figure 2.1: FML Cross-Section

The first generation of ARALL was produced by ALCOA and became a mature material that was commercially available. Its promising characteristics were demonstrated by testing a full-scale Fokker 50 wing panel in the mid-1980s. Later, a much stiffer ARALL which consists of carbon fibers instead of aramid fibers, the CARALL Laminates, had been investigated in DUT [52]. Recent research has shown that CARALL laminates also have fiber failure that occurred during flight-simulation fatigue tests at elevated stress levels, which resulted in poor fatigue performance. The limited failure strain of the carbon fibers (0.5–2.0%) was thought to be a disadvantage. Thus, it is sensitive to notch behavior compared to monolithic aluminum alloy. Due to the problem of galvanic corrosion between the carbon fibers and the aluminum sheet in a moisture environment, more research has to be done. In 1987 the second generation of fiber-metal laminates was introduced with the name GLARE [46]. This FML was based on high-strength glass fibers. Where ARALL had unidirectional fiber layers because it was optimized for wing structures, GLARE was developed in both unidirectional variants (GLARE 1 based on Al 7475 and GLARE 2 on Al 2024) and biaxial variants (GLARE 3 based on 2024 with an equal percentage of fibers in 0 and 90 direction, and GLARE 4 with twice the percentage in 0 direction).

The biaxial cross-ply variants were required for the application as a fuselage skin material in view of biaxial stress fields in the pressurized structure. Moreover, glass fibers were introduced because fiber failure was observed in ARALL under cyclic loading at a zero stress ratio (R=0) which is relevant to the fuselage skin. Deutsche Airbus extensively demonstrated the technology of GLARE in 1988/89 in Hamburg by testing an A330/340 fuselage barrel. In the fuselage section crack growth was measured in panels of different aluminum alloys and GLARE. The crack growth rate was significantly slower in GLARE in comparison to crack growth in the aluminum alloy panels.

The first civil applications of GLARE were mainly associated with a better impact damage resistance, which applies to GLARE in the bulk cargo floor of the Airbus A330 and the front bulkhead of the Bombardier Learjet 125. The so-called splicing concept to be discussed later was developed in 1993. It implies that the production of very large panels without joints is possible. The combination of favorable properties makes GLARE an attractive material to be selected for transporting aircraft. The Airbus Consortium has selected GLARE as the material for large parts of the skin of the fuselage of the Airbus 380 [56], as seen in Figure 2.2.

Figure 2.2: GLARE Deployment in the Airbus A380

2.2. High-Velocity Response of FML

2.2.1. Impact Testing

There are several categories of impact loading, and specifically, these are low velocity (large mass), intermediate velocity, high/ballistic velocity (small mass), and hypervelocity impact. These categories of impact loading are important because there are extreme changes in the energy transfer between the projectile and target, energy dissipation, and damage propagation mechanisms as the velocity of the projectile varies [37]. Low-velocity impacts occur at a velocity below 10 m s^{-1}, intermediate impacts occur between 10 m s^{-1} and 50 m s^{-1}, high-velocity (ballistic) impacts have a range of velocity from 50 m s^{-1} to 1000 m s^{-1}, and hypervelocity impacts have a range of 2 km s^{-1} to 5 km s^{-1}. The low-velocity impact response tests are usually done through drop weight tests, where a mass is raised to a certain height and released, impacting the specimen, as seen in Figure 2.3. While in the high-velocity response tests two types of single-stage guns are used, which are powder guns and gas guns. A powder gun uses normal gunpowder as the propellant, and a single-stage light-gas gun uses compressed helium or hydrogen gas as the propellant.

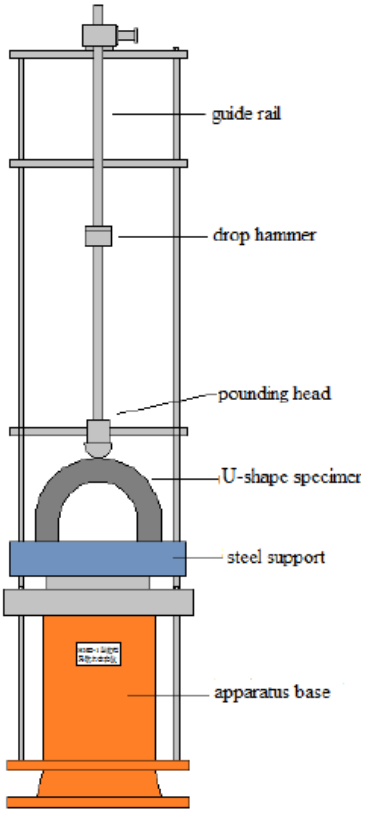

Figure 2.3: Drop Weight Test Apparatus

There are different impact damage criteria for FML, the most commonly used to describe and compare the laminates affected by the impact are the following:

- Maximum permanent deflection (the maximum dent)
- Energy restitution coefficient (for the rebounded projectile, the ratio of the kinetic energy of the impactor after and before impact)
- Minimum cracking energy (the minimum impactor kinetic energy required to cause fiber failure or cracking of the outer aluminum layers)
- Damage width (the diameter of the smallest circle around the damaged area)

2.2.2. Load Displacement Behavior

FML has a force-deflection similar to that of the composites. However, FML exhibit either fiber or aluminum-dominated failure behavior. For the FML with fiber-dominated failure, the first failure occurs at the ultimate load as for monolithic aluminum. Before the first load drop in the force-deflection curve a region of the prepreg layer around the center of the specimen shows some micro-cracking, small cracks in the adhesive. At first failure (the first load drop) the fiber and/or outer aluminum layer will fail. Always when the failure is "fiber dominated" a crack is also found in the outer aluminum layer opposite the loaded side [57]. When an aluminum critical failure occurs a crack will run in the rolling direction irrespective of the fiber direction. If the fibers underneath this layer also run in the rolling direction, they remain intact. After the first failure, the force rises until the ultimate load is reached. At this point, the indenter starts to perforate the specimen. Figure 2.4 shows the force-deflection diagram of a FML.

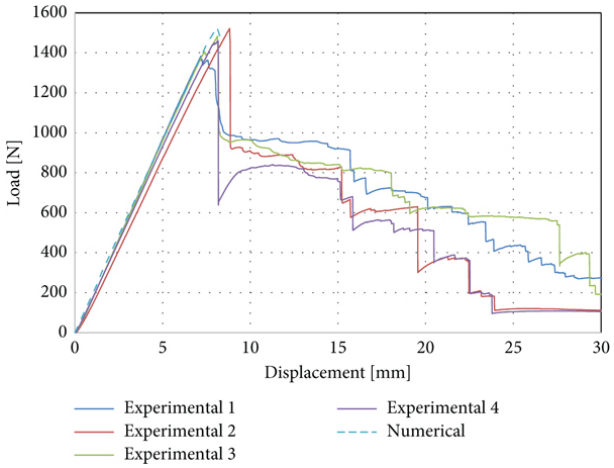

Figure 2.4: Load deflection of FML

2.2.3. Impact Testing Parameters

There are different parameters related to the performance of a FML during impact testing, they can be broadly categorized into two main categories: material and event-related parameters. The material-related parameters are the type of metal, type of fiber, total thickness, type of matrices, layup configuration, volume fraction, and post-stretching [11]. The event-related parameters are specimen geometry, the geometry of the impactor, loading rate, place of impact, and pre-tension.

Material-Related Parameters

The most common fibers applied in the layups of FML are carbon, aramid, and glass. FML are divided into two groups in terms of their failures, "fiber-dominated" and "aluminum-dominated" failures. Aral and Caral are both "fiber dominated", whereas Glare is "fiber" or "aluminum" critical depending on the behavior of glass fiber and the lay-up [2]. In terms of impact damage criteria, it is reported that Caral has significantly lower energy until the first failure than Aral, followed by Glare. However, the type of fibers in FML until the first failure has a small influence on the maximum central deflection, but it has more influence on the permanent deflection after impact. Caral has the highest permanent deflection followed by Glare and Arall. Glare has smaller damage width than Caral and Arall, which depends on their pronounced type of failures.

Two types of aluminum alloys 2024-T3 and 7075-T6 are the main variations used as the metal constituents of FML. 7000 grades of aluminum alloys are stronger and more brittle whereas the 2024 type is more ductile and slightly stiffer. Therefore, the smaller area under the stress-strain curve of Al 7075-T6 compared to Al 2024-T results in considerably lower energy until failure for Al 7075-T6. Smaller deflection, earlier initiation of cracks, and lower delamination of Glare1 due to the high stiffness and strength of 7475-T6 aluminum alloy have been reported. It can be concluded that for Glare the application of 7000 grades of aluminum alloys might lead to a less favorable damage resistance than with Al 2024-T3 [33]. A number of advantages of magnesium alloy over some other alloys, such as low density, improved electromagnetic shielding capability and superior corrosion resistance has been reported by Cortes and Cantwell [15]. It has been reported that Mg-based FML perform significantly better than glass-epoxy/aluminum FML and offer higher specific perforation energy than the comparable aluminum FML with a thermoplastic resin.

Titanium has been proposed as another alternative for the metal constituents in FML. In spite of the suitable fatigue performance of titanium-based FML and improvement in the static strength compared to Glare, the low ductility of the high-strength Ti-alloy caused relatively poor impact properties for the FML [16]. Although, the better performance in the high-velocity impact of Ti-based FML compared to the corresponding carbon fiber-reinforced poly-ether-ether-ketone (CF/PEEK) and glass fiber-reinforced poly-ether-imide (GF/PEI) composites is an advantage, low specific perforation, and first crack energies following the low velocity impact shows that this type of alloy is not suitable as an alternative for better impact resistance of FML.

The first FML for aerospace applications were based on composites with thermosetting polymer matrices, which have higher stiffness and strength, and temperature performance compared to other polymer matrices. Thermoplastic materials offer improved toughness because of somewhat higher energy at first failure and ultimate energy than that of thermosets. Their manufacturing can be more rapid and maybe low-cost [45].

In terms of two types of failure of FML, i.e. "fiber" or "aluminum" critical, Arall and Caral, due to their low strain to failure (2%), irrespective of their lay ups always shows a fiber critical behavior, whereas Glare due to its higher strain to failure (5%), may have both types of failure depending on the lay up of the material [3]. A comparison to assess layup importance was performed between the impact resistance of Glare2 and Glare3 by Liu and Liaw [33] to show the effect of unidirectional fiber orientation of Glare2 and the cross-ply glass epoxy prepregs in the Glare3. It has been shown that Glare3 offers superior impact resistance than that in similar thicknesses of Glare2 due to the use of the cross-ply configuration, having fibers in both directions. As a fact, in composite laminate delamination, will occur between the adjacent plies with different fiber orientations, so cross-ply configuration is expected to have more energy dissipation through the delamination process within composite plies [47]. The higher impact resistance of Glare3 compared to Glare2 was observed since the lower crack length and permanent deflection occurred for similar impact energy levels. Energy may be absorbed through delamination between the bottom aluminum sheet and the lower glass-epoxy ply and within the glass-epoxy, as well as crack initiation and propagation at the non-impacted side. The quasi-isotropic prepreg configuration for FML has better impact damage tolerance than cross-ply prepregs and than UD configuration, which performs the worst, in terms of impact load and crack formation [31]. In Figure 2.5 we can see the effect of different stacking sequences of GLARE while being subjected to impact testing.

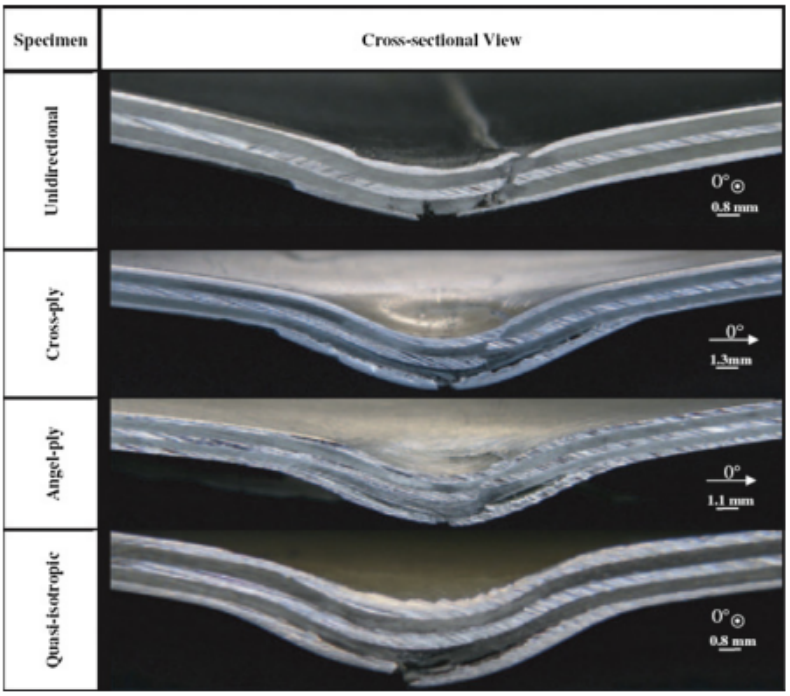

Figure 2.5: Cross-sectional view of Glare with various stacking sequences under impact

During quasi-static loading the stiffness, maximum force, and the perforation resistance increase with the thickness of the composite between metal sheets of FML, whereas the specific perforation decreases [23]. It should be noted that the difference between specific perforation energies of FML and plain composites decreases when the thickness of composite core in FML increases and remains almost constant. Abdolah & Cantwell [9] concluded that replacing a 6.5 mm composite core between two layers of aluminum 2024-T3 results in three times greater perforation energy than that of a system of hose aluminum layers bonded together without reinforced polymer. Increasing the number of composite plies inside the Glare laminates causes smaller damage width, and higher specific first cracking energy in the low-velocity impact and further in high-velocity impact. For a given thickness of an FML, laminates with thicker aluminum plies offer a superior impact resistance to those based on thin plies. However, it has been shown [9] that after a threshold laminate thickness, the normalized perforation energy (perforation energy/Al thickness) begins to fall. It is due to the change in failure mode (thinning to shear) which needs lower perforation energy. It should be noted that the behavior of aluminum will be more dominant in the thinner laminates. Recently, Sadighi et al. [50] who examined metal thickness effects on the impact resistance of FML appreciated that increasing the aluminum thickness improves the impact performance of FML but as it increases the weight, it should be considered where a weight penalty is acceptable.

The maximum permanent deflection is strongly dependent on the thickness of the sheet. For monolithic aluminum and Arall it was found that the energy restitution coefficient is not much dependent on the thickness. This means that the same amount of energy will be stored but that a thicker plate will have a smaller permanent deflection [2]. As it is expected, the maximum force, the initial slope of load-displacement curves, and the perforation resistance increase for GLARE with increasing the plate thickness whereas the specific perforation energy is roughly constant over the range of thickness considered [1]. Influences of thickness on the low-velocity impact of Glare5 FML were examined experimentally by Seyed Yaghobi et al. [53]. They reported that failure modes change by increasing the panel thickness. Two types of behavior, fiber critical and aluminum critical were observed depending on the thickness of the laminate. For Glare 5 (2/1) after debonding, aluminum failure occurred, whereas, for Glare 5(3/2), the major failure type was debonding in the non-impacted side followed by fiber breakage and splitting and aluminum layers fracture. When panel thickness increases, i.e. for Glare 5(5/4) and (6/5), delamination occurred near the impacted side at relatively lower impact energies.

The only article related to the post-stretching of FML and its effect on the impact behavior is published by Vlot [2]. Depending on the post-stretch strain applied, post-stretching causes initial tensile stress in the fibers and therefore causes lower energy absorption and reduction of the first failure energy. ARALL specimens were tested at different percentages of post-stretching. It was found that the post-strength percentage did not influence the maximum central deflection, the maximum force during impact, and the crack length after the first failure due to impact; but the perforation energy decreases with increasing post-stretch percentage.

Event-Related Parameters

Increasing the size of the target results in decreasing the initial slope of the load-displacement curve and reducing the maximum impact load. Also, perforation energy increases due to the reduced flexural stiffness in the larger diameter panels and increasing of elastic and plastic energy dissipation [23]. A work from Carrillo and Cantwell [13] focused on the scaling of the low-velocity response of FML, has dealt with the configuration of the laminate through two approaches, one called ‘ply-level’ scaling, where the thickness of each ply is scaled, and in other approach named ‘sub-laminate-level’ scaling, a simple sub laminate was repeated. Experiments elucidated that the low-velocity impact phenomena of FML obey almost a simple scaling law.

Severe damage around the impact site is induced by small indenters during drop-weight impact on Glare2 and 3 and energy dissipated through local damage (fracture, delamination, and plastic dent). Whereas indenters with a diameter beyond 25.4 mm caused no considerable local damage and more energy was absorbed through global deformation. In general, the maximum impact force, maximum deflection, and perforation energy of the FML increase significantly with increasing projectile diameter [13]. Two impactor geometries, i.e. hemispherical and flat were applied by Compston and Cantwell [14] for high-velocity impact on polypropylene-based FML. Both energies at the perforation threshold and the specific perforation energy for the flat nose impactor are higher than for the hemispherical impactor. It should be noted that the mode of failure for the perforation of the aluminum sheet by hemispherical is associated with high plastic deformation and tensile crack on the back side, whereas a disc-shaped plug out caused by shear failure is visible after perforation with less plastic deformation by flat projectile resulted in lower perforation energy. However, for FML specimens, the flat nose projectile produces larger fracture areas which causes more energy for perforation.

Kashfi et al. [35] researched the effect of the projectile nose on the ballistic response of FML. Blunt, hemispherical, and conical-nosed projectiles are considered to study the high-velocity impact behavior, as seen in Fig. 2.6. The obtained results reveal that the ballistic limit of FML for the conical-nosed projectile was higher than the blunt and hemispherical-nosed projectiles by 83.08% and 35.23%, respectively.

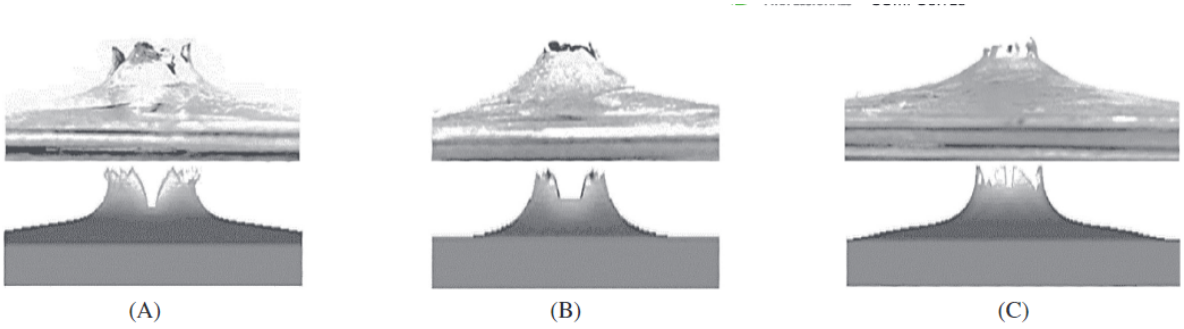

Figure 2.6: Comparison of experimental deformation with FE for (A) conical, (B) hemispherical and (C) blunt-nosed projectiles

An experimental observation [2] shows that the variation of impact locations from the center to the corner or along the edges does not have any significant effect on the perforation energy of the FML. Vlot's work [2] investigated pre-tension on aluminum alloys (2024-T3 and 7075-T6) and the corresponding Arall3/2 specimens containing these alloys while the tensile stresses applied to the specimens before impact varied between 0 and 350 MPa.

In general, he observed that the maximum central deflections and the contact time decrease with increasing pre-load; whereas the maximum impact force increases during elastic impact tests (lower energy). For higher impact energies (plastic impact tests), the influence of pre-tension on the force-time and force-displacement curves of the Arall is higher than for aluminum. With increasing the pre-stress, cracking takes place sooner and a significant rise in the crack length occurs at high pre-stresses.

2.3. Failure Modes of FML

The failure of FML is mainly caused by the accumulation of damage. The failure modes mainly include fiber-resin matrix debonding, fiber fracture, resin matrix crack propagation, metal layer/fiber layer interlaminar delamination, and metal fracture failure [63]. When materials are used in aircraft or automobile structures, they are often subjected to complex stress conditions such as axial stress, bending stress, shear stress, and impact stress. For example, when extrusion occurs between parts or temperature changes greatly, FML are often subjected to tensile stress or compressive stress. When an airplane or a car is strongly impacted, the structure often needs to bear huge shear stress and bending stress.

During high-velocity impact, first at lower impact energies, the failure in the FML starts with a top surface dent and a localized crack parallel to the rolling direction at the back surface aluminum layer. By increasing the impact energy, the length of the rear surface crack and the size of the top surface dent increase up to the stage of perforation threshold which usually results in a clean hole and a limited petalling at the rear surface of the FML. A thinning process around the point of impact occurs due to membrane stretching and yielding in the aluminum plies during impact.

The proportions of the energy dissipating through a high-velocity impact on Glare have been estimated by Hoo Fat et al. with their analytical model [29]. According to their results, the deformation energy due to bending and membrane accounts for 84% to 92 % of the total absorbed energy, having in mind that thinner panels absorb a higher percentage of deformation than thicker panels. 2% to 9% of the total energy absorbed is due to the delamination energy with the fact that the thinner panels absorb a lower percentage of delamination energy than the thicker panels. The tensile fracture portion of energy dissipation is about 7%. These findings emphasize the use of thinner panels that would allow energy absorption in the membrane stretching.

An important observation during low- and high-velocity impact on FML relates to the event of debonding between lower aluminum ply and the adjacent composite ply, which may happen during high-velocity impact. This is believed to be responsible for higher energy absorption and further perforation resistance of FML during high-velocity impact. The bond between the prepregs and aluminium layer is a point of weakness during high velocity impact whereas, at low-velocity impact, the composite-metal adhesion remains impressive under the loading.

Langdon et al. [30] studied panels loaded locally or uniformly distributed and the results have been reported for thin and thick laminates, where thick panels contained proportionally more composite layers. Localized loading results in membrane deformation due to a relatively high proportion of aluminum layers within the laminate as well as dominated shaped damage in the thinner panel. The thicker panel undergoes back-face debonding, both in terms of overall back-face displacement and debonded area without much membrane action. In Figure 2.7 it is seen the failure modes of FML under axial compression.

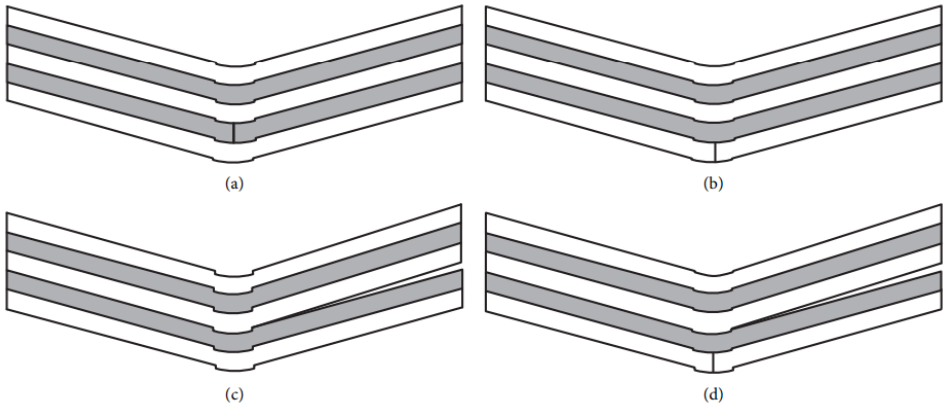

Figure 2.7: Failure of FML under bending stress. (a) Fiber layer failure; (b) metal layer failure; (c) interlaminar shear failure; (d) mixed damage.

The interlaminar shear strength refers to the bonding strength between fibers and the matrix resin in FML. The interlaminar shear strength of composites is closely related to the interlaminar bonding quality of materials [44]. When the shear stress is greater than the maximum interlaminar shear stress, the composite material will be damaged or fail [48]. The interface of the FML is extremely sensitive to shear stress, and one of the most typical failure mechanisms of laminar composites is debonding delamination. The interlaminar shear strength of the FML can be effectively improved by surface treatment of the metal and adjustment of different layer designs. Since the fiber/resin interface and the metal/resin interface were closely related, the interface between the surface-treated metal and the resin had excellent adhesion.

He et al. [41] found that the samples after anodizing, annealing, and primer treatment were superior to the original samples in terms of shear strength and specific elongation. Goushegir et al. [49] tested aluminum-based laminates after different surface treatments, such as mechanical grinding, sandblasting, acid pickling, conversion coating, and electrochemical pretreatment. The results showed that all surface pretreatments increased the interlaminar shear strength of FML.

Under the bending stress, the laminate is subjected to both normal stress and shear stress. Therefore, the failure mode is more complicated, and the changes in structure and layer design will affect the failure behavior of the material [26]. Under bending stress, the failure of the FML mainly manifests as the failure of the fiber layer and metal layer under normal stress, interlaminar shear failure, and mixed failure under normal stress and shear stress. The interlaminar failure behavior of FML was considerably affected by ply angle. The longitudinal fibers in FML increase the bending stiffness and strength. Good interlaminar bonding strength can also improve failure behavior under bending stress. Xu et al. [62] found that there were two ways to improve the bonding strength between the metal layer and the fiber layer. The first method was to make surface treatment on the metal before preparation to remove dirt on the metal surface and loosen the surface oxide film to increase surface roughness. The second method was to use adhesive [42] to improve the bond strength between metal and prepreg.

Under the longitudinal tensile stress, failure behaviors of the laminate were shown as resin matrix cracking, fiber breakage, fiber/resin interfacial debonding, and so forth [18].Sharma et al. [5] prepared FML with metal layers placed at different locations along the thickness and evaluated its tensile response through tensile testing. They found that the failure modes of unidirectional laminates include fiber breakage, metal breakage, and necking. However, when it came to orthogonal laminate, mixed failure including fiber layer delamination, fiber breakage, and metal breakage may occur. Under the compressive stress, the test found that FML would buckle. First, the metal layer buckled in the same direction.

Under the shear stress, the resin deformed, and the metal/fiber layer interface began to delaminate [43]. After buckling, local deformation would cause matrix interlaminar and intraply failure forms such as matrix failure, fiber failure, delamination, and debonding. In the study of the tensile properties of the GLARE laminate, some scholars concluded that, due to the strength difference between fiber and metal in the transverse and longitudinal directions, the tensile property would be reduced in both directions. +e decrease of tensile property would aggravate the possibility of tensile failure.

However, when the glass fiber was used for bidirectional reinforcement, the tensile property of the GLARE laminate in both the transverse and longitudinal directions would increase, and the degree of improvement was related to the fiber content. Thermal cycling can also improve the tensile property of FML. Khalili et al. studied the effect of thermal cycling on the tensile property of FML.In Figure 2.8 it can be seen the different failure modes under axial compression.

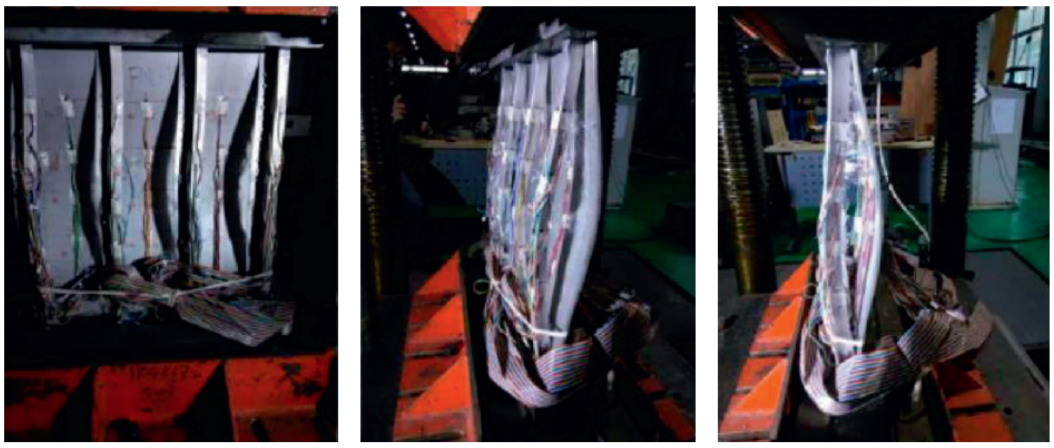

Figure 2.8: Destruction of fiber metal materials under axial compression stress. (a) Skin buckling, (b) long buckling, and (c) overall instability of the siding

Since most composite materials are brittle, they can only absorb energy during the elastic deformation. Therefore, under the condition of no plastic deformation, the low-velocity impact damage is concealed, but it may cause the overall failure of the structural members as the damage accumulates [25]. Under the low-velocity impact stress, the failure modes of FML include metal layer cracking, fiber layer fracture, and interfacial debonding [39]. The interfacial debonding under the impact stress generally includes debonding between different fiber layers and debonding between the fiber layer and the metal layer.

High-velocity impact can lead to complete failure of the FML and even lead to penetration [58]. Chen et al. found that as the impact velocity increased, the damage area of the GLARE laminate gradually increased. Under ballistic impact, GLARE laminates mainly release absorbed impact energy through plastic deformation, metal cracking, debonding, and fiber breakage. The way GLARE laminates are damaged is related to the initial velocity of the bullet, including metal cracking, brittle fracture of the fibers, and damaged areas. At the same time, the failure mode of GLARE laminates under impact stress is also significantly affected by constraints. For example, the ballistic limit velocity of the GLARE laminates impacted at the corner of the plate was found to be much less than that impacted at the middle location of the plate [60].

The impact resistance property of the FML is related to the thickness of the laminate, the fiber diameter, and the ply angle. In a comprehensive study of the low-velocity impact response of GLARE laminates, Morinie‘re et al. concluded that as the number of layers increased, the metal volume fraction decreased gradually, and the specific absorption of the laminates was gradually increased [21]. It indicates that the fiber layer plays an important role in improving the specific absorption energy of the laminate. However, due to the different structures of the laminate, the thickness cannot be adjusted at will. Therefore, changing the ply angle is still the first choice to control the impact failure defects [6]. The treatment of the metal surface also improves the impact resistance of the material. Bahari-Sambran et al. [20] studied the effect of adding surface-modified nanoclay on the mechanical behavior of basalt fiber-epoxy resin/aluminum laminate composites. They found that the addition of clay gave FML higher impact strength. This may be due to the improved interlaminar property.

2.4. Numerical Models of FML

There is a limited number of articles discussing the FEM model of FML. For example, Alkhatib et al [19] use LS dyna models, the material model 058 used for composite fabric materials is used for plates and 010 elastoplastic hydrodynamic material is used for the bullet, as seen in Figure 2.9. For contacts between layers, the surface to surface tiebreak is found to model the adhesion between the metallic and composite plies, and surface-to-surface for bullet and composite interfaces. The FEM shows that the main dissipation is due to matrix cracking, delamination, fiber debonding, and fiber breakage.

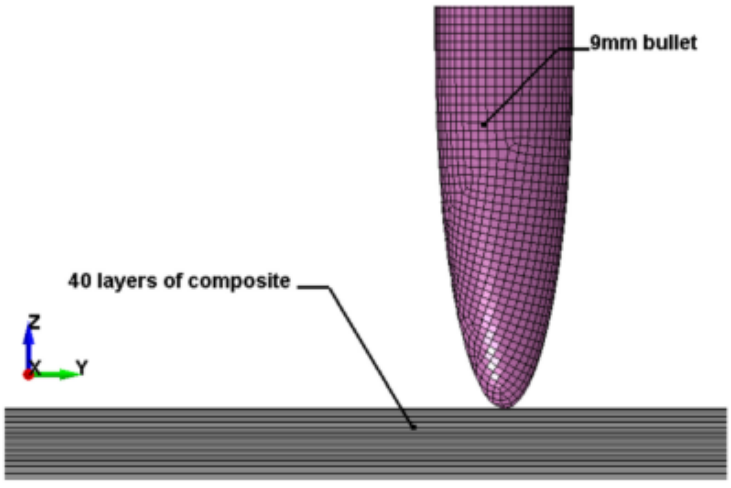

Figure 2.9: Section view of FEM bullet and laminate

In another paper, Chen et al. [61] compared the energy dissipation between magnesium and aluminum-based FML. In this paper the impactor was made of high-strength steel, of which the stiffness was much larger than that of FML specimens, the impactor was discretized as a rigid body. Both the aluminum and composite layers of the FML specimens were modeled with deformable hexahedral solid elements (C3D8R), except for some six pyramidal solid elements for mesh transition, as seen in Figure 2.10. The 0.001 mm-thickness cohesive layers were established by COH3D8 cohesive elements at the metal-composite interface, cohesive elements bond plies together, and contact between the plies must be considered after cohesive elements fail and are deleted. The results of the paper show that the impact energy of the FML was mostly dissipated by metal layers, where the plastic dissipation energy of each aluminum layer in aluminum-based FML was distinctly higher than that of the magnesium layer in magnesium-based FML. Replacing aluminum in FML with magnesium leads to faster perforation and passive energy dissipation, but will also reduce delamination damage at the metal-composite interface due to smaller plastic deformation.

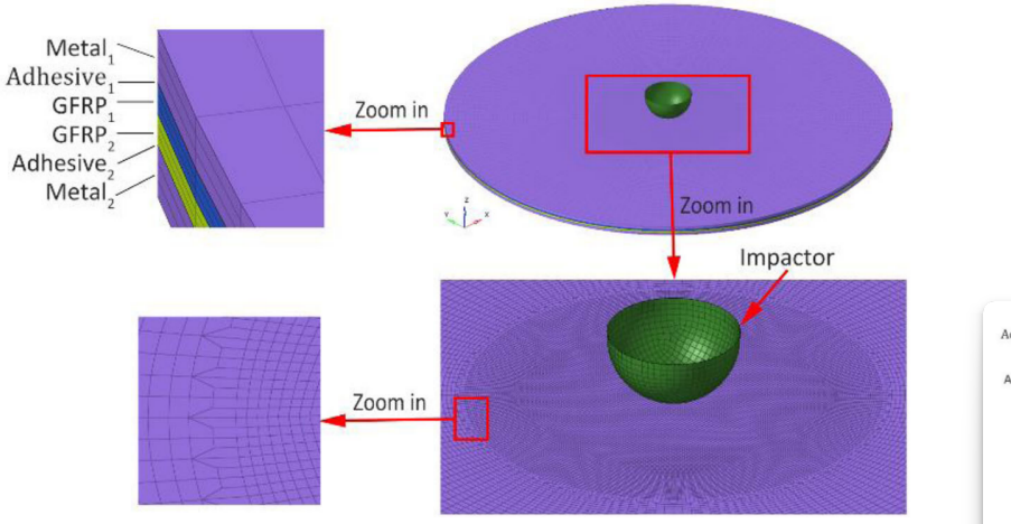

Figure 2.10: Finite element model of FML specimen under impact.

Tarafdar et al. [7] studied the low-velocity impact test energy absorption capacity of GLARE. In the FEM model, different through-thickness integration points were used, with no boundary conditions but two surfaces under compression with controlled displacements. Aluminum is considered as piecewise linear plasticity. For the crush behavior on the composite tubes, the material used was an enhanced composite damage material. Failure criteria based on tensile and compressive fiber failure and matrix failure, when reached elastic constants reduce to zero. Failure introduced with DFAILT, DFAILC, and DFAILM.

Unusual distortion requires a lot of hourglass energy and more computational time. Contacts are defined as an automatic single surface for each shell to prevent self-penetration, the automatic surface-to-surface to stimulate interaction between tube and rigid plate, and automatic surface-to-surface tiebreak for the interaction and bonding between two adjacent composite layers.

Due to symmetric boundary conditions, we can model a part of the model but to show accurate failure mechanisms a complete model was simulated. Results show the energy absorption of metal through plastic folding and composite through catastrophic failure, avoided by efficient design, and progressive crushing. Diamond deformation for aluminum, splaying, longitudinal crack, lamina bundle, and fibers breakage for GFRP. In general, demanding load cases and absorbed energy is better with aluminum included while cost-effective and lightweight structures with higher stroke efficiency. Corrections were needed in software for slow velocity numerical results since micro-level failure mechanisms were not considered. In Figure 2.11 the mesh of the components for the GLARE are presented.

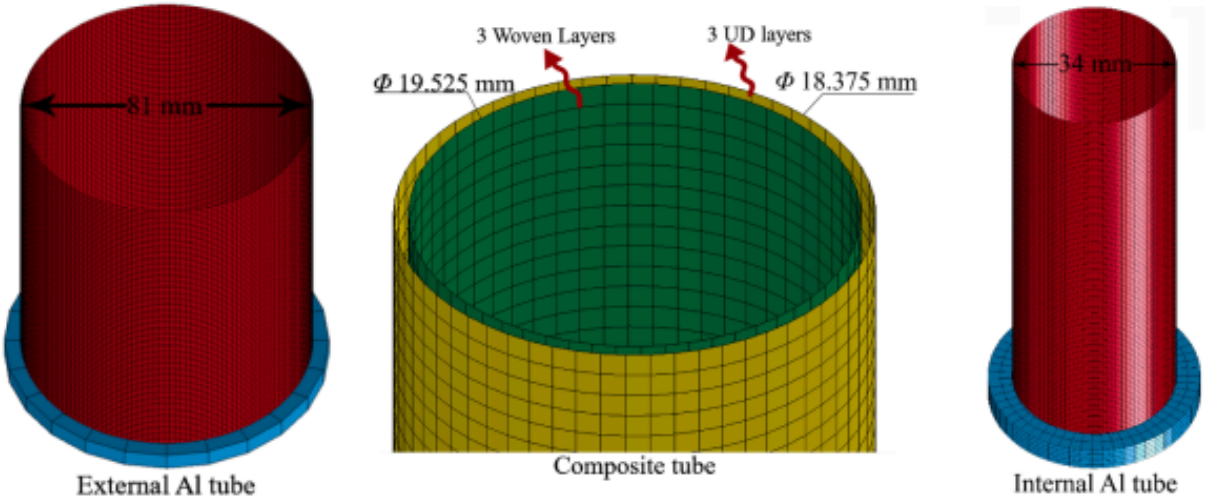

Figure 2.11: Simulated aluminum and composite tubes under quasi-static compression loading.

3 | Methodology and Experimental Analysis

In this chapter, the methodology of the work and the experimental activities developed are presented. The methodology is explained in detail from the manufacturing of the laminates to the properties of the materials, the testing rig design, impactor selection, model construction, and impact tests.

3.1. Methodology

The main scope of this thesis is to set up an appropriate FEM to simulate the impact of a spheric steel projectile against a plate based in an aluminum-carbon laminate; the plate may represent protection for both automotive (road debris) or aerospace vehicle (runway or space debris). The second is to find an efficient protective system in terms of impact energy per unit mass. The first step is to perform a literature review in order to find meaningful information to develop the work. The impact speed is set at around 120 m s^{-1}, it is considered a threshold to find penetration in laminates with similar dimensions as the one proposed for this study.

The projectile shape is considered spheric to simplify the manufacturing and to avoid possible sensitivity to the projectile's attitude, while the mass is set at a range between 20-25 grams since high-velocity impact papers consider small impactors to find localized failure and penetration. The materials chosen for this work were carbon and aluminum, considering they are a good match, have not been deeply studied in the literature, and lab staff has had experience with this kind of laminate before. The dimensions of both the impacted surface and the thickness are similar to the ones found in the literature, this will help in terms of result comparison in terms of failure modes and energy absorption.

A clamping system must be devised for the testing rig, as the existing frame used for prior impact tests is insufficient to mount the specimen with the dimensions specified in the literature (100mm x 100mm x 2.8mm), the new clamping system can be seen in Figure 3.1. In addition to centering the shot, a sabot is required to propel the projectile through the barrel, acting as an interface between the gun and the bullet. This sabot also serves the purpose of centering the shot.

Figure 3.1: Mounted clamping system.

After the material selection, a series of characterization tests take place. For the composite material, the tests include tension, compression, and shear tests according to the standards, while for the aluminum only tensile tests were necessary. For the FML level, only interlaminar tests were considered, in particular the double cantilever beam test and three-point bending test. To start to characterize the impact behavior some initial shots are done at the aluminum and composite impact specimens. Once the model is reliable enough in terms of energy absorption, the speed is fixed, and the most optimal solution in terms of thickness and weight is searched between the constituents and FML.

3.2. Manufacturing

This section will outline the essential procedures for preparing the materials needed to carry out the experimental activity.

3.2.1. Sabot

To develop the sabot the first step is to prepare a geometry in a computer-aided design (CAD). The basis for the design is the shape of the bullet and the inner diameter of the gas gun, also a minimum thickness of 5 mm between the bullet and the back of the sabot is necessary in order to withstand the high pressure at the back face. The design is developed using SOLIDWORKS and can be seen in Figure 3.2.

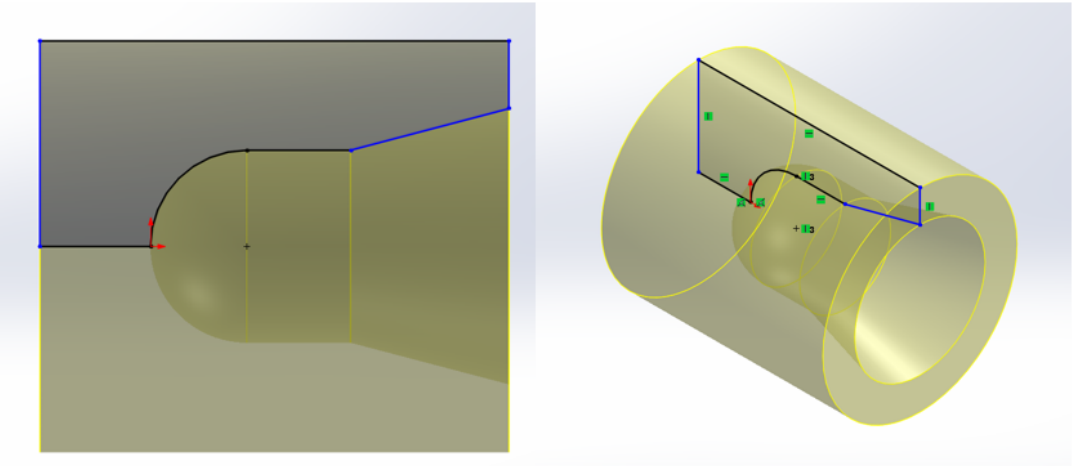

Figure 3.2: CAD of the sabot.

Following this, the gcode file required by the 3D printer is prepared using 3D printing software, specifically Ultimaker Cura. To ensure compatibility with the specific 3D printer in use, a basic set of settings must be selected. The next step involves importing an STL file from SOLIDWORKS, which describes the surface of the sabot, after which the appropriate gcode settings are chosen. In order to slice the 3D part into individual layers, various basic settings such as infill, bed temperature, printing temperature, and printing speed are required. The infill, which is a measure of the density of the inner part of the 3D object, affects the mechanical properties of the finished part; the lower the infill, the lower the mechanical properties. Printing and bed temperature are determined by the material used, with polylactic acid (PLA) being the most commonly used due to its low melting point, high strength, low thermal expansion, good layer adhesion, and high heat resistance.

The material used for this case is tough PLA, a stronger version of PLA that can resist the high pressure exerted by the gas gun. Once the gcode with the desired settings is ready, it is saved and exported into the 3D printer. Cleaning and adding an adhesive to the printer plate are highly recommended to get the correct adhesion of the piece. In Figure 3.3 we can see the nozzle of the 3D printer used to prepare the sabots.

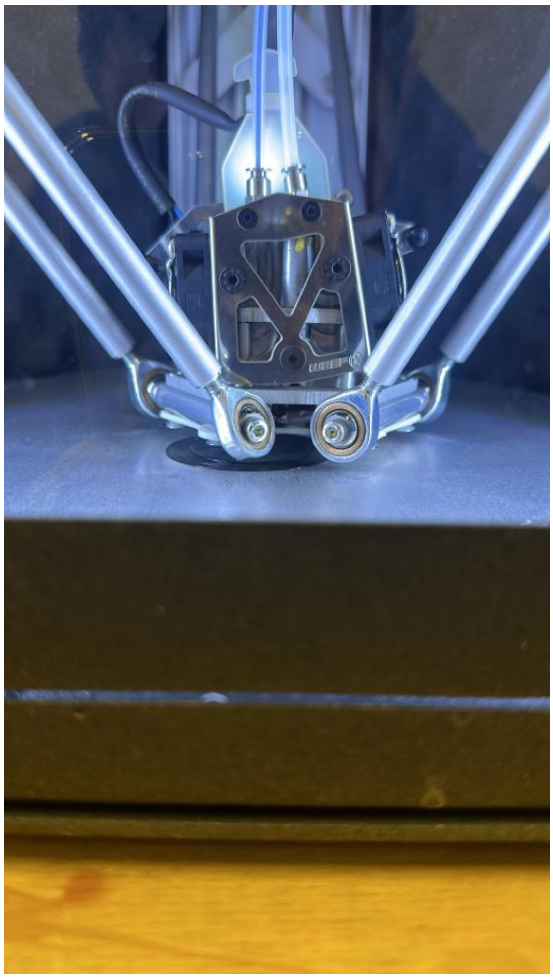

Figure 3.3: Nozzle printing the sabot.

Upon testing the PLA sabots by firing projectiles, it was discovered that the original design was insufficient, as the sabot was destroyed at the cannon's stopper. This caused parts of the sabot to be expelled from the cannon, thereby contaminating the data intended to measure the bullet's speed and impact. To improve the sabot's structural reliability, the tip's shape was modified, and the infill was significantly increased in a second attempt. Although this resulted in a better shot, some material still appeared on the shot. A final iteration was conducted by switching to Nylon material, which produced an optimal behavior and resulted in a clean shot.

In Figure 3.4 it is seen the destroyed PLA sabot and how it contaminates the capture of the camera and we can see the comparison between a shot Nylon and a tough PLA sabot.

Figure 3.4: Top: Shot contaminated with destroyed PLA. Bottom: Comparison between two shot sabots, Nylon on the left and PLA on the right.

3.2.2. Carbon Specimens

The procedure for creating both the characterization and impact specimens is identical, differing only in their geometry. The dimensions of the characterization specimens vary depending on the relevant standard, with the tension and shear specimens being longer (250 x 25 x 2.5 mm) than those for the compressive module (150 x 25 x 2.5 mm) and compressive strength (75 x 25 x 2.5 mm). Conversely, the impact specimens have a fixed length of 120 x 120 mm, with the thickness varying to examine its effects during testing.

The carbon fiber reinforced fabric used was chosen to be a woven material for convenience in the layup, the sensibility to an error of assembly, and the assumptions that can be made between longitudinal and transversal behavior. HexTow® AS4 carbon fiber is a continuous, high strength, high strain, PAN based fiber available in 3,000 (3K) filament count tows. This fiber has been surface treated and can be sized to improve its interlaminar shear properties, handling characteristics, and structural properties.

HexPly® M79 is a formulated epoxy resin matrix, specially designed for prepreg applications where cure temperature is low. It cures from temperatures as low as 70°C. The matrix is highly tolerant to a wide variety of production techniques and process conditions. The material's properties are listed in Table 3.1.

Type of yarn	HexTow® AS4C GP 3K
Nominal weight	200 gr/mm^2
Weave style	Twill 2/2
Nominal cure ply thickness	0.2 mm
Matrix	M79 epoxy resin
Resin percent volume	42%

Table 3.1: Woven material characteristics

To properly characterize the material, it is essential to produce coupons for testing purposes. This is done by performing a plain lamination of a known thickness, following ASTM norms. After curing, the required geometry is obtained by cutting the coupons from the lamination. To conduct a tensile test, the lamination is prepared with the same fiber orientation (0°) for both tension and compression. For an in-plane shear test, a separate lamination is performed with a 45° fiber orientation.

To ensure consistent mechanical pressure on both the internal and external laminations of FML during polymerization, the vacuum-assisted bag molding (VABM) method is employed, using an aluminum plate as the mold. This method utilizes a sealed plastic bag that is depressurized to compact all of the lamination layers. Thermocouple sensors are attached to the bag to monitor the temperature of the component inside the autoclave during the curing process, as seen in Figure 3.5.

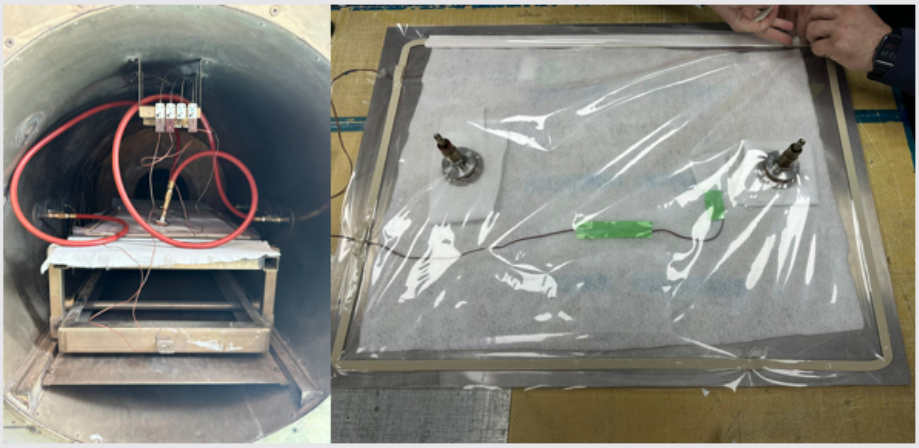

Figure 3.5: Vacuum Bag Manufacturing of Specimens

The initial stage of specimen preparation involves cutting the required number of plies to achieve the desired thickness and applying pressure with a thin plate to obtain a uniform finish. Peel-ply tissue is then placed on both the top and bottom sides of the fabric sheets to etch the surface, creating a stronger adhesion zone for attaching the GFRP tabs to the coupons after the curing process. The component is then enclosed in a plastic bag and sealed with butyl tape. Valves are placed inside the bag to apply vacuum pressure and compress the lamination.

After placing the vacuum bag in the autoclave and connecting all the necessary valves and sensors, the curing cycle commences. The laminated component is subjected to pressure, gradually increasing in tandem with the temperature until it reaches the resin glass temperature, allowing the matrix to polymerize. As the matrix cools, it becomes rigid and provides structural support to the fibers. During the temperature increase, the resin's viscosity in the prepregs decreases, and the external pressure applied to the laminate compresses the layers, resulting in improved adhesion between the elements. The curing cycle parameters are based on the recommendations provided by the prepregs manufacturing company for the M79 epoxy resin and are presented in Table 3.2.

Heat-up rate	1°C/min
Cure temperature	80°C
Cure time	360 min
Pressure gauge vacuum	0.9 bar
Pressure autoclave	3.0 bar

Table 3.2: Typical M79 epoxy cure cycle by HexPly ®

Regarding the production of impact specimens, the dimensions of the specimens are 120x120 mm, of which 100x100 mm are for the test rig aperture, and the remaining 20x20 mm are used for clamping the specimens. As previously mentioned, quasi-isotropic laminates are ideal for energy absorption. Due to the symmetric nature of the woven material, a single ply can be used for 0°-90°, and another ply for ±45°. Table 3.3 displays the layup configurations utilized for the impact specimens.

Test ID	Thick $[mm]$	Total Layers	0°-90° plies	±45° plies	Layup
1IC	2.5	12	6	6	$[0\text{-}45\text{-}0\text{-}45\text{-}0\text{-}45]_s$
2IC	4	20	10	10	$[0\text{-}45\text{-}0\text{-}45\text{-}0\text{-}45\text{-}0\text{-}45\text{-}0\text{-}45]_s$
3IC	5.3	24	12	12	$[0\text{-}45\text{-}0\text{-}45\text{-}0\text{-}45]_2s$
4IC	7.2	36	18	18	$[0\text{-}45\text{-}0\text{-}45\text{-}0\text{-}45]_3s$
5IC	8.8	40	20	20	$[0\text{-}45\text{-}0\text{-}45\text{-}0\text{-}45\text{-}0\text{-}45\text{-}0\text{-}45]_2s$
6IC	10.5	48	24	24	$[0\text{-}45\text{-}0\text{-}45\text{-}0\text{-}45]_4s$

Table 3.3: Layup of Impact Carbon Composites

3.2.3. Aluminum Specimens

The material selected to use as the metallic constituent is an aerospace grade aluminum, in particular 2017 aluminum in the T4 temper. This aluminum is solution heat-treated and naturally aged. It has the highest ductility compared to the other 2017 variants, this is important since ductility is important in FML in order to produce the desired failure modes and deformation along the panel. The material was purchased from Profital Spa, in the shape of four plates of 1000 by 2000 mm with varying thicknesses of 0.5, 2.5, 4.5, and 5 mm.

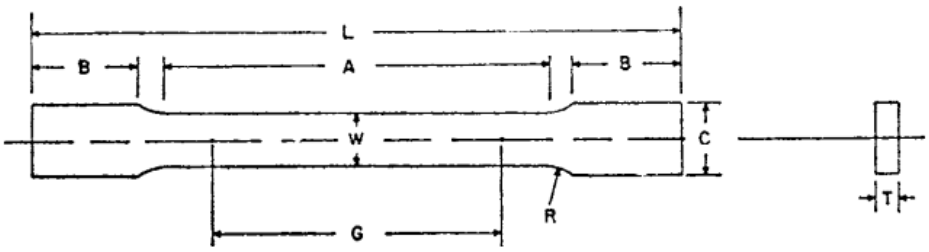

Figure 3.6: Standard sheet-type test specimen.

There were two kinds of specimens developed, the first to characterize the material and the second to perform the impact tests. For the impact specimens, the dimensions are fixed to 120X120 mm, so they can be fixed in the testing section. Considering aluminum is an isotropic material, a single test is enough to characterize it, the ASTM E8M tensile test standard is used for this purpose. In Figure 3.6 and Table 3.4, the geometry for the characterization specimens is shown.

G-Gauge Length	50
W-Width	12.5
T-Thickness	2.5
R-Radius fillet	25
L-Overall Length	200
A-Length of Reduced Section	80
B-Length of Grip Section	50
C-Width of Grip Section	20

Table 3.4: Dimensions in mm of Plate-Type Specimens

3.2.4. FML Specimens

Producing FML specimens is similar to fabricating composite specimens, with the primary fabrication method being vacuum-assisted bag molding. However, there are additional steps involved. In order to ensure proper adhesion between the composite laminate and aluminum, an adhesive layer is utilized. Specifically, a structural thermo-setting adhesive film called 3M Scotch-Weld® is used for both solid panel and honeycomb sandwich constructions. To facilitate proper adhesion between the adhesive film and the aluminum, sandblasting treatment is applied to the aluminum plates. This not only cleans the plates but also provides a rough surface finish that aids in attaching the adhesive, as depicted in Figure 3.7.

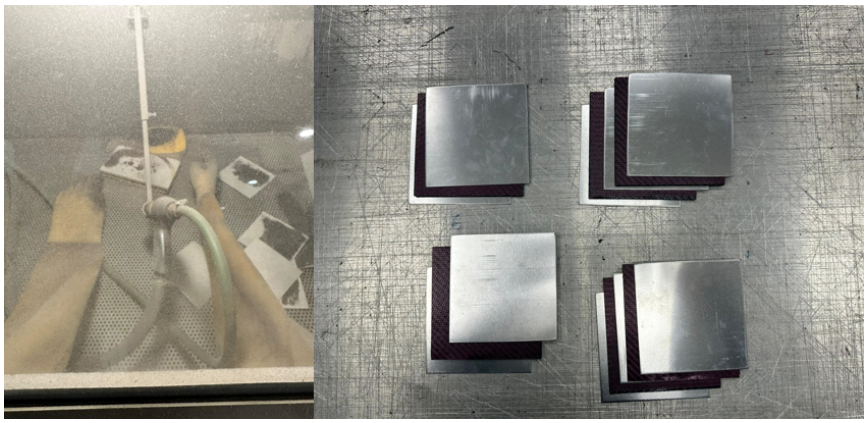

Figure 3.7: Left: Sandblasting treatment for the aluminum plates. Right: FML Lamination sequences.

The maximum thickness of aluminum plates for FML specimens is limited by the failure mechanism of thin aluminum plates. While some papers mention a limit of up to 8 mm, for our purposes, we use plates that are 5 mm thick. According to the literature, thicker aluminum plates would lead to shear failure and fail to distribute the load effectively along the composite layer. Table 3.5 shows the lamination sequence of the FML.

ID	Thick [mm]	AL layers	0°-90° plies	±45° plies	Layup
1IFML	2.7	2	4	4	$[\text{AL-0-45-0-45}]_s$
2IFML	5	2	9	9	$[\text{AL-45-0-45-0-45-0-45-0-45}]_s$
3IFML	6.5	2	12	12	$[\text{AL-0-45-0-45-0-45-0-45-0-45-0-45}]_s$
4IFML	3.5	3	4	4	$[\text{AL-0-45-0-45-0.5 AL}]_s$
5IFML	5	3	8	8	$[\text{AL-0-45-0-45-0-45-0-45-0.5 AL}]_s$
6IFML	8.5	3	16	16	$[\text{AL-}[\text{0-45-0-45-0-45-0-45}]_s$ -AL-$[\text{0-45-0-45-0-45-0-45}]_s$-AL]

Table 3.5: Layup of Impact Carbon Composites

3.3. Carbon Characterization

Material characterization refers to the determination of material properties through tests conducted on a specimen. In these characterization tests the main properties of the materials as young modulus or maximum stress were computed, with the goal of applying these properties to the numerical model.

3.3.1. Tensile Characterization

The standard used to get the tensile properties on a composite coupon is the ASTM D3039 [54], this test method determines the in-plane tensile properties of polymer matrix composite materials reinforced by high-modulus fibers. According to the standard, it is necessary to apply tabs on the coupon tips to transfer the load from the wedge grips of the tensile test machine to the specimen itself, thus reducing stress concentrations and protecting the specimen.

In Table 3.6, we can see the summary of the dimensions of the specimens in terms of width, thickness, and cross-sectional area, which are important to compute the materials' properties.

Specimen ID	Width (mm)	Thick (mm)	Area (mm^2)
1T	2.91	24.87	72.28
2T	2.88	24.75	71.37
3T	2.83	24.90	70.55
4T	2.92	24.90	72.62
5T	2.90	24.88	72.16

Table 3.6: Dimensions of tensile specimens

To get a more precise measurement of the stress-strain relationship, the specimens are tested with a dual grid biaxial strain gauge (KYOWA® KFGS-3-350-D16-11). The bi-axial configuration is needed to compute the Poisson's ratio during the deformation. One last step before testing is to glue the sensors at the half length of the specimen. The strain gauges placed in the specimens are presented in Figure 3.8.

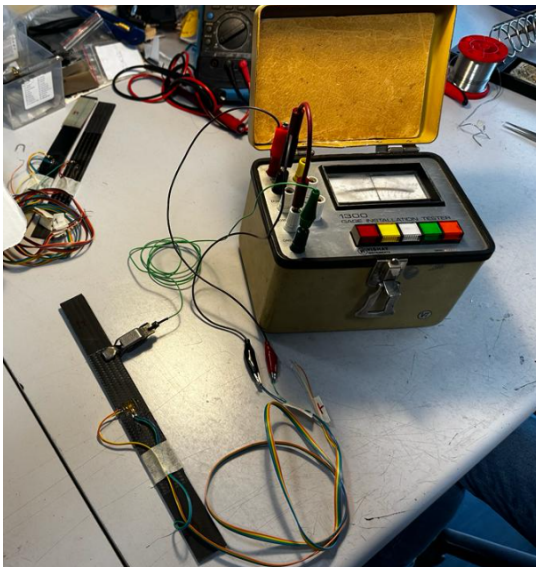

Figure 3.8: Tension specimens with strain gauges in place

The tests were performed on MTS 810 Material Testing Systems. The machine has the capability of measuring applied load and crosshead displacement. Moreover, to the afore-mentioned biaxial strain gauges, a single-axis extensometer MTS 634.11F-54 is applied. Extensometers are less common in composite tests than strain gages. The test configuration is the one presented in Figure 3.9.

As stated earlier, the material characteristic of symmetric fabric laminate can be considered equal in the in-plane directions. In addition, the limit load strengths can be approximately equal $X_1^T \approx X_2^T$. While the shear strength X_S is quite small as it is governed by the matrix. X_1^T is the limit force at which the laminate brakes under tensile loading in the x_1 direction. Considering the latest assumption, the tensile tests are performed only for 0° fiber direction, assumed equal to the response in the 90° orientations.

From the tensile tests, the three main mechanical properties that need to be computed are the young modulus (E), Poisson ratio (ν), and the tensile strength (X_1^T) from the maximum axial stress (σ_x). To minimize the potential effects of bending it is recommended that the strain data used for modulus of elasticity and the Poisson ratio determination be computed in the initial elastic range between 1000 to 3000 micro-strains in the axial direction.

Figure 3.9: Tension specimens with strain gauges and extensometer in place

$$E_x = \frac{\Delta\epsilon_x}{\Delta\sigma_x} \tag{3.1}$$

$$\sigma_i = \frac{P_i}{A} \tag{3.2}$$

$$\nu_{xy} = -\frac{\Delta\epsilon_y}{\Delta\epsilon_x} \tag{3.3}$$

The subscripts "x" and "y" refer to the axial and transverse directions of a test specimen, P is the load in the axial direction (applied by the test machine) and A is the cross-sectional area of the specimen. The failure mode is also critical to check if the test was done correctly, the standards mention that data obtained from specimens that fracture outside the gage should be used with caution as this data may not be representative of the material. Failure in the grip region indicates the stress concentration at the tab is greater than the natural strength variation of the material in the gage section. Below the results from the tensile tests are presented in Table 3.7 and Figure 3.10.

Specimen ID	X_1^T $[MPa]$	ϵ_x^T	ν_{xy}	E_x $[GPa]$
1T	727.635	0.01526	0.1823	51.774
2T	732.168	0.01169	0.0385	63.970
3T	735.795	-	0.0685	66.881
4T	740.978	0.01211	0.0067	58.635
5T	747.171	0.01371	0.0417	59.132
Average	739.028	0.01319	0.0496	62.154
SD	5.648	0.0014	0.01343	3.433
CV	0.76%	10.7%	27.09%	5.52%

Table 3.7: Results from Tensile Tests

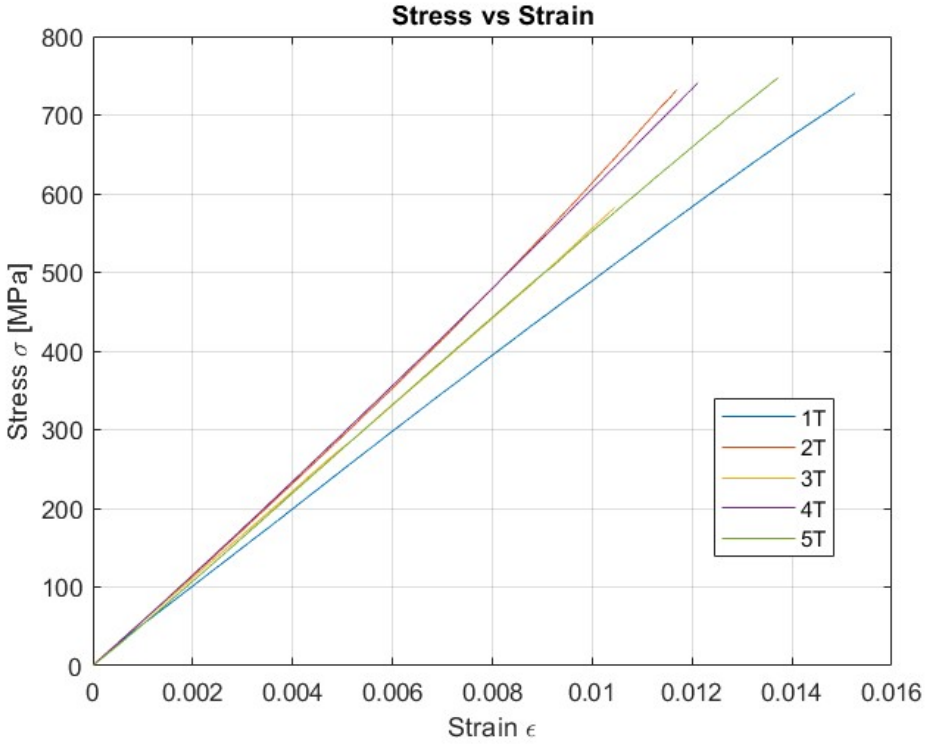

Figure 3.10: Stress-strain curve of the tensile test

Table 3.7 provides us with the values for SD (standard deviation) and CD (coefficient of variation). It's worth noting that one specimen's results were excluded due to failure at the tabs, and the standard allows for such results to be used in this failure mode (as outlined in Appendix A). The stress-strain curve is based on the four most representative specimens, as depicted in the plot.

3.3.2. Shear Characterization

The standard to compute the shear properties of a composite coupon is the ASTM D3518, this test method determines the in-plane shear response of polymer matrix composite materials reinforced by high-modulus fibers. The state of stress in each lamina of the 45° laminate is not pure shear. Each lamina contains tensile normal stresses, σ_1 and σ_2, in addition to the desired shear stress, τ_{12}. Moreover, interlaminar shear stress, τ_{23}, is present near the laminate-free edge. Normally, this consideration could be neglected, and the stress state approximated, making the tensile shear test method an appropriate and simple test for determining the shear modulus and strength of the ply.

The main mechanical properties computed from the experiments are the shear strength X_S from the maximum shear stress τ_{12}, shear strain ϵ_{12} and shear modulus G_{12}. Some considerations have to be considered for these properties, first, the in-plane shear modulus, G_{12}, is readily determined by plotting τ_{12} vs ϵ_{12} and establishing the slope of the initial portion of the curve. The regulation suggests G_{12} evaluation over a range of 2000÷6000 micro-strain in shear strain. Also if the ultimate failure does not occur within 5 % shear strain, the data shall be truncated to the 5 % shear strain mark. The results of the shear tests are presented in Table 3.8 and Figure 3.11.

Specimen ID	X_S $[MPa]$	G_{12} $[MPa]$
10	66.739	3529.649
11	63.917	3574.084
12	65.981	3588.388
13	69.711	3832.186
14	65.098	3872.207
Average	66.289	3679.303
SD	2.078	143.051
CV	3%	4%

Table 3.8: Results from Shear Tests

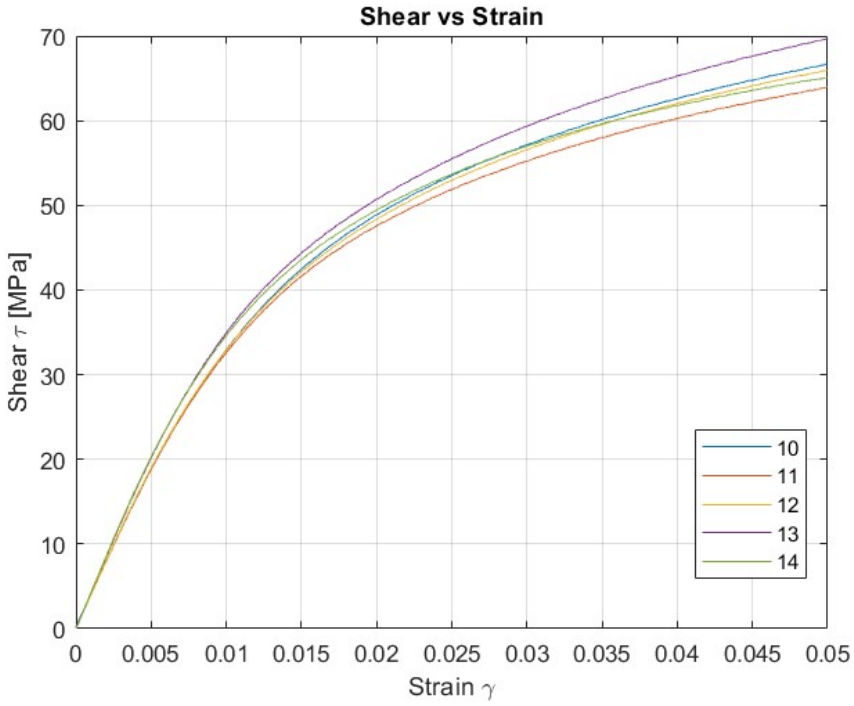

Figure 3.11: Shear stress-shear strain curves

In this series of tests, all the coupons were considered since all of them have the desired failure (fiber breakage) as seen in Appendix A.

3.3.3. Compression Characterization

To obtain the compressive properties of polymer matrix composite materials reinforced by high-modulus fibers, the ASTM D3410 test method is employed. This test method is specifically designed to determine the in-plane compressive properties of such materials. The calculation of compressive properties is similar to that of a tensile test, but there are two key differences in the testing process. The first difference is the length of the specimen being tested, and the second is the direction of load application. The results of the compressive tests are presented in Table 3.9 and Figure 3.12 below. Due to testing limitations, two separate tests were performed: one to obtain the compressive modulus (E_c) and another to determine the maximum compressive stress (X_1^C).

Specimen ID	E_c [GPa]	Specimen ID	X_1^C [MPa]
1C	62.294	11C	-538.435
2C	58.590	12C	-479.432
3C	60.370	13C	-509.925
4C	68.725	14C	-429.200
5C	58.11	15C	-492.647
Average	61.618	**Average**	-489.928
SD	3.847	**SD**	36.216
CV	6.240%	**CV**	7.390%

Table 3.9: Results from Compression Tests

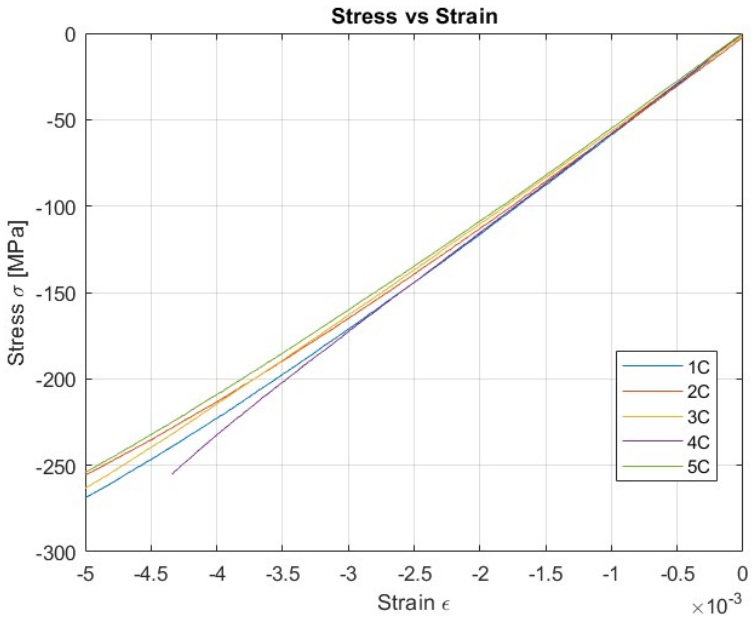

Figure 3.12: Compression stress-strain curves

Appendix A displays the failure modes of the compression coupons, with all but one coupon failing due to compressive failure of the fibers. The single remaining coupon failed due to a delamination issue that occurred during the manufacturing process. Although standards suggest ignoring this data, we chose to include all results as the level of scattering was insignificant.

3.4. Aluminum Characterization

The properties required to model aluminum in LS Dyna are the Young Modulus, density, yield stress, ultimate tensile stress and plastic strain of failure. The standard used for the aluminum characterization is the ASTM E8M, the test methods cover the tension testing of metallic materials in any form at room temperature, specifically, the methods of determination of yield strength, yield point elongation, tensile strength, elongation, and reduction of area.

The Young modulus can be computed as it was with the composite material. The Young Modulus has to be computed with the slope of the stress-strain curves before yielding, in the elastic range. To determine the yield strength by the offset method, it is necessary to secure data from which a stress-strain diagram may be drawn. Then on the stress-strain diagram lay off Om equal to the specified value of the offset, draw mn parallel to OA, and thus locate r, the intersection of mn with the stress-strain diagram, as seen in Figure 3.13. Finally, the plastic strain leading to failure is calculated by subtracting the region of elastic strain from the strain at the point of breakage.

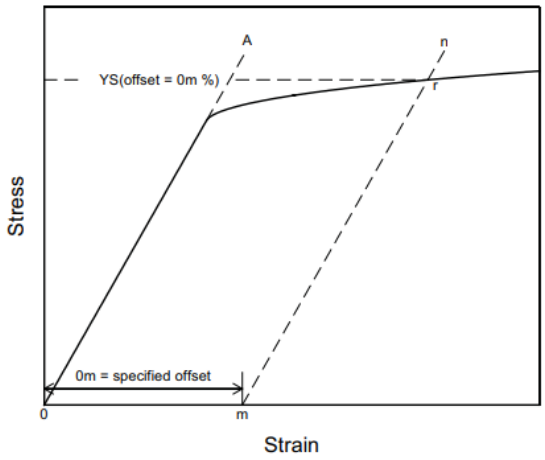

Figure 3.13: Stress-Strain Diagram for Determination of Yield Strength by the Offset Method

Table 3.10 presents a summary of the width, thickness, and cross-sectional area of the aluminum specimens, which are essential parameters for calculating the materials' properties.

Specimen ID	Width (mm)	Thick (mm)	Area (mm^2)
1A	2.51	12.45	31.21
2A	2.51	12.40	31.13
3A	2.47	12.46	30.83
4A	2.52	12.49	31.47
5A	2.49	12.39	30.94

Table 3.10: Dimensions of aluminum specimens

As there are no significant variations in the Poisson ratio for aluminum compositions, the strain gauge was not a focus of interest in this experiment. Since aluminum possesses high strength, the specimens were fixed to the test rig without a tabbed interface, unlike composites that may suffer from delamination. As anticipated, the specimens underwent ductile failure during all tests, as evidenced in Appendix B. The test data was utilized to compute the material properties, which are presented in Table 3.11. The Young modulus, yield stress, ultimate tensile stress, and plastic strain to failure are the listed properties. The stress-strain curves for Aluminum 2017 T4 are depicted in Figure 3.14.

Specimen ID	E $[GPa]$	σ_f $[MPa]$	σ_y $[MPa]$	ϵ_{pf}
1A	71.86	430.03	338.24	0.169
2A	71.55	430.98	336.83	0.207
3A	72.88	433.58	330.07	0.158
4A	72.57	426.36	333.67	0.201
5A	72.65	433.73	334.21	0.182
Average	72.30	430.94	334.2	0.1835
SD	0.51	2.70	2.71	0.0183
CV	0.70%	0.62%	0.81%	9.98%

Table 3.11: Results from Aluminum Tests

3.5. High-Velocity Impact Set-Up

The high-velocity testing apparatus comprises a gas gun, test specimen support, tested specimens, lights to ensure sufficient illumination for the high-speed camera, and the high-speed camera itself, as depicted in Figure 3.15. Prior to firing the cannon, the tip must be removed and the previous sabot replaced with a new one at the opposite end. A foil is used to ensure that the sabots are fired at the intended pressure level, and a lever is manually operated to create a hole and allow the pressurized air to pass through at the desired velocity.

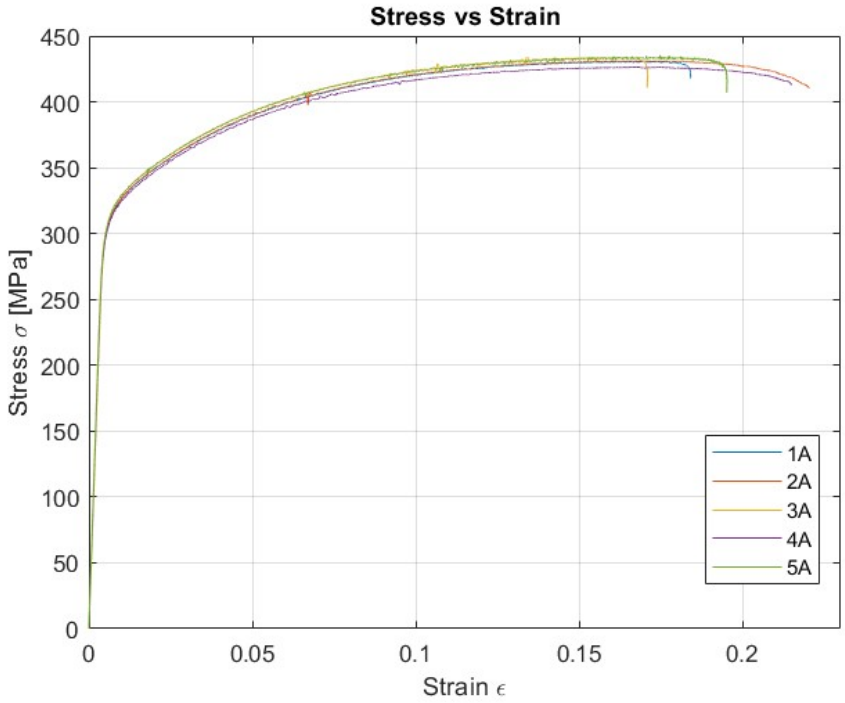

Figure 3.14: Stress-Strain Diagram for Aluminum 2017

The foil needs to be replaced after each shot. The specimen is mounted in the apparatus shown in Figure 3.1, and the torque applied to the clamping system is crucial, as excessive pressure on the composite specimens could result in delamination. The torque threshold is determined by finding the maximum torque applicable to M8 bolts and halving it. This torque is then verified using a dynamometer and applied to all tests. The camera is positioned above the test rig and must be adjusted properly to ensure the projectile can be identified within the testing area.

A series of shots were taken with varying air pressures to determine the threshold needed to achieve the desired speed of the projectile when shooting the specimens. The values for different masses of sabots and air pressures are presented in Table 3.12. The desired speed of the projectile was fixed at around 120 m s^{-1}.

Air Pressure (bar)	Sabot Material	Mass (gr)	Speed of projectile (m s^{-1})
2.2	Carbon	60	134
1.2	Nylon	74	85
1.4	Nylon	74	103
2	Nylon	74	122

Table 3.12: Results from Shooting Tests

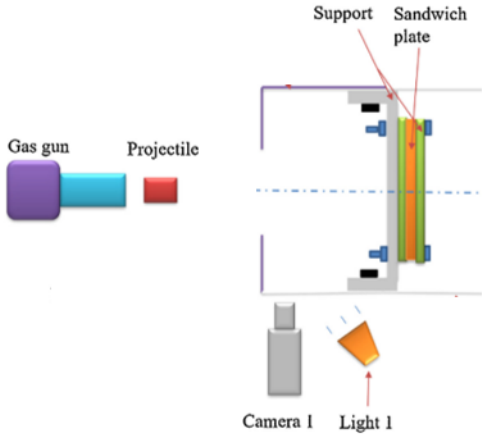

Figure 3.15: High-Velocity Testing Diagram

Formula 3.4 is used to determine the constant energy level at which the panels are struck, taking into account both the mass of the 24-gram steel ball projectiles and their velocity of 120 m s^{-1}. To assess the impact resistance of various laminates, this study employs specific energy-absorption parameters that account for both the weight and thickness of the panels.

These parameters are defined in Formulas 3.5 and 3.6. The m in Formula 3.5 stands for the mass of the laminate, A area of the impacted surface, and the t in Formula 3.6 stands for the thickness of the laminate. Formula 3.7 shows the formula to compute the absorbed energy of each panel, making reference to the impact and the residual kinetic energy of the projectile.

$$KE = \frac{1}{2} * mv^2 \tag{3.4}$$

$$SEAM = \frac{KE}{m} \tag{3.5}$$

$$SEAT = \frac{KE}{t} \tag{3.6}$$

$$AbsE = KE_{impact} - KE_{residual} \tag{3.7}$$

3.6. Aluminum High-Velocity Response

The failure of metals usually initiates at the time of the contact, with local heating arising in the impact region as a result of intense plastic shear deformation. This heat is generated so quickly that the effects of conduction are negligible; hence, the process can be considered adiabatic. As a result, thermal softening occurs in the impact region while the surrounding material continues to harden. When the load increases, the local region deforms more than the surrounding material, and narrow adiabatic shear bands are formed. While these bands do not deteriorate the material as cracks do, they are precursors to fracture. Typically, nucleation, growth, and coalescence, and/or cracks may appear in the shear bands when the impact load exceeds the local material strength. The failure process of a high impact velocity problem will then occur in two stages: local heating in the impact region leading to the development of adiabatic shear bands and ductile rupture in the shear bands [24].

The process of determining the minimum thickness required to stop the bullet begins by testing progressively thicker materials, starting from the thinnest available. Eventually, a thickness of 2.5 mm is found to effectively stop the projectile. Due to insufficient information to model the specific material, various speeds are examined using the 2.5 mm thickness.

Using LS-DYNA, a numerical model is developed to replicate these findings by establishing a threshold at which the specimens fail. In Table 3.13, the test results are presented in columns as follows: test id, specimen thickness, impact speed of the projectile, output speed, energy absorbed by the laminate, and residual energy of the bullet. Results of the shooting campaign, reveal a highly non-linear phenomenon once the threshold speed for each specimen is exceeded. The LS-DYNA model will primarily concentrate on reproducing the outcomes within the range of threshold velocities, aiming to closely match the observed results.

Test ID	Thick [mm]	Mass [gr]	In V [ms^{-1}]	Out V [ms^{-1}]	Abs E [J]	Res E [J]
1IA	0.5	20	50	0	27.5	Rebound
2IA	0.5	20	101	68	61.34	50.8
3IA	0.5	20	118	100	40.5	110
4IA	2.5	100	103	0	116.7	Rebound
5IA	2.5	100	122	3	163.6	0.1
6IA	2.5	100	144	13	226.4	1.69
7IA	2.5	100	165	96	198.105	101.37

Table 3.13: Results from Aluminum Impact Tests

Additionally, a comparison of fracture mechanisms between thin and thick aluminum plates reveals notable differences. Thin plates exhibit a more ductile failure mode, allowing the material to absorb more energy by deforming a larger surface area. Conversely, thicker specimens experience a more sudden and shear failure, resulting in less energy absorption and localized deformations. Figure 3.16 illustrates the energy absorption mechanisms in thin and thick specimens, depicting their behavior both prior to and following perforation.

Figure 3.16: Impacted specimens. Left: Thin specimens. Right: Thick specimens.

To facilitate a comparison between ductile and shear energy absorption mechanisms, the utilization of specific energy absorption per unit mass proves beneficial. Figure 3.17 visually demonstrates the superior energy absorption capability of the ductile mechanism. This is evident from Figure 3.16, as a larger surface area is involved in absorbing the impact energy, leading to enhanced absorption capacity. All the impacted aluminum specimens are reported in Appendix C.

3.7. Carbon High-Velocity Response

Following the fabrication method for vacuum bags, it was observed that the desired thicknesses of the carbon material were mostly not achieved, primarily attributed to uncertainties encountered during the curing cycle in the autoclave. The actual thicknesses and masses obtained from this process are documented in Table 3.14.

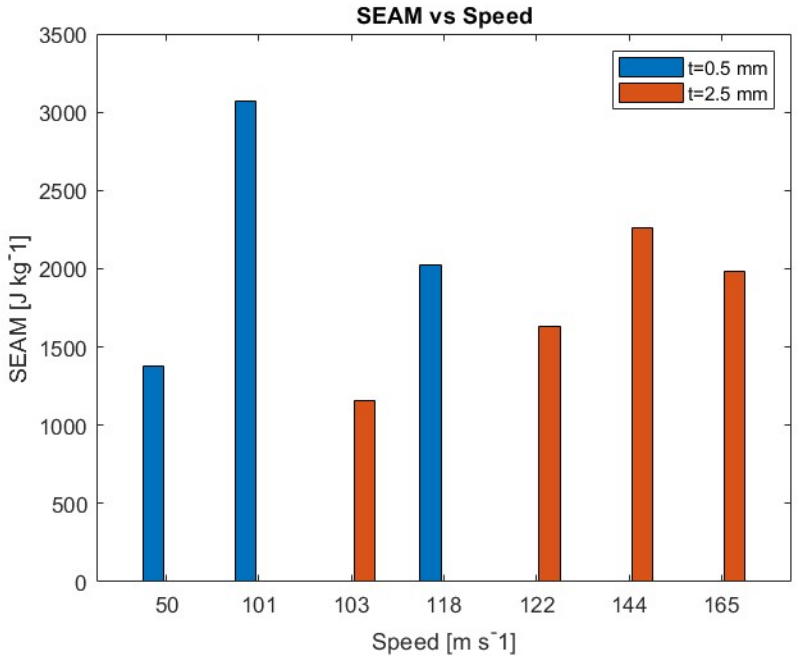

Figure 3.17: Specific energy absorption per mass versus speed for thin and thick aluminum

Test ID	Thick $[mm]$	Mass $[gr]$
1IC	2.59	55
2IC	4.7	100
3IC	5.25	110
4IC	6.8	150
5IC	8.8	195
6IC	9.61	200

Table 3.14: Physical Characteristics of Carbon Laminates

The impacts were conducted in a progressive manner, starting with the thinnest specimens and progressing to the thickest. The energy absorption values for each specimen are provided in Table 3.15. Throughout all impacts, the objective remained consistent, aiming to identify the specimen capable of absorbing a projectile at the threshold speed of 120 m/s. To facilitate the search for this specific speed range, air pressure of 2 bars was uniformly applied in all shots, although it will not be documented in the table.

During the initial testing, the first set of specimens exhibited energy absorption below the desired threshold velocity. This was primarily attributed to brittle failure mechanisms observed in the composite materials. However, following the completion of the testing campaign, it was determined that a threshold thickness of approximately 6.8 mm was necessary to achieve the targeted energy absorption at the threshold velocity.

Test ID	Thick $[mm]$	In V $[ms^{-1}]$	Out V $[ms^{-1}]$	Abs E $[J]$	Res E $[J]$
1IC	2.59	118	89	66	87
2IC	4.7	125	86	90.5	81.35
3IC	5.25	110	58	96	37
4IC	6.8	130	37	170.8	15
5IC	8.8	145	0	231.27	Rebound
6IC	9.61	114	0	142.95	Rebound

Table 3.15: Results from Impact Tests on Carbon Laminates

Figure 3.18 visually depicts the main failure modes, which include local delamination, fiber breakage, and matrix cracking. These failure mechanisms are significant contributors to energy absorption, as they occur only in a small fraction of the surface area. In the 9.6 mm thick laminate without penetration, the main failure modes observed are delamination and matrix cracking. This particular specimen is of significant interest because delamination is observed on both the top and bottom surfaces, while there is no failure detected across the thickness. However, in the penetrated sections, fiber breakage occurs throughout the entire thickness, accompanied by delamination across the laminate and some matrix cracking in the vicinity of the impact. Based on these findings, we can conclude that the initial failure mechanisms in the composite material are matrix cracking and delamination, whereas the final failure mode is fiber breakage.

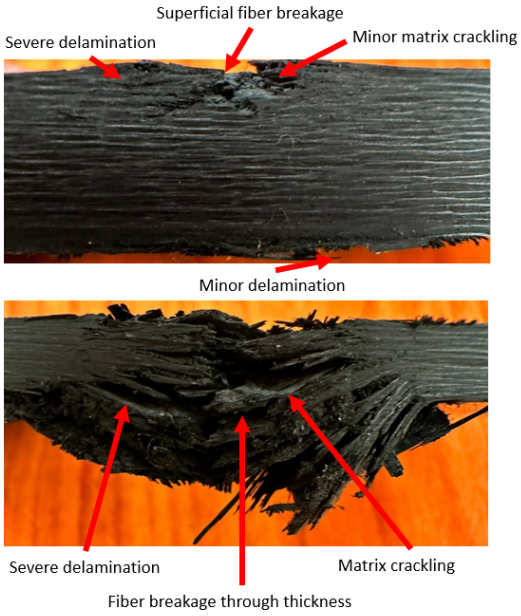

Figure 3.18: Failure modes of carbon specimens. Top: 5.5 mm thickness. Bottom: 9.6 mm thickness.

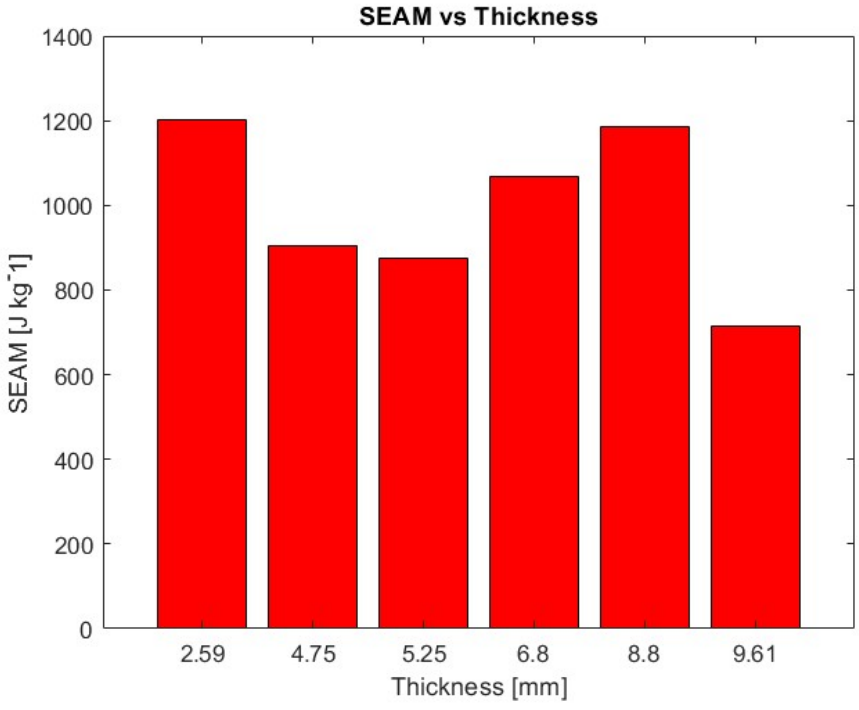

Figure 3.19: Specific energy absorption per mass versus thickness of carbon specimens

The relationship between thickness and specific energy absorption is depicted in Figure 3.19. It demonstrates a decreasing trend, indicating that thicker specimens have lower efficiency in absorbing energy compared to thinner ones. While the increase in stiffness is evident and contributes to reducing the projectile's speed, the failure mechanisms in thicker carbon specimens are less effective. Detailed information on all the carbon specimens subjected to impact testing can be found in Appendix D.

3.8. FML High-Velocity Response

Table 3.16 provides the physical properties of the carbon-aluminum specimens after the manufacturing process.

Test ID	Thick [mm]	Mass [gr]
1IFML	3.15	80
2IFML	5.55	135
3IFML	6.44	160
4IFML	3.47	100
5IFML	5.68	140
6IFML	8	190

Table 3.16: Physical Characteristics of FML

The shooting process of the carbon-aluminum specimens was conducted in two separate campaigns. The first campaign involved the first configuration with 2 aluminum plates, while the second campaign aimed to determine the threshold thickness for a stiffer laminate consisting of 3 aluminum plates. In the first campaign, the threshold thickness for the first configuration was found to be approximately 6.47 millimeters. The result of the impact on specimen 3IFML can be seen in Figure 3.20, the residual energy is considered zero since the projectile got stuck while penetrating the last section of the laminate. For the three aluminum plate configurations, the threshold thickness considered was around 5.68 millimeters, as the residual energy was exceptionally low, indicating close to complete energy absorption with less than 2% remaining energy. A summary of the testing campaign results can be found in Table 3.17.

Test ID	Configuration	T [mm]	In V [ms^{-1}]	Out V [ms^{-1}]	Abs E [J]	Res E [J]
1IFML	AL-C-AL	3.15	118	82	79.2	73.9
2IFML	AL-C-AL	5.55	117	40	135	17.6
3IFML	AL-C-AL	6.44	127	0	177.4	Stuck
4IFML	AL-C-AL-C-AL	3.47	111	68	84.7	50.9
5IFML	AL-C-AL-C-AL	5.68	123	22	161.4	5.32
6IFML	AL-C-AL-C-AL	8	115	0	1477	Rebound

Table 3.17: Results from Impact Tests on FML

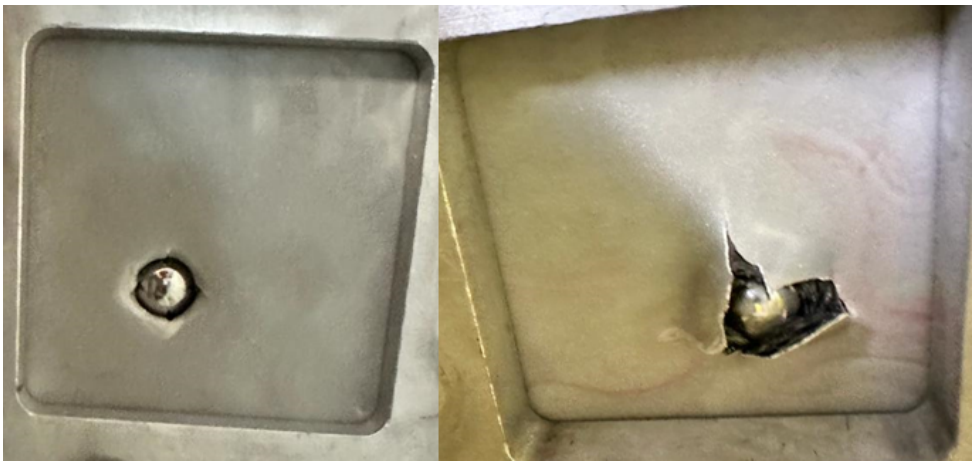

Figure 3.20: Imapct test on specimen 3IFML

The material constituents exhibit a combination of ductile and brittle behavior, resulting in a mixed failure mode. The ductility of aluminum plays a significant role, leading to a larger failure surface by integrating the observed failure modes in the composites. As shown in Figure 3.21, the failure occurs over a broader area, indicating the interaction of various failure mechanisms.

The carbon-aluminum specimens exhibit identifiable failure modes, including ductile dents, crack propagation, shear failure of aluminum, detachment at the carbon-aluminum interface, delamination, matrix cracking, and fiber breakage from the carbon constituent. Figure 3.21 also reveals that the failure modes in both configurations are similar, but the 2 aluminum configurations show more severe delamination and debonding between the constituents.

Interestingly, the three aluminum configurations demonstrate the ability to absorb more energy and distribute it effectively across the contact area. This enhanced energy absorption can be attributed to the higher ductility provided by the additional aluminum foil in these configurations.

Figure 3.22 presents the relationship between specific energy absorption and thickness for FML components. It is evident that, unlike carbon and aluminum, the amount of energy per mass remains quite consistent across different thicknesses and configurations. However, when comparing the 5.5 mm and 5.68 mm specimens, it becomes apparent that the addition of an extra layer of aluminum did not yield the expected benefits. While it enhanced the panel's stiffness, it also increased the weight, resulting in comparable absorbed energy when compared to the two aluminum plate configurations. Detailed information on all the FML specimens subjected to impact testing can be found in Appendix E.

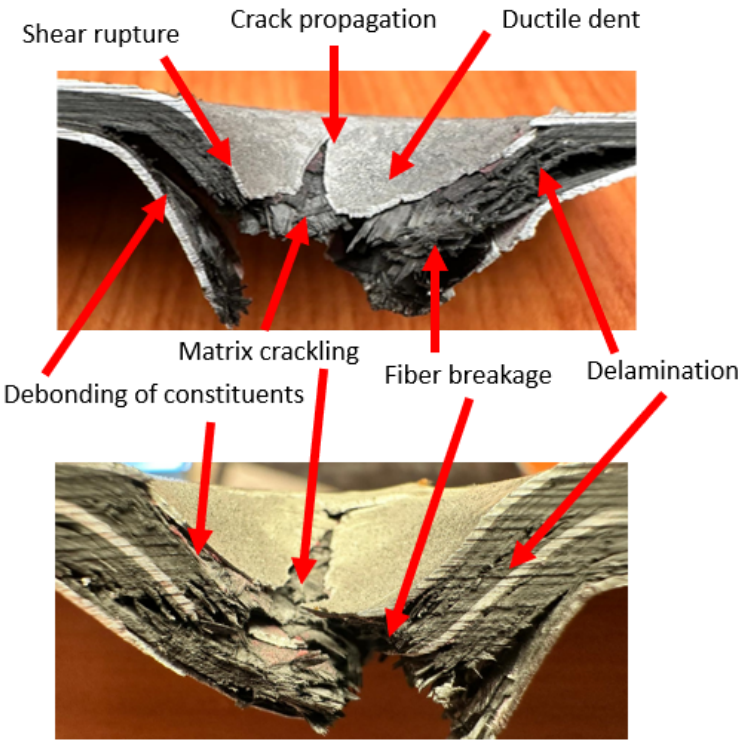

Figure 3.21: Failure modes FML specimens. Top: 5 mm thickness two aluminum configuration. Bottom: 5 mm thickness three aluminum configuration.

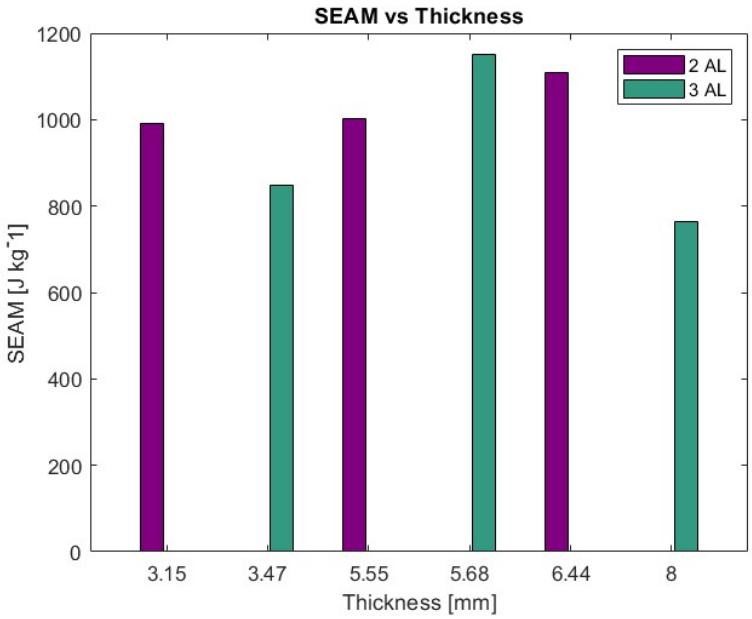

Figure 3.22: Specific energy absorption per mass versus thickness of FML specimens

4 | Numerical Analysis

This section provides a summary of numerical simulations conducted to analyze the impact. Finite element models are valuable, particularly when compared to experimental studies, as they are more cost-effective. Additionally, simulations allow for an understanding of failure mechanisms and progression that may not be observable in physical testing. However, the designer must ensure that the model accurately represents reality. One crucial aspect to consider is the selection of an appropriate material model, particularly when working with composite materials that do not exhibit straightforward behavior.

The first step to being done when approaching the numerical modeling of composites is the choice of the structural model. The plate theory was developed for this purpose, where the plane-stress condition is applied and the corresponding numerical equivalent is represented by the shell element. Layup sequence is implemented using Classical Lamination Theory (CLT), where each through-the-thickness integration point corresponds to a determined ply. Shell elements are very efficient but they lack precision with respect to solid elements. On the other hand, the use of solid elements will result in an exponential increase in computational time. Despite the missing capability of representing composite interlaminar behavior, the shell approach is the most preferred one thanks to its balance between accuracy and efficiency.

Initially, the bullet is represented as a solid sphere mesh with a diameter of 18 mm. The mesh has a density of 5, meaning there are 5 elements along the radius. Different material models are tested to examine significant plasticity effects in the steel projectiles. A plastic model is initially used, but it is determined that the plastic strain is negligible. As a result, an elastic material is chosen instead. Figure 4.1 shows that the elastic strain in the projectile is minimal after several simulations. Consequently, a decision is made to switch to a rigid body model for the projectile. This reduces the computational power required for the simulation and allows for a focus on the materials being impacted.

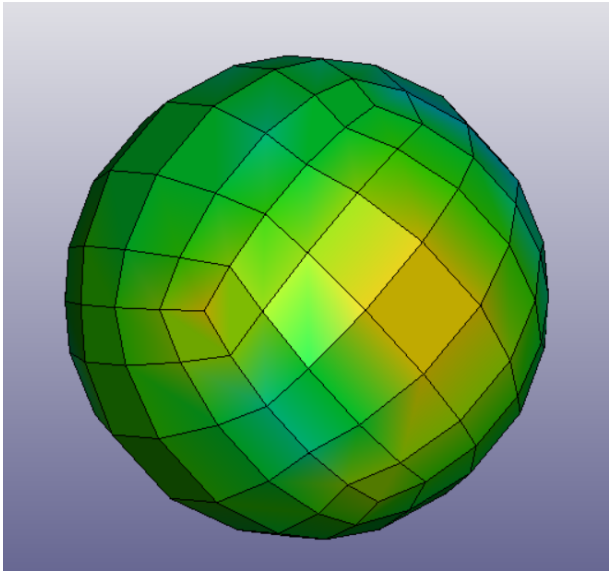

Figure 4.1: Elastic Strain used for the Projectile's Mesh

The plate used in the impact test is modeled with a 4-node mesh, selected to match dimensions of 120 x 120 mm. To ensure accuracy, the mesh comprised 240 x 240 nodes. Various material models are then applied to this base mesh. It's worth noting that a 20 x 20 mm section of the plate is fixed as a clamp using a set of nodes restricting the displacement and rotations in all directions to replicate the test conditions in the rig. Figure 4.2 illustrates the constrained nodes and mesh of the plate.

The bullet is positioned at 5 mm of distance from the plate, this is made in order to save computational time on the projectile's travel distance. The simulation time is fixed to 0.001 seconds and 2.5e-5 time intervals for the D3 plot to have a good understanding of the interaction between the late and the bullet. The speed of the projectile is initialized in velocity generation with a value of 100 m s^{-1}.

4.1. Aluminum Numerical Model

In order to account for the anticipated failure modes and energy absorption characteristics of aluminum, an elastoplastic constitutive law must be used to approximate its behavior. The LS-DYNA material type 24 (*MAT 024) is the prevailing material model for simulating impact events involving elastoplastic, isotropic materials. This model offers the flexibility to design arbitrary stress versus strain curves and strain rate dependencies. The behavior of *MAT 024 is described using Von Mises theory, which employs the Von Mises yield surface to establish the yield condition, as depicted in Figure 4.3.

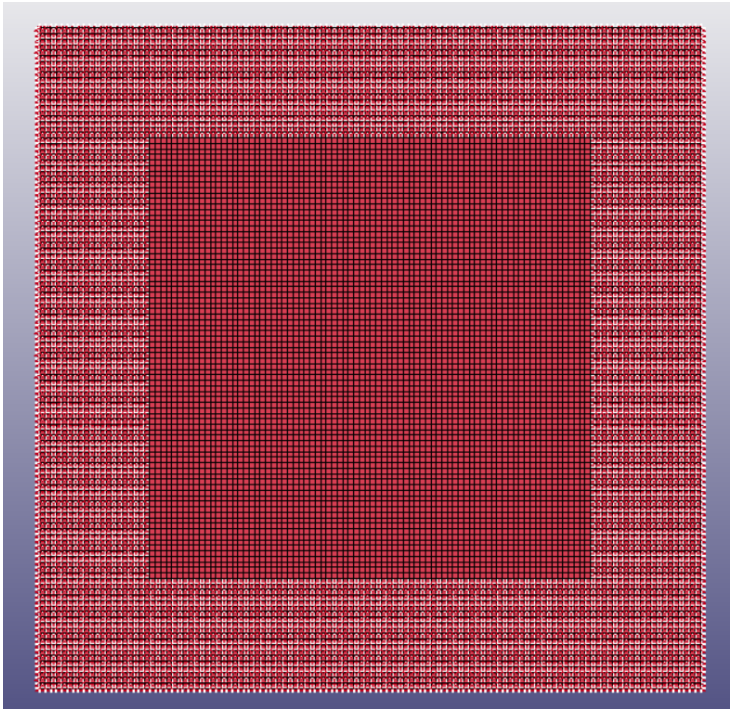

Figure 4.2: Plate's mesh and constrained nodes

The region of elasticity is assumed to be rate-independent until a yield point is determined, beyond which the stress-strain curve is divided into an elastic-plastic model for the lowest strain rate of interest. This model results in a plasticity curve, which is a stress function of plastic strain. However, when applied to plastics, the accuracy of this model depends on the linearity of the stress-strain relationship up to the selected yield point, which should not be rate-dependent, and the plasticity curve should have a uniform shape that is independent of strain rate. This assumption is only valid for ductile materials, not most plastics. As there is limited information on the rate dependency of the material, it is considered rate-independent in the plasticity region. The plastic behavior of the material is defined by a curve of points from the yield point to the failure limit.

The plastic curve can be directly measured by tensile test, but it can also be obtained via Ramberg–Osgood power law relation [17]:

$$\sigma_p = H\epsilon_p \tag{4.1}$$

$$H = \frac{\sigma_{yield}}{(\frac{\sigma_{yield}}{E})^n} \tag{4.2}$$

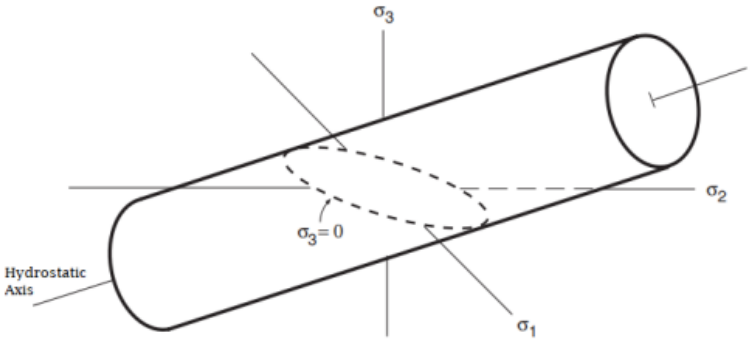

Figure 4.3: Von Mises yield surface

The stress and strain in the plastic region ($\sigma > \sigma_{yield}$) are denoted by σ_p and ϵ_p respectively, while the strain hardening exponent and the strain hardening coefficient are represented by H and n. The hardening parameters are determined by fitting test loading curves. In the case of Aluminum 2017, there was no explicit value available in the literature, so Aluminum 2024 was used as a reference due to its similar behavior and chemical constituents. The value of the exponential term is taken as n=0.23, according to a source cited as [36]. Table 4.1 reports the material card for MAT_024.

MID	RO	E	PR	SIGY	ETAN	FAIL	TDEL
C	P	LCSS	LCSR	VP			

Table 4.1: MAT_024 card overview

Apart from the commonly known elastic parameters, the variables that are relevant for the conducted simulation are:

- SIGY: yield stress value.
- LCSS: Load Curve of plasticity region, the first value in stress must be equal to SIGY.

Table 4.2 reports all the data to define the ductile material. Figure 4.6 reports the plastic stress-strain curve of ductile material employed in the experimental test, the data of the curve are directly associated with MAT_024 card via the LCSS card option.

The plasticity stress-strain curve was obtained directly from the experimental tensile tests. However, during the numerical analysis, the measured response oscillated, causing numerical problems. To resolve these issues, a smoothing operation was performed using Matlab. The yielding stress was set as the initial stress value, and the resulting curve is presented in Figure 4.4.

ρ	2.82 g/cm^3	Computed from known volume and mass
E	72.30 GPa	From tensile aluminum characterization tests
ν	0.33	Common value of aluminum materials
ϵ^{max}	0.18	Defined in order to replicate experimental results
σ_{yield}	334.2 MPa	From tensile aluminum characterization tests

Table 4.2: Data used for aluminum numerical model

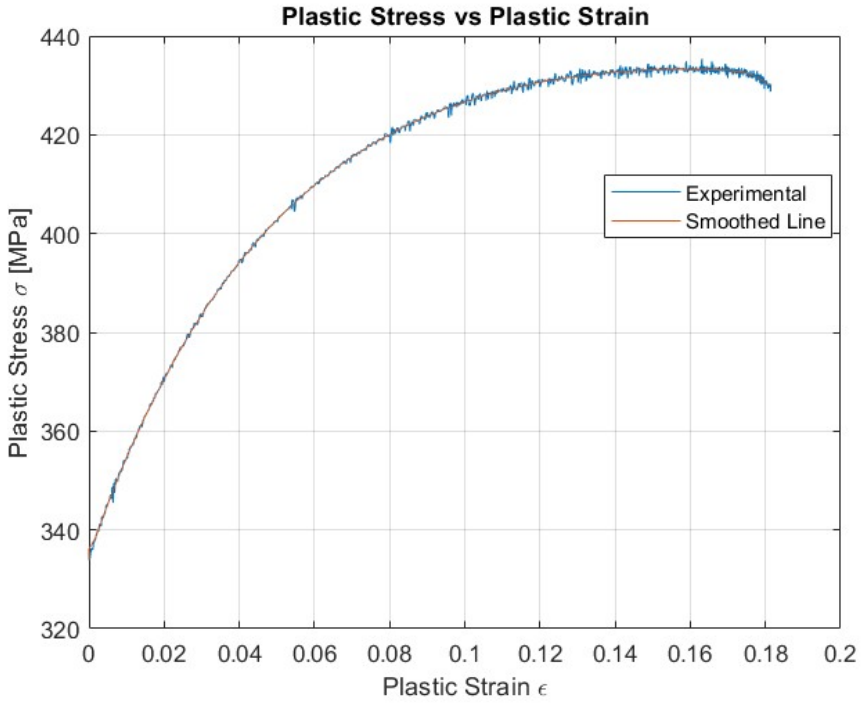

Figure 4.4: Plastic stress vs plastic strain diagram of the Aluminum

The numerical model needs refinement to match impact test results. The impact lacks repeatability, leading to varying absorbed energies due to uncertainties in factors like pressure distribution, projectile attitude, and impacted surface. The model refinement aims to maintain the original material model while allowing for some error, focusing on finding answers close to the observed absorbed energy.

Two main parameters can be adjusted to refine the model: the mesh and the strain to failure. Initial results indicated that a highly refined mesh resulted in a flexible and weak plate. To address this, a coarser mesh was employed for both aluminum thicknesses, making the plate stiffer. This modification enabled the plate to absorb more energy compared to the initial iteration, as shown in Figure 4.5. The new mesh consists of 40x40 elements, with each element measuring 3 mm in length.

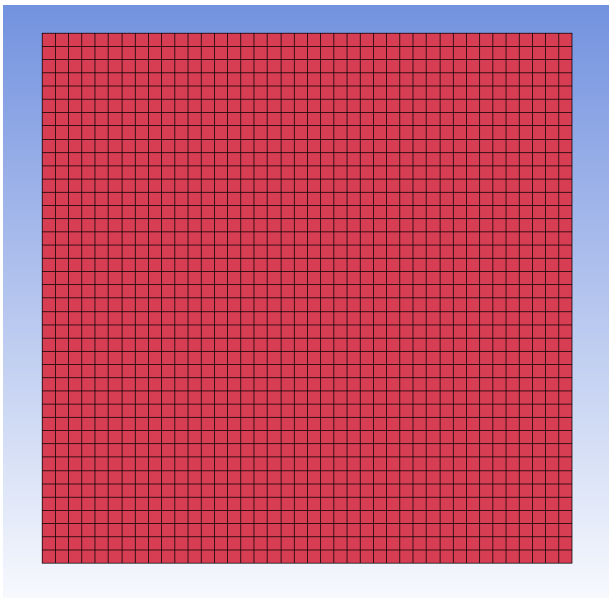

Figure 4.5: New mesh of aluminum plate

The second parameter to be modified is the strain to failure. By raising the plastic strain to failure to 0.19 compared to the original 0.18, a stronger plate was obtained, resulting in consistent outcomes and a more ductile failure in the perforated area. The simulations demonstrate that the thin, more ductile specimen exhibits a more evenly distributed plastic energy absorption, showcasing different failure mechanisms, in contrast to the thicker and less ductile specimen, as depicted in Figure 4.6.

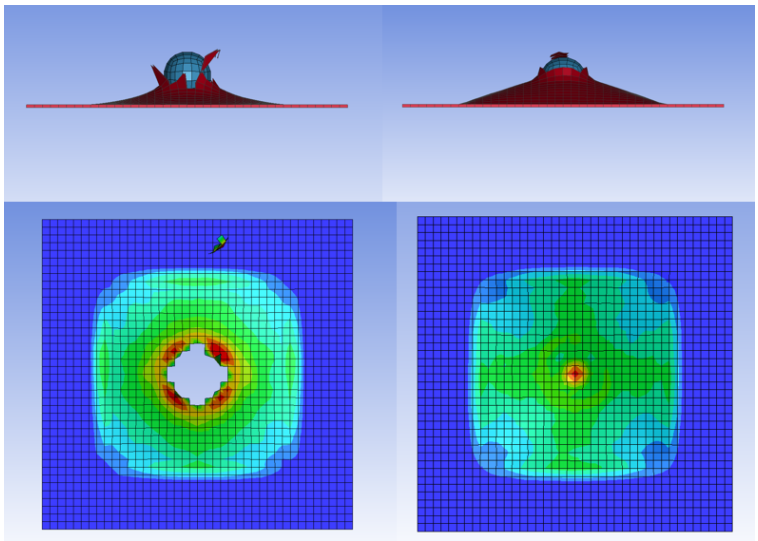

Figure 4.6: Top: Perforating frame between plate and bullet. Bottom: Effective plastic strain. Left: Thick specimen results. Right: Thin specimen results.

To evaluate the model's accuracy against experimental results, the total energy of each component is computed. The residual energy of the projectile is determined by analyzing the remaining energy after impact, while the absorbed energy by the plate indicates its ability to absorb energy. These quantities are graphically represented, focusing on the brief interaction between the plate and the bullet. The graphs reveal that threshold thicknesses have zero residual energy, and the absorbed energy matches the initial energy of the projectile. For the absorbed energy to exceed residual energy, the lines representing projectile and plate energies must intersect. Figure 4.7 illustrates energy absorption plots, with the top line representing the projectile energy decreasing s the energy is absorbed, and the bottom line representing plate energy increasing with the absorbing energy.

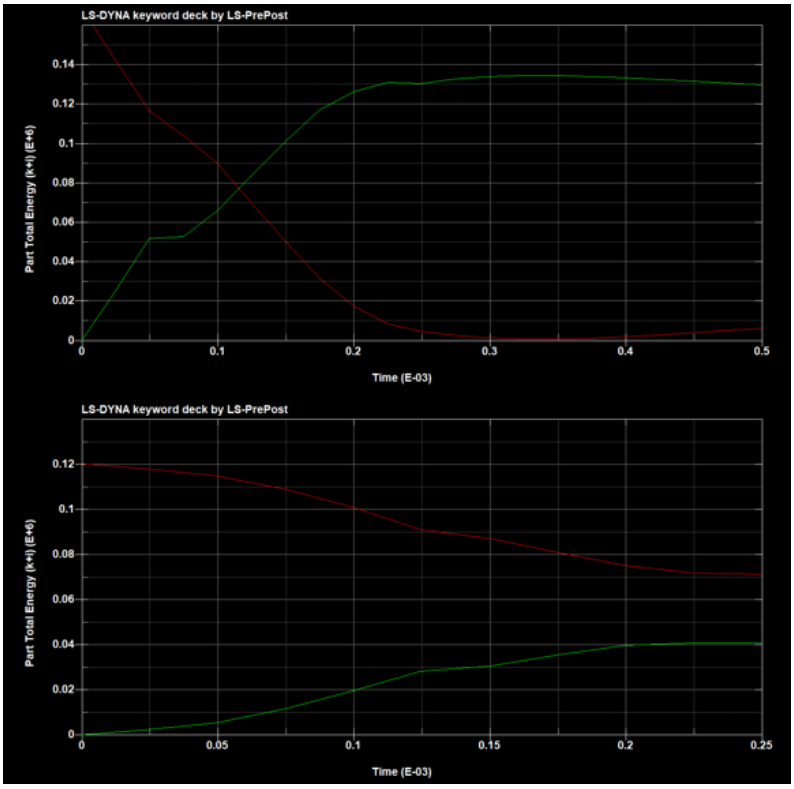

Figure 4.7: Upper: A robust specimen reaches the threshold speed of 122 m s^{-1}. Lower: A slender specimen experiences an impact at 100 m s^{-1}.

Table 4.3 presents the absorbed energy for each conducted simulation. It is worth noting that the model remains valid up to the threshold thickness, as indicated in Table 4.3. However, beyond this threshold, the model tends to exhibit increased unpredictability and inefficiency in energy absorption. Appendix F shows the energy absorption plots for all the aluminum specimens.

Test ID	Thick [mm]	In V [ms^{-1}]	Abs E [J]	Res E [J]
1SA	0.5	50	28.2	Rebound
2SA	0.5	101	51.2	64.8
3SA	0.5	118	21	134
4SA	2.5	103	120	Rebound
5SA	2.5	122	169	Rebound
6SA	2.5	144	188	46
7SA	2.5	165	113	200

Table 4.3: Results from energy absorption simulation of aluminum specimens

4.2. Carbon Numerical Model

LS-DYNA presents a vast choice in terms of orthotropic material models [34]. A brief overview of the composite material cards is reported in [38], the previously cited references in the second chapter suggest the use of material type 58 to model a composite plate.

LS-DYNA's material model relied on Hashin's damage mechanics model [4], which enables independent damage modeling in the principal directions of orthotropic materials. The model assumes that failure is a result of stresses acting on planes, and the failure criteria are classified into tensile and compressive modes. These criteria are combined into a quadratic polynomial format.

a) In tensile fiber mode, E_1, E_2, G_{12}, ν_{12}, $\nu_{21} = 0$ after lamina failure

$$\sigma_1 > 0 \text{ then } e_f^2 = (\tfrac{\sigma_1}{X_T})^2 - 1 \text{ if } \geq 0 \text{ failed \& if } < 0 \text{ elastic} \tag{4.3}$$

b) Compressive fiber mode causes fiber buckling. Hence, the parameters E_1, ν_{12}, ν_{21} $= 0$

$$\sigma_1 < 0 \text{ then } e_c^2 = (\tfrac{\sigma_1}{X_C})^2 - 1 \text{ if } \geq 0 \text{ failed \& if } < 0 \text{ elastic} \tag{4.4}$$

c) When the matrix begins to crack, the enters the tensile matrix mode, causing the values of E_1, ν_{12}, $G_{12} = 0$

$$\sigma_2 > 0 \text{ then } e_m^2 = (\tfrac{\sigma_2}{Y_T})^2 + (\tfrac{\tau_{12}}{S_C})^2 - 1 \text{ if } \geq 0 \text{ failed \& if } < 0 \text{ elastic} \tag{4.5}$$

d) When the lamina fails, the material constants E_1, ν_{12}, ν_{21}, $G_{12} = 0$. Accordingly, the failure mode is called the compressive matrix mode.

$$\sigma_2 < 0 \text{ then } e_d^2 = (\tfrac{\sigma_2}{2S_C})^2 + (\tfrac{\tau_{12}}{S_C})^2 - 1 \text{ if } \geq 0 \text{ failed \& if } < 0 \text{ elastic} \tag{4.6}$$

σ_1 is the stress in the fiber direction, σ_2 is the stress perpendicular to the fiber direction, τ_{12} is the shear stress in the lamina plane, ν_{12} and ν_{21} are the major and minor Poisson's ratio, respectively. The parameters X_T, X_C, Y_T, Y_C, and S_C are the limit strengths in tension and compression respectively for the parallel, perpendicular, and shear directions of the material.

The failure surfaces that h bound the elastic region can be extrapolated starting from the failure criteria by introducing a damage function $w_i(i = 1, 2, s)$, defined for $w_i < 0$ and a damage threshold r that defines the size of the elastic region.

$$f_{\parallel} = \frac{\sigma_1^2}{(1 - w_{1c,t})^2 X_{c,t}^2} - r_{\parallel c,t} \tag{4.7}$$

$$f_{\perp} = \frac{\sigma_2^2}{(1 - w_{2c,t})^2 Y_{c,t}^2} - r_{\perp c,t} \tag{4.8}$$

$$f_s = \frac{\tau_{12}^2}{(1 - w_s)^2 S_c^2} - r_s \tag{4.9}$$

The parameters $\epsilon_i(1T, 1C, 2T, 2C, S)$ and $SLIM_i(1T, 1C, 2T, 2C, S)$ are introduced, where ϵ_i is defined as the strain at the maximum stress response and $SLIM_i$ is the ratio of the limiting stress to the peak stress, $SLIM_i$=1 corresponds to no strain softening. A parameter study indicated that varying ϵ_i changed the slope of the pre-and post-peak response, a greater ϵ_i value results in a smaller slope of the stress-strain response while $SLIM_i$ sets a predefined limiting stress. At the limiting stress, the damage law is described by Formula 4.8. Figure 4.3 show parameter $SLIM_i$ defines the minimum stress limit of damaged material.

$$w = 1 - \frac{SLIM_i X_i}{E\epsilon_i} \tag{4.10}$$

An overview of the material model implementation is now given by highlighting the most relevant parameters. Table 4.1 shows the parameters that make up the MAT_058 card.

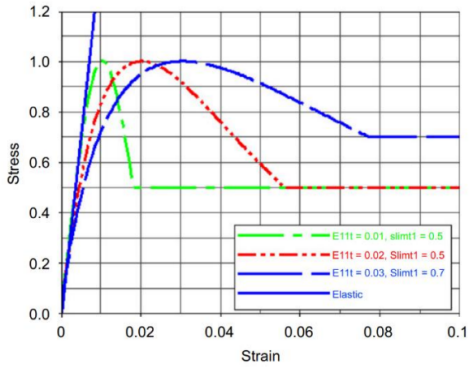

Figure 4.8: Examples of stress-strain responses for various ϵ_i and $SLIM_i$ values

MID	RO	EA	EB	EC	PRBA	TAU1	GAMMA1
GAB	GBC	GCA	SLIMT1	SLIMC1	SLIMT2	SLIMC2	SLIMS
AOPT	TSIZE	ERODS	SOFT	FS	EPFS	EPSR	TSMD
XP	YP	ZP	A1	A2	A3	PRCA	PRCB
V1	V2	V3	D1	D2	D3	BETA	LCDFAIL
E11C	E11T	E22C	E22T	GMS			
XC	XT	YC	YT	SC			

Table 4.4: MAT_058 card overview

Apart from the elastic constants and strength-related parameters, the material behavior in *MAT_058 can be significantly affected by important non-physical variables.

- ERODS: This is the maximum effective strain that determines the element deletion (complete failure). If lower than zero, the element fails when the effective strain calculated from the full strain tensor exceeds ERODS.
- FS: Failure Surface type, which defines the use of equations (4.5),(4.6), or (4.7). If failure criteria are taken as independent, non-linear shear behavior can be obtained through parameters GAMMA1, TAU1, GMS, SC. Figure 4.4 represents the method.

- TAU1, GAMMA1: Are the stress and strain limits of the first slightly nonlinear part of the shear stress versus shear strain curve. Values are used to define the curve of shear only for FS=-1.
- SOFT: This is a parameter related to the crash-front algorithm. In order to obtain a realistic crack propagation, once an element is deleted, all adjacent to it are subject to a stress reduction during the softening part.
- TSIZE: Element is deleted when the time step is smaller than the given value.

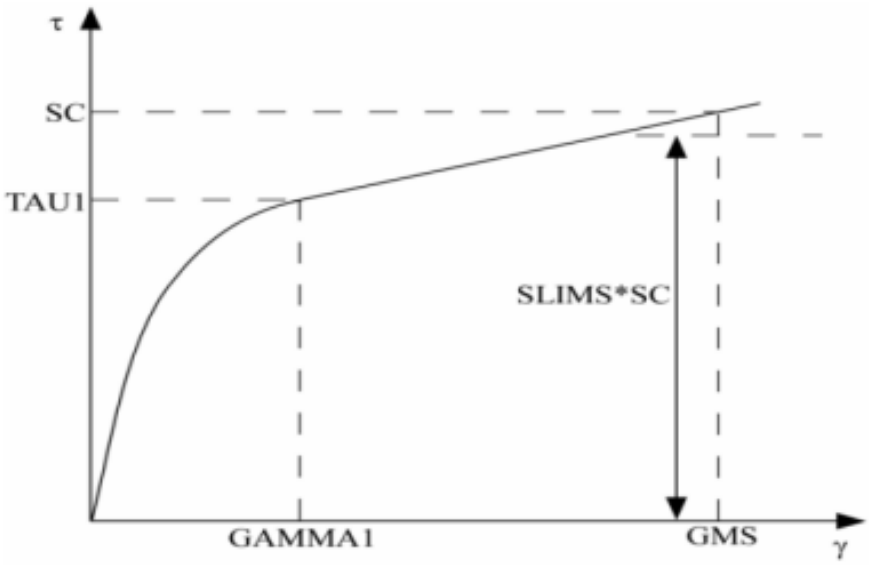

Figure 4.9: Stress-strain diagram of shear

Table 4.2 reports the data used to define the fabric material in LS Dyna.

ρ	1.41 g/mm^3	Computed from known volume and mass
E	62.154 GPa	$EA = EB$, from the carbon characterization tests
ν	0.0496	From tensile carbon characterization tests
ϵ_T^{max}	0.01319	$E11T = E22T$, from tensile carbon characterization tests
ϵ_C^{max}	0.024	$E11C = E22C$, from compressive carbon characterization tests
X^C	489.92 MPa	XC=YC, from compressive carbon characterization tests
X^T	739.02 MPa	XT=YT, from tensile carbon characterization tests
G	3679.3 MPa	From shear carbon characterization tests
γ^{max}	0.05	From shear carbon characterization tests
τ^{max}	66.28 MPa	From shear carbon characterization tests
$\gamma 1$	0.02	Extrapolated from figure 3.10
$\tau 1$	46.6 MPa	Extrapolated from figure 3.10
ERODS	0.35	Defined with trials and errors
SOFT	0.55	Suggested in [40]
SLIMT2	0.01	Small but not zero residual strength is assumed after tensile failure to avoid numerical instabilities [40]
SLIMT1	0.1	Recommended in [34]
SLIMC	0.8	SLIMC1=SLIMC2=SLIMS, suggested value in [34] is 1, reduced after trials and errors
FS	-1	Faceted failure surface. When the strength values are reached then damage evolves in tension and compression for both the fiber and transverse direction. Shear behavior is also considered.[34].

Table 4.5: Data used for carbon numerical model

Similar to aluminum, the experimental plates surpass the numerical model in terms of strength when it comes to carbon. To address this issue, the solution involves adjusting the mesh density and manipulating the strain-to-failure values. Unlike the single strain-to-failure used in aluminum, there are now five different strains considered: tensile longitudinal, compressive longitudinal, tensile transversal, compressive transversal, and shear strain. To enhance the plate's strength, the mesh from the aluminum case was reused, while the strains were scaled to minimize the material's alteration. A scaling factor of 1.5 was chosen as a compromise between thin and thick specimens. Figure 4.10 illustrates the failure behavior of the composite numerical model.

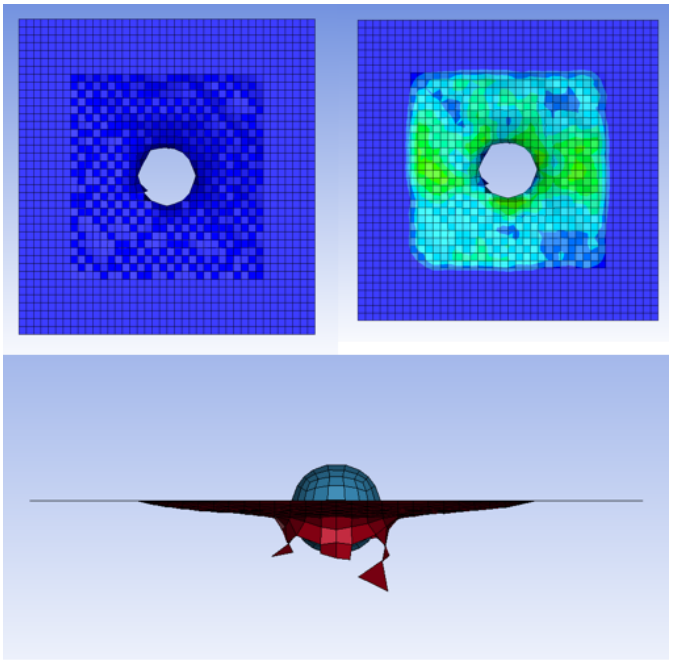

Figure 4.10: Top left: Effective plastic strain on carbon laminate. Top right: Von misses stress on carbon. Bottom: Penetrating interaction between projectile and laminate.

In Figure 4.10, the carbon laminate's effective plastic strain is displayed, confirming the expected behavior of the plate. Due to the brittle nature of the material and its lack of ductility, the plate exhibits no plastic deformation. Consequently, the failure is sudden and localized primarily in the center of the plate, which differs from the behavior observed in the aluminum case. Despite the elastic strain being zero, other areas of the surface exhibit limited contribution to the impact resistance, as indicated by the Von Mises stress. However, this contribution is minimal compared to the significant amount of energy absorbed locally through the fracture of the surface in contact with the bullet. The simulation results are summarized in Table 4.6. The energy absorption plots are included in Appendix G.

Test ID	Thick [mm]	In V [ms^{-1}]	Abs E [J]	Res E [J]
1SC	2.5	118	51	107
2SC	4	125	90.8	86.2
3SC	5.3	110	103.8	33.2
4SC	7.2	130	142	41
5SC	8.8	145	190.8	48.2
6SC	10.5	114	129.9	Rebound

Table 4.6: Results from energy absorption simulation of carbon specimens

4.3. FML Numerical Model

The interaction between composite laminate and the metal plates is modeled as an adhesive interface that is mainly dominated by the delamination phenomena. This adhesion interface modeling has several approaches in LS-DYNA, the two main approaches used in FML are tiebreak contacts and adhesive elements ad mentioned in Chapter Two.

Cohesive elements model the interface between two materials as a thin layer of cohesive material with its own material properties, such as stiffness, strength, and fracture energy. When the interface experiences a certain level of stress, the cohesive layer can begin to deform and eventually fail, simulating the delamination or fracture of the FML. While tiebreak contact models the interface between the layers of fiber and metal as an interface that is connected by a set of springs or penalty constraints. When the interface experiences a certain level of stress, the springs break, simulating the separation of the layers in the FML.

Modelling adhesive elements is challenging and often requires significant computational resources, making tiebreak contacts a more preferable option. Tiebreak contacts are widely used and considered a reliable and relatively simple contact algorithm. To simulate the adhesive interface of a CFRP-AL laminate and model the delamination behavior between its constituents, the CONTACT_AUTOMATIC_ONE_WAY_SURFACE_TO_SURFACE _TIEBREAK contact card is employed. One-way contact types allow for compression loads to be transferred between the slave nodes and the master segments.

The algorithm ties nodes that are initially in contact by creating a linear spring, and the debonding of the surface initiates when the maximum stress criterion is met, which leads to scaling down of the stress by a linear damage curve until the critical separation is reached and the spring is removed [28]. The failure stress tiebreak criterion is defined in formula 4.11.

$$(\frac{|\sigma_n|}{NFLS})^2 + (\frac{|\sigma_s|}{SFLS})^2 \geq 1 \tag{4.11}$$

In which σ_n and σ_s are the normal and shear stresses acting at the interface, while NFLS and SFLS are the normal and shear strength of the tie, respectively. Table 4.5 reports the material card for tiebreak contact. The parameters that define the card are listed in

SSID	MSID	SSSTYP	MSTYP	SBOXID	MBOXID	SPR	MPR
FS	FD	DC	VC	VDC	PENCGIK	BT	DT
SFS	SFM	SST	MST	SFST	SFMT	FSF	VSF
OPTION	NFLS	SFLS	PARAM	ETAEN	ERATES		

Table 4.7: AUTOMATIC_ONE_WAY_SURFACE_TO_SURFACE_TIEBREAK card overview

Table 4.6. The variables used for this card are listed below.

- FS, FD: Static and dynamic friction coefficient respectively.
- SST, MST: Optional thickness for slave and master surface (overrides true thickness). This option applies only to contact with shell elements. These parameters have no bearing on the actual thickness of the elements, it only affects the location of the contact surface.
- $NFLS, SFLS$: the same as equation (4.11).
- PARAM is the critical distance at which the failure occurs (i.e., deletion of the tiebreak and advancing of delamination).
- OPTION: Type of response of the contact. OPTION=8 is the most common option for the use of tiebreak contacts for delamination analysis. Tiebreak is active for nodes that are initially in contact. Failure stress must be defined for a tiebreak to occur. After the failure stress tiebreak criterion is met, the damage is a linear function of the distance between points initially in contact. When the distance is equal to PARAM damage is fully developed and interface failure occurs

FS	0.15	Taken from reference [22]
FD	0.14	Taken from reference [22]
$NFLS$	12 MPa	Taken from reference [59]
$SFLS$	36 MPa	Taken from reference [59]
$PARAM$	0.025	Taken from reference [59]

Table 4.8: Data used for tiebreak contact card

4.3.1. 2 Aluminum Plates Configuration

In order to evaluate and develop numerical models for FML laminates, a differentiation was made between the two tested configurations. Firstly, the weaker configuration consisting of two aluminum plates is discussed. The model is constructed based on existing models of aluminum and carbon that have already undergone refinement through adjustments in mesh and strain to failure. For the FML model, only the PARAM parameter governing the distance at which the bonding between aluminum and carbon is disrupted is manipulated. The layout of the 2 aluminum plate configurations is depicted in Figure 5.4.

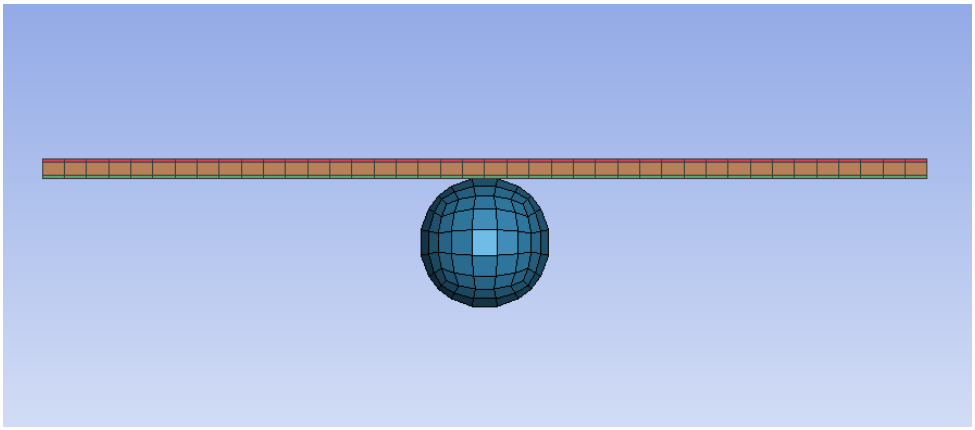

Figure 4.11: Top view with a unitary thickness of FML

The numerical model of the FML exhibited significantly lower strength compared to the experimental counterpart. To enhance the strength of the laminate, the PARAM parameter was increased to 0.85. The impact simulations were conducted, and the results are presented in Table 4.9. In contrast to the previous materials, the impact absorption in this FML laminate occurs in distinct stages. This is due to the composition of two aluminum layers and a carbon layer. As depicted in Figure 4.12, each stage of the laminate absorbs a varying amount of energy.

Test ID	Thick $[mm]$	In V $[ms^{-1}]$	Abs E $[J]$	Res E $[J]$
1FML	2.7	118	67.3	90.7
2FML	5	117	100.9	54.1
3FML	6.5	127	183	Rebound

Table 4.9: Results from energy absorption simulation of FML specimens

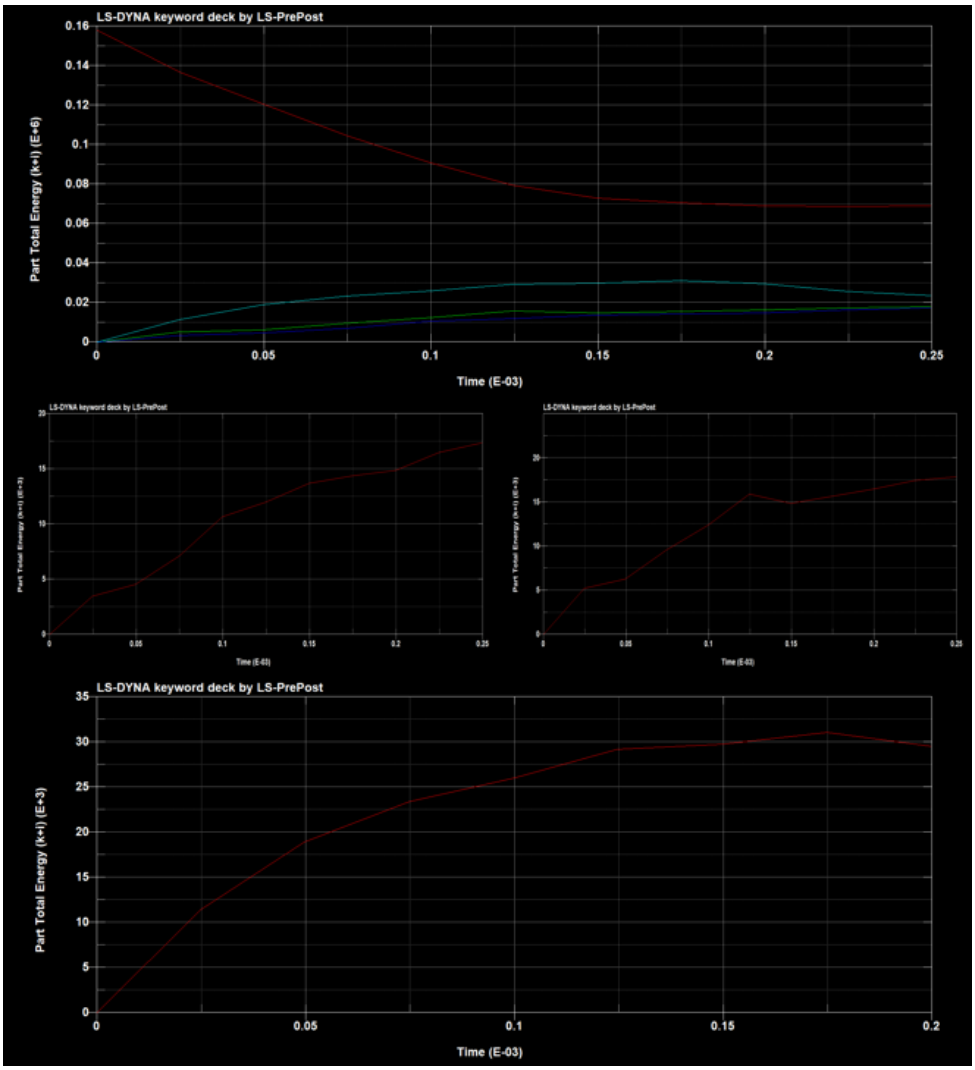

Figure 4.12: Top: Energy absorption of all parts. Left: Back aluminum face. Right: Front aluminum face. Bottom: Carbon energy absorption.

In Figure 4.12, the energy absorption of the different constituents in the 2.5 mm thick laminate is illustrated. In this simulation, the bullet was able to fully penetrate the laminate, exiting it. This is evident from the residual energy and the fact that the total absorbed energies do not match the initial energy of the projectile.

The aluminum constituents exhibit similar behavior, with each layer absorbing approximately 25 joules of energy. On the other hand, due to its greater thickness, the carbon component contributes a higher energy absorption of around 35 joules. Notably, the 1.5 mm thickness of the carbon significantly improves the overall energy absorption of the simulated 2.5 mm laminate.

This enhancement in energy absorption is primarily attributed to the ductility introduced by the aluminum plates. The increased ductility allows for a larger surface area of the carbon laminate to come into contact with the deformed initial aluminum, thus enabling greater energy absorption. This change in energy absorption can be observed through the alteration in the von Mises contour of the carbon, as depicted in Figure 4.13.

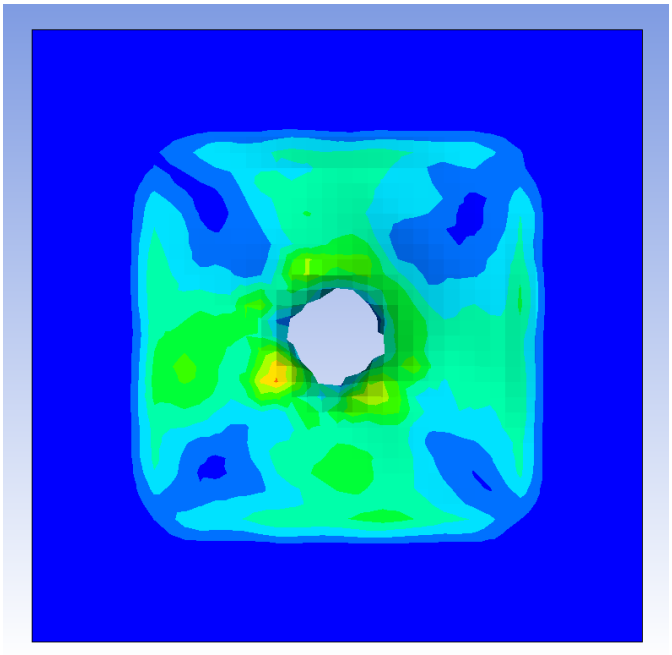

Figure 4.13: Von Misses contour of carbon constituent

4.3.2. 3 Aluminum Plates Configuration

Figure 4.14 displays the second FML configuration. In comparison to the two aluminum plates, the numerical model of the three aluminum plates appears excessively rigid. Despite utilizing the appropriate materials and PARAM parameter based on previous simulations, even the thinner components remain without being penetrated. Interestingly, the additional layer of aluminum located in the center of the laminate demonstrates a higher capacity for absorbing energy and resists penetration at a similar threshold as the top and bottom plies. The outcomes of the numerical analysis can be found in Table 4.10.

Test ID	Thick $[mm]$	In V $[ms^{-1}]$	Abs E $[J]$	Res E $[J]$
4FML	3.5	111	140	Rebound
5FML	5.68	123	172	Rebound
6FML	8	115	155	Rebound

Table 4.10: Results from energy absorption simulation of FML specimens

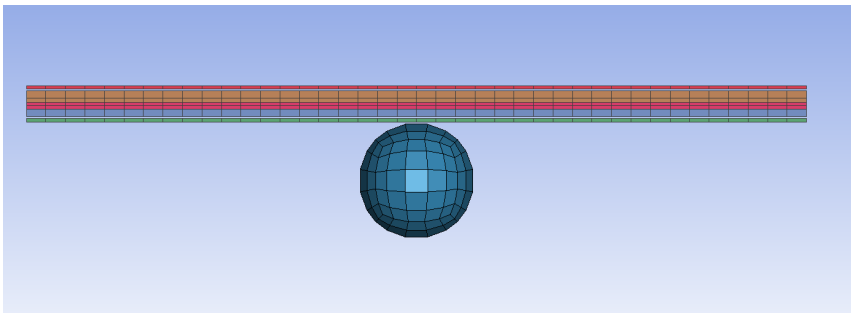

Figure 4.14: Top view of three aluminum configuration FML

In order to study the impact of an additional aluminum ply, the energy absorption plots are utilized. Figure 4.16 illustrates the energy absorption across the Fiber Metal Laminate (FML). The behavior of carbon is comparable to the configuration with two aluminum layers, exhibiting reduced absorption in the rear laminate primarily due to the energy absorbed by the preceding plies. However, the aluminum displays a distinct behavior in the middle layer. While the top and bottom aluminum plates absorb a similar amount of energy, the middle aluminum plate exhibits an unexpected behavior by absorbing a greater amount of energy compared to the other aluminum layers. This phenomenon can be better comprehended by examining the plastic strain in the middle aluminum, as depicted in Figure 4.15. The figure demonstrates a significant level of plastic deformation occurring on the surface, which could be attributed to the positioning between the composites, the presence of brittle and ductile interfaces, and the distribution of energy. All energy absorption plots are included in appendix H.

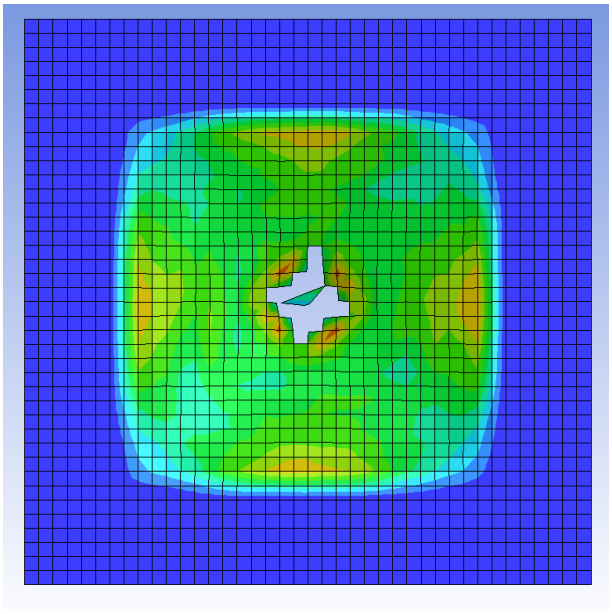

Figure 4.15: Plastic strain in the middle aluminum plate

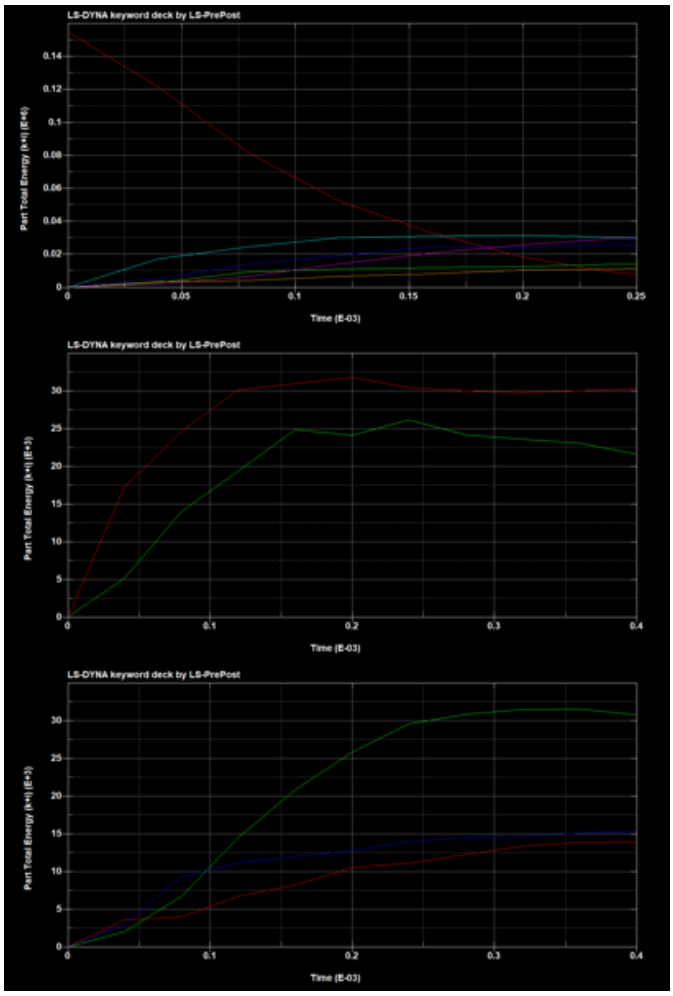

Figure 4.16: Top: Energy absorption of all parts. Middle: Carbon energy absorption red front and green back face. Bottom: Aluminum energy absorption red front, green middle, and blue back face.

5 | Results Comparison and Discussion

This chapter examines the disparities between experimental and numerical results for the different materials, particularly focusing on differences in energy absorption and the deformed shape of the specimen. Subsequently, a detailed comparison of the different materials is conducted to determine the optimal solution in terms of weight and required thickness for efficient energy absorption during impact. The comparison specifically considers the threshold thicknesses of each material. To ensure consistency when comparing different materials, specific energy absorption parameters are utilized. This approach allows for a meaningful comparison that is independent of exact velocities but rather focuses on a threshold value.

5.1. Aluminum Analysis

Comparing the experimental and simulated impacts on aluminum involves analyzing the deformed shape of the specimens, as plastic deformation is the primary absorption mechanism in aluminum. The effective plastic strain provides insight into the extent of plastic deformation along the specimen. Figure 5.1 illustrates the comparison between simulated and experimental results for aluminum specimens. It demonstrates a remarkable similarity between the thin, ductile behavior and the thick, shear behavior observed in both experimental and numerical data. This indicates the successful replication of experimental behavior through numerical simulations.

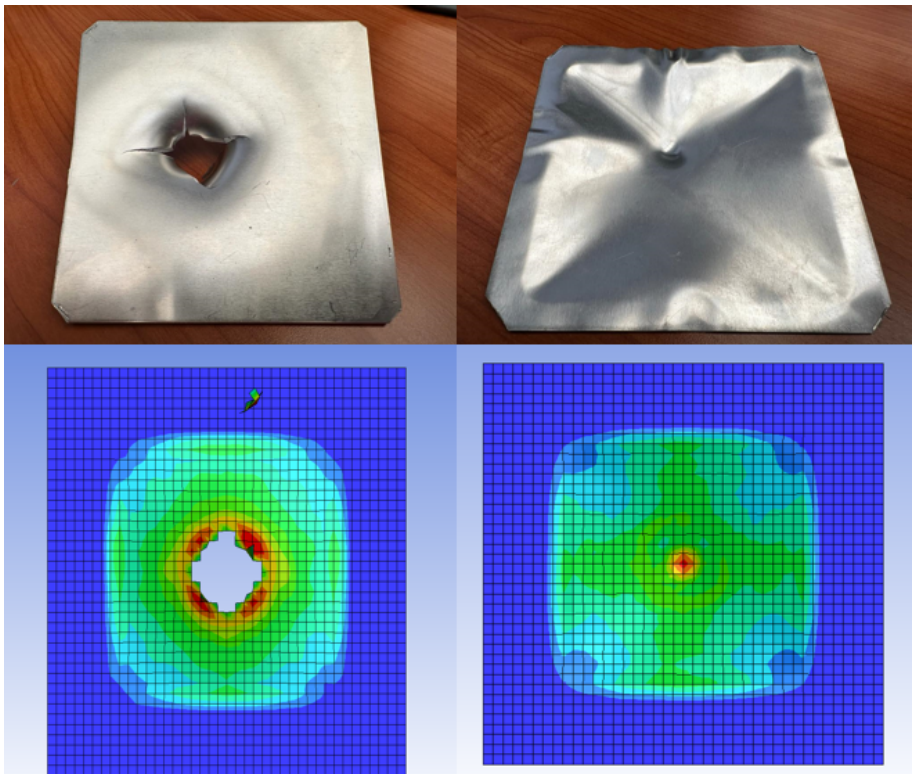

Figure 5.1: Left: Thick specimen. Right: Thin specimen.

The energy absorption capabilities of the two results can be compared by comparing the energy absorbed and the specific energy absorption of the plates. Table 5.1 shows the absorbed energy of each case and the error considered between both. Figure 5.2 shows the specific energy absorption of the simulated and experimental results. In both cases, we find the energy absorption is close but after the threshold velocities, the stiffness of the simulated plate is greatly reduced to the point where the absorbed energy at speed above the threshold the energy absorbed is far from the experimental one.

Test ID	Mass[gr]	In V [ms^{-1}]	Abs E [J]	Test ID	Abs E [J]	Error [%]
1SA	20	50	28.4	1IA	27.5	Rebound
2SA	20	101	51	2IA	61.3	16.5
3SA	20	118	21	3IA	40.5	48
4SA	100	116	120	4IA	116	Rebound
5SA	100	122	169	5IA	163	Rebound
6SA	100	144	144	6IA	226	36.39
7SA	100	165	113	7IA	198	43

Table 5.1: Comparison between experimental and numerical aluminum analysis

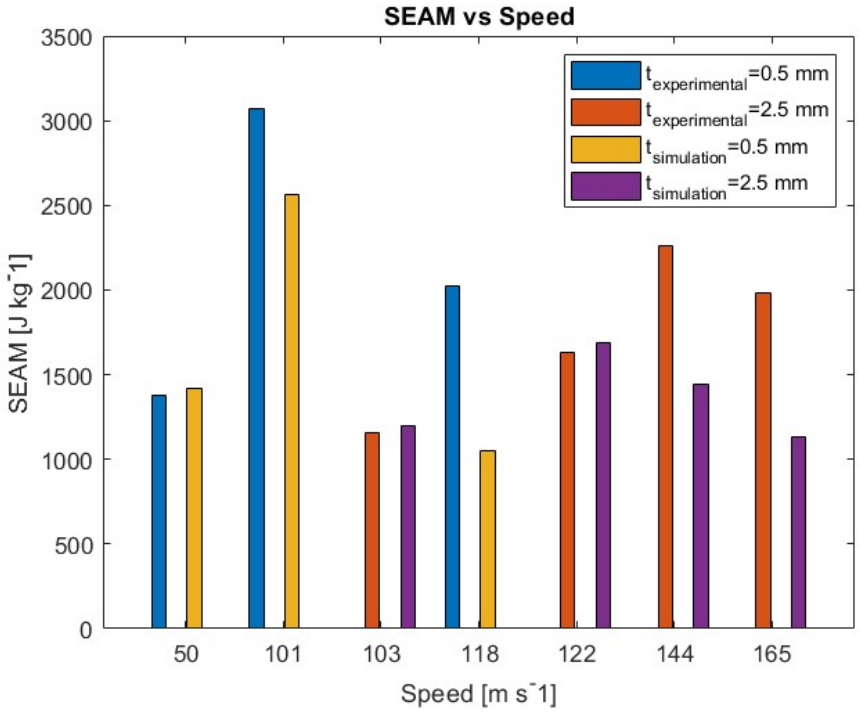

Figure 5.2: Specific energy absorption of experimental and numerical results.

5.2. Carbon Analysis

When comparing the numerical and experimental results for carbon, it becomes evident in Figure 5.3 that the deformed shapes are not directly comparable. The experimental results display a brittle failure, similar to the simulation, but the removal of failed elements in the simulation prevents the representation of failed material. In the experimental plates, the predominant failure modes are fiber breakage, matrix cracking, and delamination. However, the numerical response fails to capture the first two failure modes, and the third mode, which is dependent on out-of-plane properties, cannot be adequately accounted for. The energy absorption in the laminates primarily occurs through the stiffness of the plate and the failure of fibers and matrix. These aspects are incorporated in the Hashin model of the material in LS-Dyna.

In order to improve the accuracy of energy absorption in the experimental carbon laminates, it was necessary to adjust the failure scaling to account for less efficient energy absorption mechanisms in the numerical analysis. This adjustment was required due to the complexities involved in modeling the phenomenon and the limitations of shell elements in capturing out-of-plane reactions.

To assess and compare the energy absorbed by each approach, Table 5.2 presents the

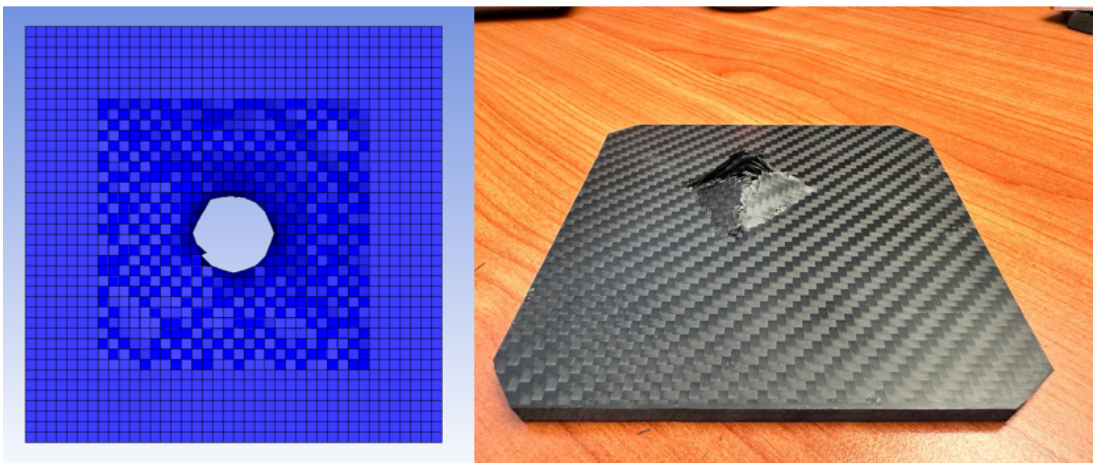

Figure 5.3: Left: Simulated carbon specimen. Right: Experimental carbon specimen.

energy absorbed by the numerical and experimental methods, along with the corresponding error between them. Additionally, Figure 5.4 compares the specific energy absorption between the numerical and experimental approaches. These results demonstrate a reasonable correlation between the experimental and numerical findings, highlighting the relatively poor efficiency of carbon laminates in high-velocity impacts.

Test ID	Mass[gr]	In V [ms^{-1}]	Abs E [J]	Test ID	Abs E [J]	Error [%]
1SC	55	118	51	1IC	66	22.7
2SC	100	125	90.8	2IC	90.5	0.3
3SC	110	110	103.8	3IC	96.1	8
4SC	150	130	142	4IC	170	16.8
5SC	195	145	190.8	5IC	231	Rebound
6SC	200	115	148	6IC	143	Rebound

Table 5.2: Comparison between experimental and numerical carbon analysis

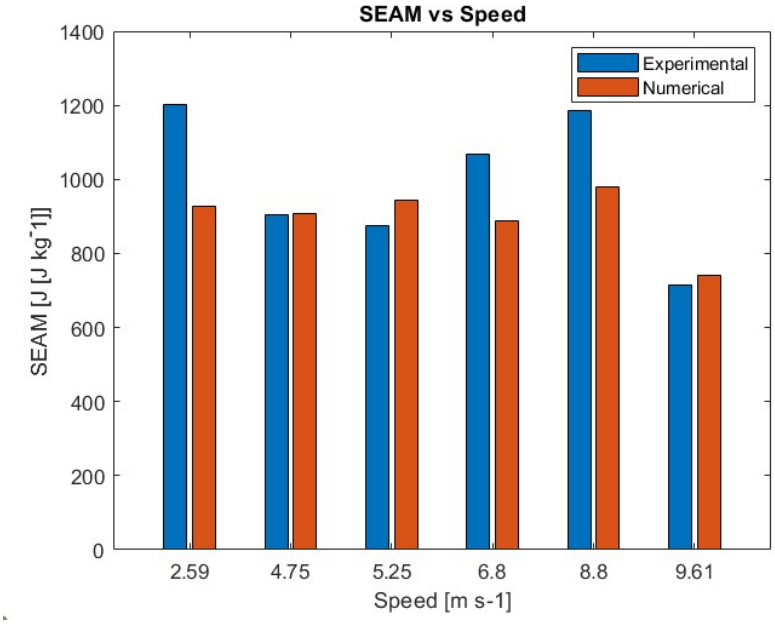

Figure 5.4: Specific energy absorption of carbon specimens comparing experimental and numerical results.

5.3. FML Analysis

Figure 5.5 presents a comparison of the deformed shapes between the experimental and numerical results. In the case of the two aluminum configurations, the numerical results exhibit a more ductile behavior for aluminum compared to the experimental results. The damaged area is larger in the numerical results, while the carbon area is reduced and localized. Additionally, the debonding between aluminum and carbon occurs over a broader area in the simulated results.

For the three aluminum configuration, the numerical aluminum layers behave similarly to the experimental ones. The middle and back aluminum layers deform as expected, following the trajectory of the projectile. However, the top aluminum layer behaves differently in the experimental results, as it does not produce a pronounced ductile dent but rather folds around the impact.

Similar to the two aluminum configuration, the carbon layers in the three aluminum configuration also exhibit limited deformation. Nonetheless, the overall deformed configuration of the FML in the numerical results resembles the experimental one, with debonding only occurring near the impact zone.

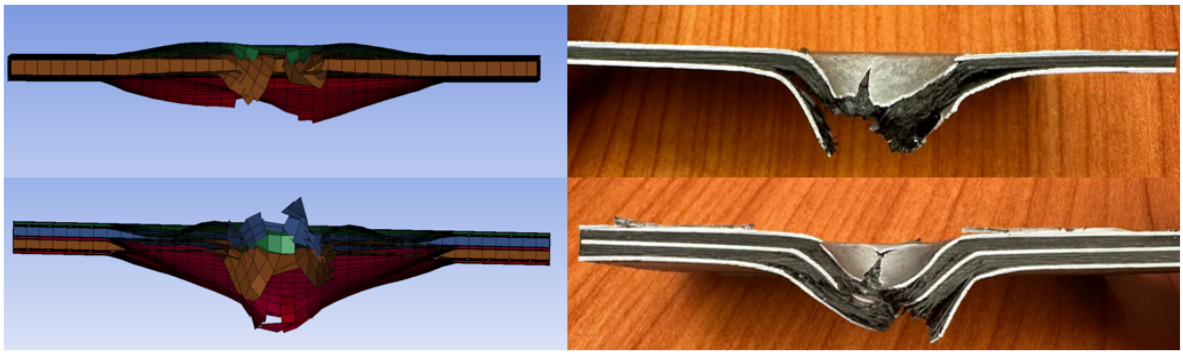

Figure 5.5: Top: Numerical and experimental comparison of impacted two aluminum configuration. Bottom: Numerical and experimental comparison of impacted three aluminum configuration.

In order to evaluate the energy absorption capabilities, it is crucial to compare the absorbed energy of each specimen. The energy absorption results are documented in Table 5.3. Furthermore, Figure 5.6 illustrates the specific energy absorption, highlighting the similarity between the numerical and experimental results. The minimal difference in specific energy absorption further supports the refinement of the model.

The findings indicate that the energy absorbed in the numerical tests is comparable to that in the experimental tests. It is worth noting that in the initial case, adjusting the PARAM parameter to increase the stiffness of the laminate proved beneficial. This adjustment helped compensate for unaccounted energy absorption mechanisms, such as the out-of-plane reactions leading to delamination in the composite and significant involvement in debonding between the constituents. However, it was discovered that this artificially increased stiffness was excessive for the thicker and stiffer three aluminum configurations. Consequently, modifications were made to the aluminum strain to align with the energy absorption observed in the experimental results.

Test ID	Mass[gr]	In V [ms^{-1}]	Abs E [J]	Test ID	Abs E [J]	Error [%]
1SFML	80	118	67.3	1IFML	79.2	15
2SFML	135	118	100.9	2IFML	135.5	25.5
3SFML	160	127	183	3IFML	177	Rebound
4SFML	100	111	140	4IFML	84.6	Rebound
5SFML	140	123	172	5IFML	161	Rebound
6SFML	190	115	155	6IFML	145	Rebound

Table 5.3: Comparison between experimental and numerical FML analysis

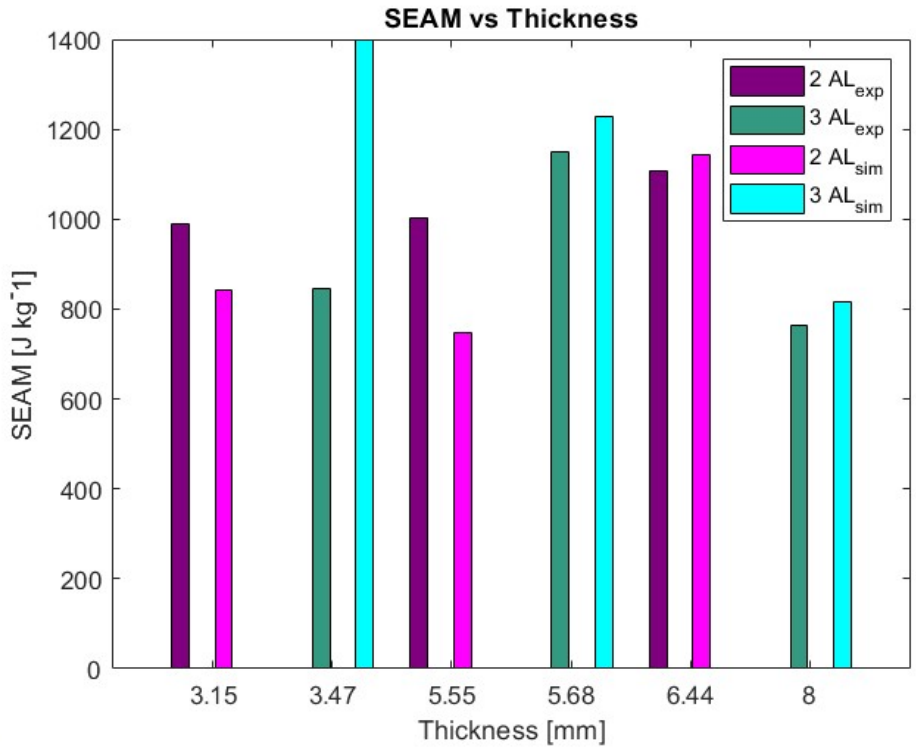

Figure 5.6: Specific energy absorption of experimental and numerical FML results.

5.4. Material Comparison

As mentioned previously only the threshold thicknesses for a set of speeds in the vicinity of 120 m. Since the amount of energy is similar for all the threshold thicknesses a more useful comparison can be made while comparing the absorbed energy capabilities normalized with respect to changing properties of the laminates. The comparison can be seen from two perspectives, the amount of energy absorbed per mass unit and a second approach considering the amount of energy per unit of thickness. Table 5.4 presents the results of the experimental campaign for the different laminates.

Test ID	In V $[ms^{-1}]$	T $[mm]$	Mass $[gr]$	Abs E $[J]$	Res E $[J]$	SEAM	SEAT
5IA	122	2.5	100	163.6	0.1	1636	65.44
4IC	130	6.8	150	170.8	15	1138.7	19.4
3FML	127	6.5	160	177.4	0	1108.8	27.3
5FML	123	5.48	140	161	5.3	1150	29.4

Table 5.4: Results from threshold thicknesses of the different materials

In Figure 5.7, the graph illustrates the specific energy absorption per unit mass for various materials. A clear observation from the graph is that aluminum is the most effective material for energy absorption in lightweight structures. It required nearly half the mass compared to the two-aluminum configuration FML to halt the bullet across different speeds. The other materials displayed similar behavior, as they required an equivalent mass to stop the bullet. This indicates that while the FML outperforms carbon in energy absorption, the additional weight contributed by aluminum makes the two solutions comparable in terms of overall weight.

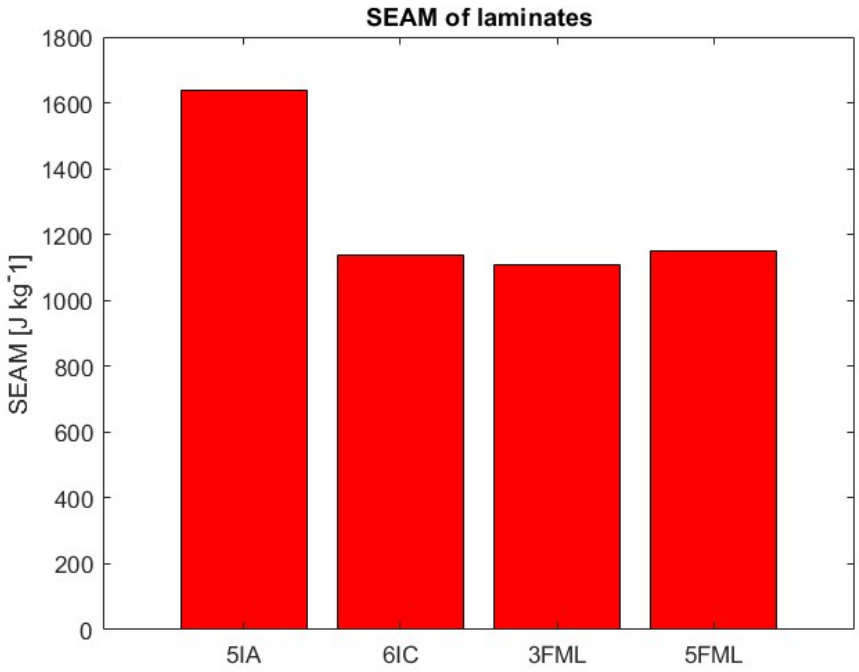

Figure 5.7: Specific energy absorption per unit mass of each material.

Figure 5.8 illustrates the specific energy absorption per unit thickness for different laminates. The advantage of aluminum over other materials in terms of space efficiency is clearly apparent. Aluminum requires less than half the thickness compared to other materials to stop the bullet. This indicates that in applications where thinness is crucial, aluminum outperforms the rest. Another observation is that as the number of aluminum plies in the fiber metal laminate increases, the component can be made even thinner. It is possible that an FML with four aluminum plates could potentially be the thinnest solution after pure aluminum. Carbon, on the other hand, ranks last in terms of slim solutions, suggesting that composites are not the most favorable option for impact energy absorption applications. Although implementing FML may enhance absorption characteristics, aluminum remains the most optimal solution.

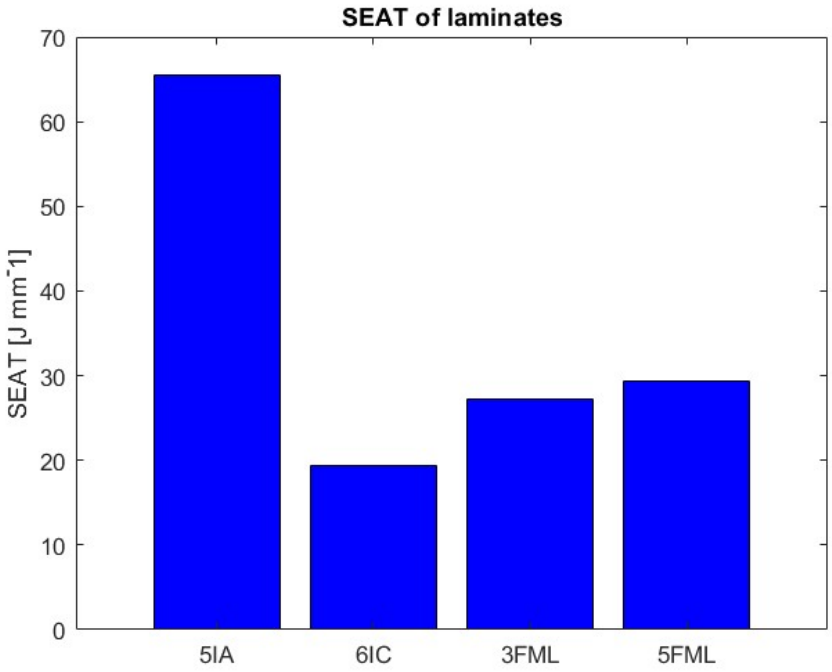

Figure 5.8: Specific energy absorption per unit thickness of each material.

6 | Conclusion and Further Developments

Throughout this work, various objectives were achieved. The primary focus was to determine the most optimal solution for stopping a steel sphere projectile at speeds around 120 m/s through experimental testing. The results demonstrated that aluminum was the superior choice, considering both weight and space-saving considerations. Additionally, the experiments clearly showed that while the FML exhibited better energy absorption compared to the pure carbon specimen, the inclusion of aluminum increased the weight and negated any weight advantages. However, the introduction of aluminum did enhance the material's ductility, potentially resulting in a thinner solution.

These findings indicate that carbon is the least efficient method for energy absorption upon impact. Despite its ability to absorb a significant amount of energy through localized failure, the brittle failure of carbon proves to be less effective compared to the ductile failure observed in aluminum. Although an FML with more aluminum layers could potentially offer a more lightweight and space-saving solution compared to the carbon and previously presented FML configurations, it cannot compete with pure aluminum. This is primarily due to the continuous ductile failure mechanism of aluminum, which outperforms the brittle failure of other materials. Moreover, the imperfect interface of the other constituents, relying on adhesives to transfer energy, further contributes to the inefficiency of alternative solutions.

Despite the initial hypothesis that the FML would exhibit superior energy absorption performance compared to its individual constituents, the existing literature sheds some light on the findings presented here. It should be noted that research comparing the same materials was not available during the time of this study, as most papers primarily focused on glass and aluminum solutions for FML.

Tengfei Liu [32] conducted a study comparing carbon and aluminum laminates subjected to high-velocity impacts. The research concluded that the specific energy absorption of carbon was significantly less efficient than glare, making it inferior in terms of absorbing high-velocity impacts.

Additionally, Jaroslaw et al [12] discussed the low-impact response of glass-aluminum laminate and carbon-aluminum laminates. Their findings revealed that carbon FML exhibited high damage even under low-velocity impact conditions, indicating that it is a less efficient solution compared to glass-based FML.

In the study conducted by Bikakis et al [27], they examined the ballistic response of FML and monolithic metal laminates. The findings indicate that aluminum and glare exhibit similar perforating energy, with GLARE showing slightly better performance in a configuration involving two aluminum layers.

Based on these findings and previous observations, it can be concluded that carbon laminates and carbon-aluminum laminates are expected to perform poorly compared to monolithic aluminum. This conclusion is drawn from the fact that monolithic aluminum already demonstrates performance that is nearly on par with glass-based FML, which has been proven to be significantly superior to carbon laminates.

Therefore, considering the similarities between aluminum and glare as well as the favorable performance of glass-based FML, it can be inferred that carbon-based laminates are likely to exhibit an inferior ballistic response when compared to monolithic aluminum.

The second primary objective of this study was to develop numerical models using LS Dyna for the impact materials. Typically, the common approach to refining a numerical model is to impact a specimen with a defined thickness and vary the impact velocity. However, in this study, the approach was reversed by fixing the threshold speeds and varying the thicknesses of the specimens. This presented a challenge as changing the thickness also affected the stiffness of the model. Consequently, in some cases, multiple models were required for each material, and the model selection depended on the thickness of the specimen.

Despite this challenge, the proposed numerical models were successful in accurately predicting the amount of impact energy absorbed by each laminate up to the threshold thickness, achieving a reasonable level of precision.

This study establishes a foundation for future research in the field of high-velocity impacts on FML. To advance further projects on this subject, the initial step would involve enhancing the current testing rig, particularly the gas gun.

The testing process currently faces certain limitations that hinder smooth operations. Among these limitations, the trigger mechanism of the cannon proved to be the most consistent issue, requiring multiple mountings and dismountings to achieve proper tuning and functionality. Addressing and improving these liabilities in the testing rig would be a crucial next step for future investigations in this area.

In the task of exploring high-velocity impacts, another intriguing focus of research would involve testing different fibers, such as Kevlar, renowned for its exceptional impact resistance, or even glass fiber. Additionally, the metal component could be altered to incorporate more ductile aerospace-grade aluminum or stronger metals like titanium. By examining these alternative fiber and metal combinations, a deeper understanding of the nonlinearities associated with the phenomenon can be achieved.

To gain further insights into the dynamics beyond the threshold speed, a more comprehensive investigation can be conducted. This considers conducting detailed research that may include varying projectile geometries and impact conditions. Such an approach would allow for a more thorough examination of the intricacies involved in high-velocity impacts, providing valuable insights into the behavior of different materials under diverse impact scenarios.

Finally, to enhance the modeling of the materials under investigation, further refinements can be implemented. This includes developing a more sophisticated model using defined user cards in LS-Dyna, which enables greater control and customization of the simulation parameters. Additionally, incorporating cohesive elements into the model would provide a more accurate representation of the adhesive interface between the constituents of the FML. Cohesive elements are known to offer a precise solution for modeling such interfaces.

Furthermore, a more complex model utilizing solid elements could be developed to account for out-of-plane interactions and capture a more detailed comparison of failure mechanisms between experimental and numerical findings. This advanced model would provide deeper insights into the behavior and performance of the materials under various loading conditions.

To evaluate the performance of solid elements, a simulation campaign utilizing aluminum material was conducted. Surprisingly, the results obtained from the simulation aligned significantly better with the experimental results. This finding highlights the potential for developing a more precise model to accurately replicate the impact response. The solid model employed aluminum material that perfectly matched the one used in the characterization campaign.

Formula 6.1 shows the formula to compute the absorbed energy of each panel, making reference to the impact and the residual kinetic energy of the projectile.

$$AbsE = KE_{impact} - KE_{residual} \tag{6.1}$$

Test ID	T $[mm]$	In V $[ms^{-1}]$	Abs E_{sim}[J]	Abs E_{exp}[J]	$Error_{shell}$[%]	$Error_{solid}$[%]
1SA	0.5	50	27.5	27.5	Rebound	Rebound
2SA	0.5	101	57.2	61.3	16.5	6.8
3SA	0.5	118	35	40.5	48	13.5
4SA	2.5	103	116	116	Rebound	Rebound
5SA	2.5	122	169	163	Rebound	1.55
6SA	2.5	144	229	226	36.4	1.45
7SA	2.5	166	113	198	43	Rebound

Table 6.1: Comparison between experimental and numerical aluminum analysis

Based on the results presented in Table 6.1, the solid mesh demonstrates higher accuracy compared to the shell element when compared to the experimental data. An additional investigation incorporating solid aluminum mesh elements into the simulations of FML materials reveals an increase in stiffness. Table 6.2 illustrates the outcomes of this study.

Test ID	T $[mm]$	In V $[ms^{-1}]$	Abs E_{sim}[J]	Abs E_{exp}[J]	$Error_{shell}$[%]	$Error_{solid}$[%]
1SFML	2.7	118	120	79.2	51	15
2SFML	5	117	154.79	135	14	23
3SFML	6.5	127	177.4	177.4	Stuck	Rebound
4SFML	3.5	111	135.5	84.7	Rebound	Rebound
5SFML	5	123	161.4	161.4	Rebound	Rebound
6SFML	8.5	115	147.5	147	Rebound	Rebound

Table 6.2: Comparison between experimental and numerical FML analysis

The composite laminates were initially observed to be composed of thick shell elements, which was not an efficient application of shell elements. To address this issue, an alternative solution was implemented by creating sub-laminates of 1 mm thickness, resulting in more efficient and thinner shell elements. The outcomes of this approach are presented in Table 6.3, demonstrating that the sub-laminate solution yields a weaker but more accurate representation of the behavior of thick laminates compared to the original single laminate solution.

By incorporating these improved modeling techniques, the simulations can significantly enhance accuracy and precision, enabling a more comprehensive analysis and a deeper understanding of the response of FMLs to high-velocity impacts.

Test ID	T $[mm]$	In V $[ms^{-1}]$	Abs E_{sim}[J]	Abs E_{exp}[J]	$Error_{shell}$[%]	$Error_{sub}$[%]
1SC	2.5	118	44	66	22.7	33.3
2SC	4	125	79.4	90.5	0.3	12
3SC	5.3	110	93.2	96	8	3
4SC	7.2	130	149.3	170.8	16.8	12
5SC	8.8	145	173.2	231.27	Rebound	Rebound
6SC	10.5	114	142.2	142.2	Rebound	Rebound

Table 6.3: Comparison between experimental and numerical carbon analysis

X_1^T $[MPa]$	ϵ_x^T	ν_{xy}	E_x $[GPa]$	X_S $[MPa]$	G_{12} $[MPa]$	E_C $[GPa]$	X_1^C $[MPa]$
739.028	0.01319	0.0496	62.154	66.289	3679.3	61.62	489.93

Table 6.4: Comparison between experimental and numerical carbon analysis

E $[GPa]$	σ_f $[MPa]$	σ_y $[MPa]$	ϵ_{pf}
72.3	430.94	334.2	0.1835

Table 6.5: Comparison between experimental and numerical carbon analysis

Bibliography

[1] V. A. Impact tests on aluminium 2024 e t3, aramid and glass reinforced laminates and thermoplastic composites. *Delft*, 1987.

[2] V. A. Low-velocity impact loading on fiber-reinforced aluminum laminates (aral and glare) and other aircraft sheet materials. *Delft*, 1993.

[3] V. A. Impact loading on fiber-metal laminates. *Int J Impact Eng*, 1996.

[4] J. L. A. Matzenmiller and R. L. Taylor. A constitutive model for anisotropic damage in fiber-composites. *Mech. Mater*, 1995.

[5] V. P. A. P. Sharma, S. H. Khan. Experimental and numerical investigation on the uni-axial tensile response and failure of fiber metal laminates. *Composites Part B: Engineering*, 2017.

[6] B. L. A. S. Yaghoubi. Experimental and numerical investigations of stacking sequence effect on glare 5 fml plates subjected to ballistic impact. *Proceedings of the ASME 2012 International Mechanical Engineering Congress and Exposition*, 2012.

[7] H. A. O. R. S. C. C. M. R. F. E. P. A. Tarafdar, G. Liaghat. Quasi-static and low-velocity impact behavior of the bio-inspired hybrid al/gfrp sandwich tube with hierarchical core: Experimental and numerical investigation. *Composite Structures*, 2021.

[8] J. G. A. Vlot. Fiber metal laminates – an introduction. *Kluwer Academic Publisher*, 2001.

[9] C. W. Abdullah MR. The impact resistance of propylene-based fiber metal laminates. *Composites Sci Technol*, 2006.

[10] B. R. Alderliesten RC. Fiber/metal composite technology for future primary aircraft structures. *Structures, Structural Dynamics and Materials Conference*, 2007.

[11] M. S. Alderliesten RC, Benedictus R. Impact resistance of fiber-metal laminates: A review. *International Journal of Impact Engineering*, 2012.

[12] J. P. Bienias Jaroslaw, Surowska Barbara. The comparison of low-velocity impact resistance of aluminum/carbon and glass fiber metal laminates. *Polymer Composites*, 2016.

[13] C. W. Carrillo JG. Scaling effects in the low-velocity impact response of fiber-metal laminates. *J Reinf Plast Comp*, 2008.

[14] J. C. J. N. Compston P, Cantwell WJ. Impact perforation resistance and fracture mechanisms of a thermoplastic-based fiber-metal laminate. *J Mater Sci*, 2001.

[15] C. W. Cortes P. Fracture properties of fiber-metal laminates based on magnesium alloy. *J Mater Sci*, 2004.

[16] C. W. Cortes P. The impact properties of high-temperature fiber-metal laminates. *J Mater Sci*, 2007.

[17] N. E. Dowling. Mechanical behavior of materials: Engineering methods for deformation, fracture and fatigue, third edition. *Choice Reviews Online*, 2007.

[18] A. G. D. E. V. Karpov. Strain and fracture of glass-fiber laminate containing metal layers. *Journal of Applied Mechanics and Technical Physics*, 2018.

[19] A. D. F. Alkhatib, E. Mahdi. Design and evaluation of hybrid composite plates for ballistic protection: experimental and numerical investigations. *Polymers*, 2021.

[20] E. K.-K. R. E.-F. S. A. C. F. Bahari-Sambran, J. Meuchelboeck. The effect of surface modified nanoclay on the interfacial and mechanical properties of basalt fiber metal laminates. *Thin-Walled Structures*, 2012.

[21] M. S. R. B. F. D. Moriniere, R. C. Alderliesten. An integrated study on the low-velocity impact response of the glare fibre-metal laminate. *Composite Structures*, 2013.

[22] T. D. F. Dogan, H. Hadavinia and P. S. Bhonge. Delamination of impacted composite structures by cohesive zone interface elements and tiebreak contact. *Cent. Eur. J. Eng*, 2012.

[23] G. Z. Fan J, Cantwell WJ. The low-velocity impact response of fiber-metal laminates. *J Reinf Plast Comp*, 2010.

[24] K. S. D. B. F.R. Ahad, K. Enakoutsa. Nonlocal modeling in high-velocity impact failure of 6061-t6 aluminum. *International Journal of Plasticity*, 2012.

[25] P. M. G. B. Chai. Low velocity impact response of fibre-metal laminates—a review. *Composite Structures*, 2014.

[26] H. N. N. Y. C. K. J. R. N. G. R. Rajkumar, M. Krishna. Investigation of tensile and bending behavior of aluminum based hybrid fiber metal laminates. *Procedia Materials Science*, 2015.

[27] E. P. S. George S.E. Bikakis, Christos D. Dimou. Ballistic impact response of fiber–metal laminates and monolithic metal plates consisting of different aluminum alloys. *Aerospace Science and Technology*, 2017.

[28] J. Hallquist. Ls-dyna® theory manual. 2006.

[29] R. J. D. H. D. Hoo Fatt MS, Lin C. Ballistic impact of glare fibermetal laminates. *Compos Struct*, 2003.

[30] K. D. C. W. Langdon GS, Nurick GN. Fiber-metal laminate panels subjected to blast loading. *Dynamic failure of materials and structures.*, 2010.

[31] V. E. Liaw BM, Liu YX. Impact damage mechanisms in fiber-metal laminates. *Annual Conference on experimental and applied mechanics*, 2001.

[32] T. Liu. Dynamic damage model of fiber metal laminates under high-velocity impact. *J Fail. Anal. and Preven*, 2021.

[33] L. B. Liu Y. Effects of constituents and lay-up configuration on drop-weight tests of fiber-metal laminates. *Appl Comp Mater*, 2010.

[34] LSTC. Ls-dyna® keyword user's manual iii- version r8.0. 2015.

[35] K. M. R. M. Majzoobi G, Kashfi M. Effect of the projectile nose on high-velocity impact behavior of fiber metal laminates. *Polym. Compos.*, 2022.

[36] D. L. Mitar Mišović, Nebojša Tadić. Deformation characteristics of aluminium alloys. *Građevinar*, 2016.

[37] N. K. Naik and P. Shrirao. Composite structures under ballistic impact. *Composite Structures*, 2004.

[38] D. C. P. C. O. Cousigné, D. Moncayo and H. Naceur. Numerical modeling of nonlinearity, plasticity and damage in cfrpwoven composites for crash simulations. *Compos. Struct*, 2014.

[39] W. J. C. P. Cortes. The prediction of tensile failure in titanium-based thermoplastic fibre-metal laminates. *Composites Science and Technology*, 2006.

[40] F. D. M. R. M. H. P. Feraboli, B. Wade and A. Byar. Lsdyna mat54 modeling of the

axial crushing of a composite tape sinusoidal specimen. *Compos. Part A Appl. Sci. Manuf*, 2011.

[41] S. F. C. Y. Y. J. Y. P. He, M. Huang. Effects of primer and annealing treatments on the shear strength between anodized ti6al4v and epoxy. *International Journal of Adhesion and Adhesives*, 2015.

[42] F. H. S. R. R. Fedele, B. Raka. Identification of adhesive properties in glare assemblies using digital image correlation. *Journal of the Mechanics and Physics of Solids*, 2009.

[43] J. B. P. J. K. M. R. J. Mania, Z. Kolakowski. Comparative study of fml profiles buckling and postbuckling behaviour under axial loading. *Composite Structures*, 2015.

[44] R. A. R. Rodi and R. Benedictus. An experimental approach to investigate detailed failure mechanisms in fibre metal laminates. *Springer*, 2009.

[45] K. H. Reyes G. Mechanical behavior of lightweight thermoplastic fiber metal laminates. *J Mater Processing Technol*, 2007.

[46] G. Roebroeks. Towards glare: The development of fatigue insensitive and damage tolerant aircraft material. *PhD Thesis*, 1991.

[47] A. S. Impact on composite structures. *Cambridge University Press*, 1998.

[48] M. H. K. S. S. Hinz, T. Omoori. Damage characterization of fiber metal laminates under interlaminar shear load. *Composite Parts*, 2009.

[49] S. T. A.-F. S. M. Goushegir, J. F. Dos Santos. Influence of aluminum surface pre-treatments on the bonding mechanisms and mechanical performance of metal-composite single-lap joints. *Welding in the World*, 2017.

[50] A. R. S. M. B. R. Sadighi M, Parnanen T. Experimental and numerical investigation of metal type and thickness effects on the impact resistance of fiber-metal laminates. *Appl Composite Mater*, 2012.

[51] H. v. L. G. v. G. Schijve, J. and A. Hoeymakers. Fatigue properties of adhesive-bonded laminated sheet material of aluminium alloys. *Engn. Fracture Mechanicse*, 1979.

[52] A. R. Schut J. Delamination growth rate at low and elevated temperatures in glare. *25th International congress of the aeronautical sciences*, 2006.

[53] L. B. Seyed Yaghoubi A, Liu Y. Low-velocity impact on glare 5 fiber-metal laminates: influences of specimen thickness and impactor mass. *J Aerospace Eng*, 2012.

[54] A. Standards. Astm d3039: Standard test method for tensile properties of polymer matrix composite materials. 2002.

[55] L. Vogelesang. The development of a new family of hybrid materials. *19th Plantema Memorial Lecture*, 2003.

[56] R. J. H. Wanhill. Glare: A versatile fibre metal laminate (fml) concept. *NLR Emmeloord*, 2017.

[57] J. WS. Impact and residual fatigue behaviour of arall and as6/5245 composite materials. *NASA Technical Memorandum*, 1986.

[58] A. B. N. Z. W.-G. L. X. Li, M. Y. Yahya. Dynamic failure of fibre-metal laminates under impact loading - experimental observations. *Journal of Reinforced Plastics and Composites*, 2015.

[59] M. E. B. X. Xiao and N. L. Johnson. Axial crush simulation of braided carbon tubes using mat58 in ls-dyna. *Thin-Walled Struc*, 2009.

[60] L. R. X. L. Y. Chen, G. Liao. Damage tolerance of glare laminates subjected to high-velocity impact. *Acta Aeronautica et Astronautica Sinica*, 2018.

[61] Q. H. Z. Z. Y. Chen, L. Chen. Effect of metal type on the energy absorption of fiber metal laminates under low-velocity impact. *Mechanics of Advanced Materials and Structures*, 2021.

[62] Y. S. S. L. W. W.-J. T. Y. Xu, H. Li. Improvement of adhesion performance between aluminum alloy sheet and epoxy based on anodizing technique. *International Journal of Adhesion and Adhesives*, 2017.

[63] H. W. Yizhe C., Yichun W. Research progress on interlaminar failure behavior of fiber metal laminates. *Advances in Polymer Technology*, 2019.

A | Appendix A

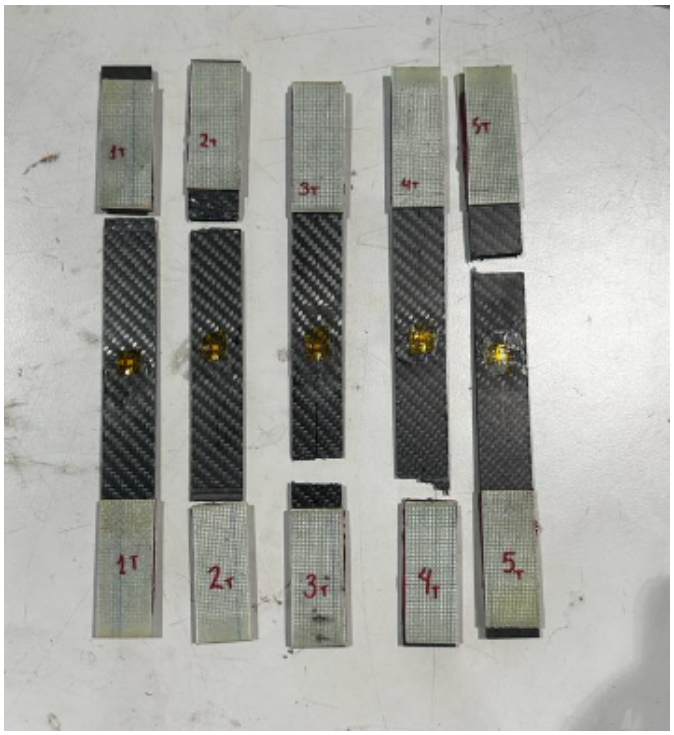

Figure A.1: Failure of tensile specimens

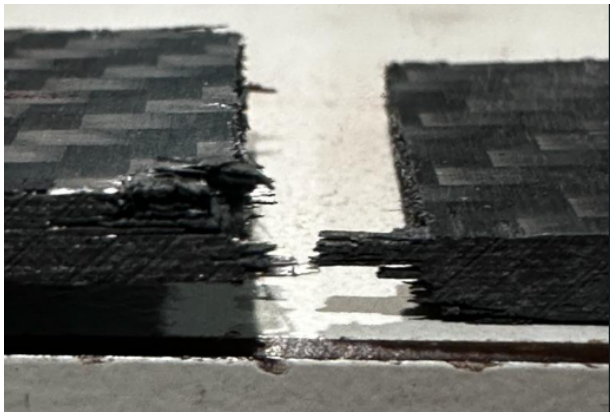

Figure A.2: Close up of failed tensile specimens

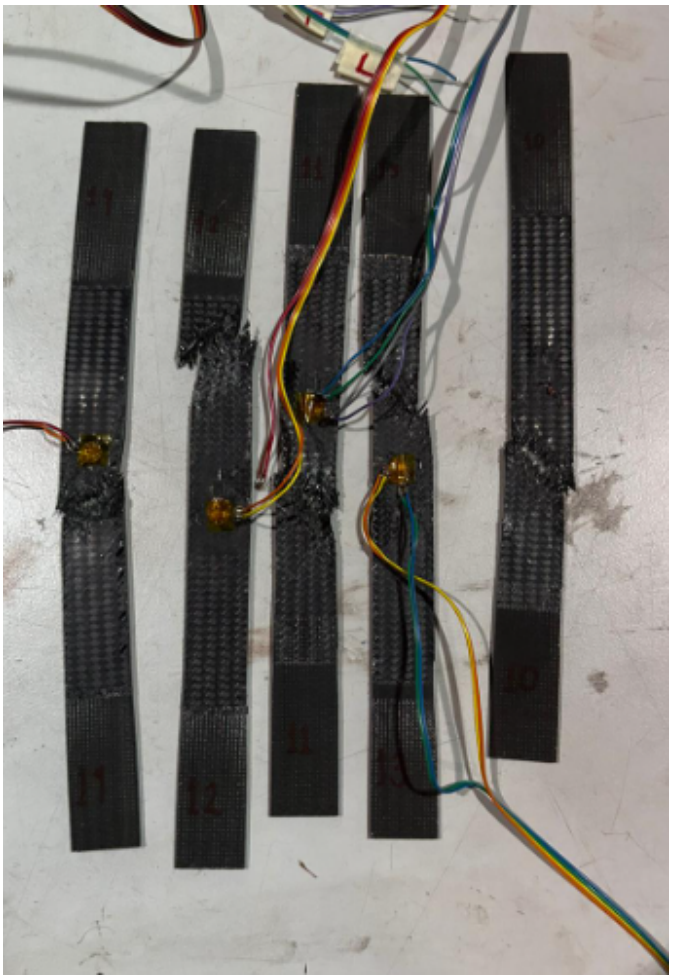

Figure A.3: Failure of shear specimens

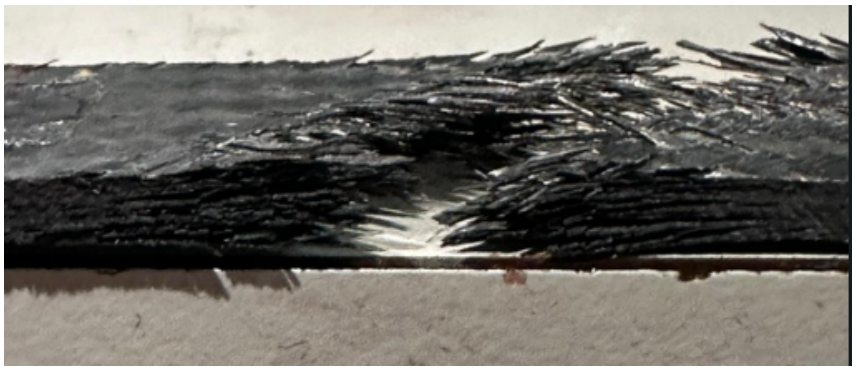

Figure A.4: Close up of failed shear specimens

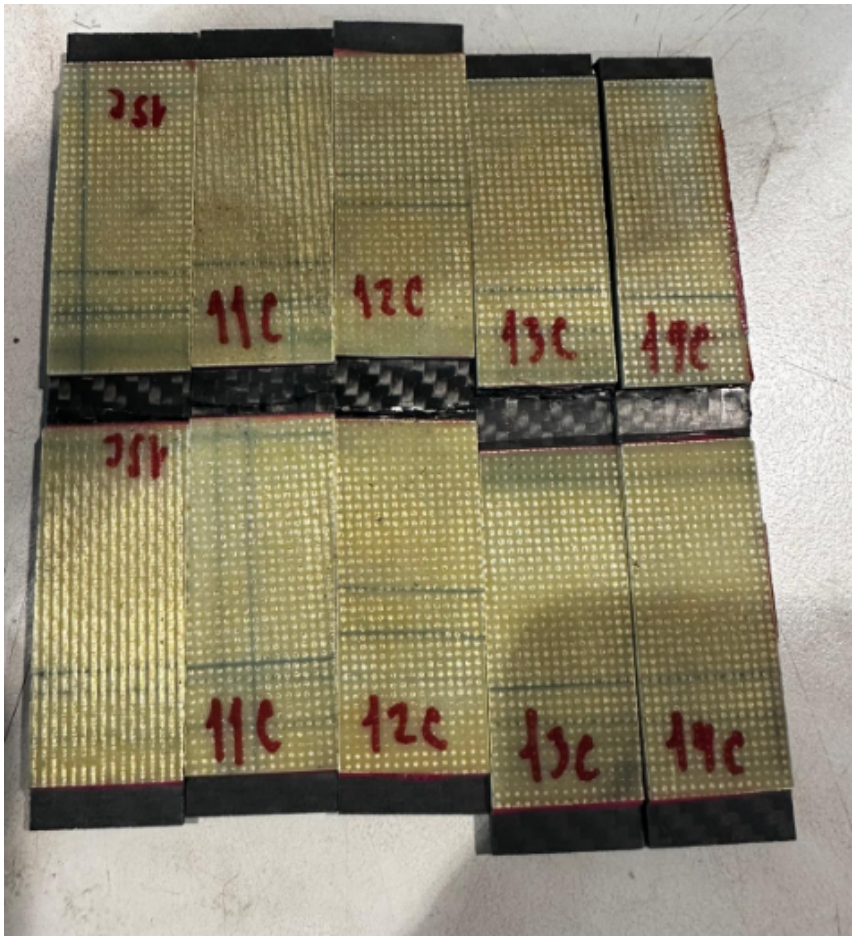

Figure A.5: Failure of compression specimens

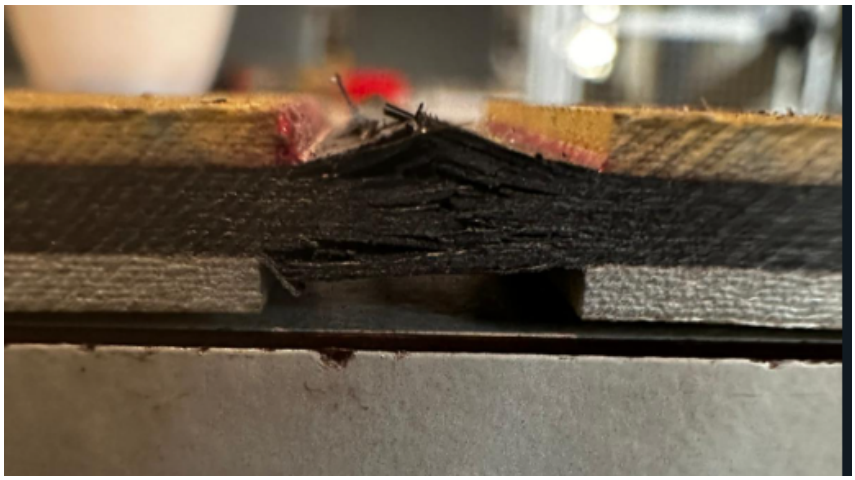

Figure A.6: Close up of failed compression specimens

B | Appendix B

Figure B.1: Aluminum specimen mounted on machine

Figure B.2: Comparison failed specimen with undamaged specimen

Figure B.3: Ductile failure of aluminum specimens

C | Appendix C

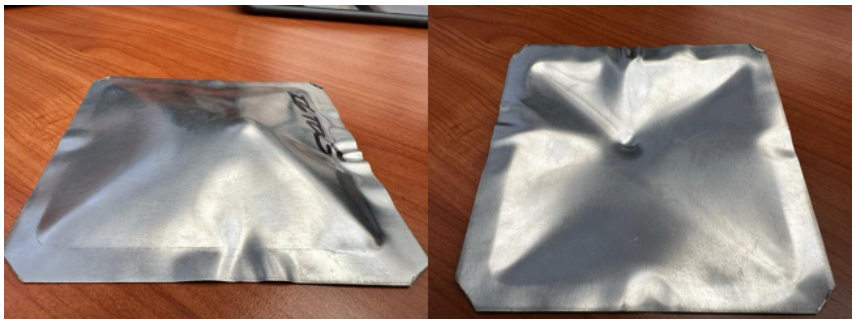

Figure C.1: Impact Specimen 1IA

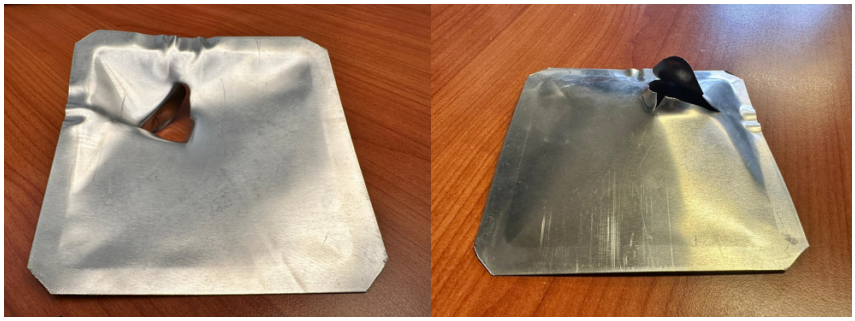

Figure C.2: Impact Specimen 2IA

Figure C.3: Impact Specimen 3IA

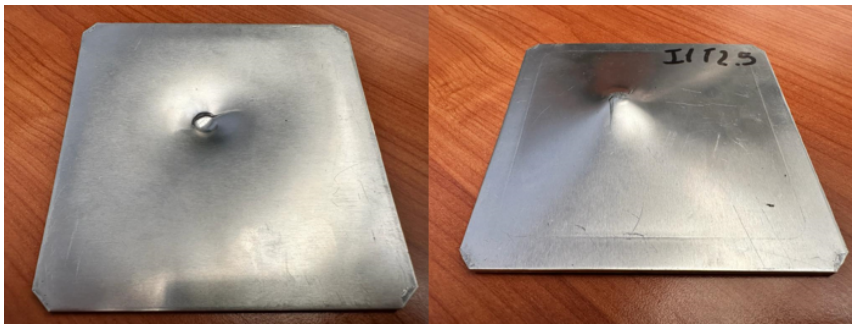

Figure C.4: Impact Specimen 4IA

Figure C.5: Impact Specimen 5IA

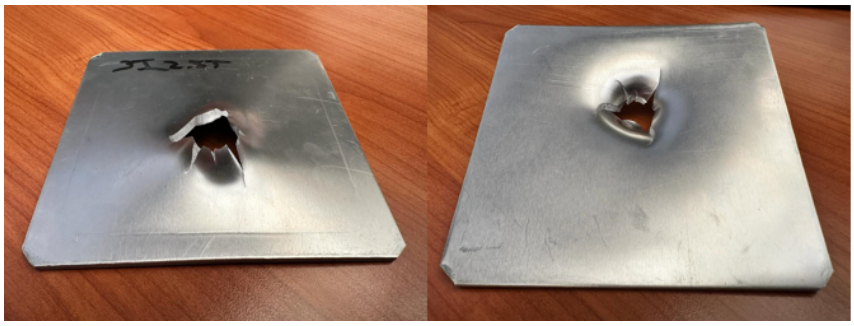

Figure C.6: Impact Specimen 6IA

Figure C.7: Impact Specimen 7IA

D | Appendix D

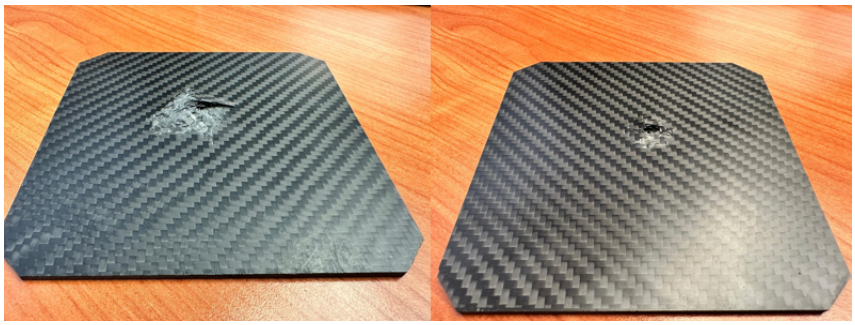

Figure D.1: Impact Specimen 1IC

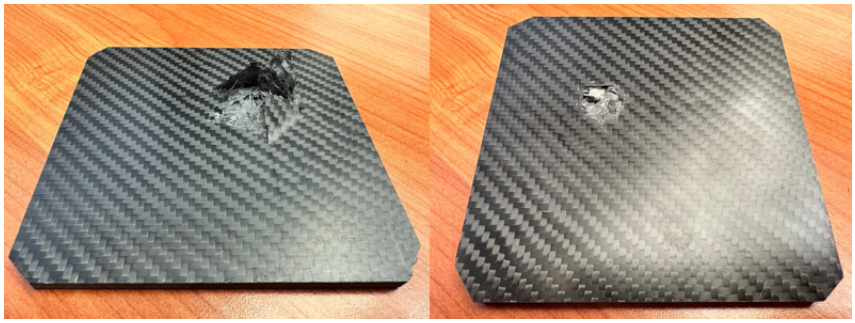

Figure D.2: Impact Specimen 2IC

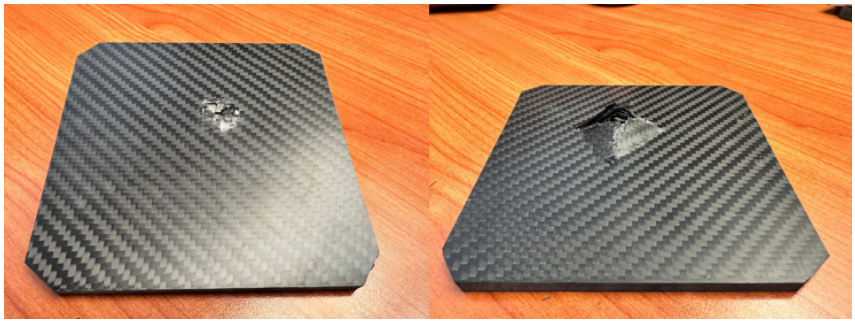

Figure D.3: Impact Specimen 3IC

Figure D.4: Impact Specimen 4IC

Figure D.5: Impact Specimen 5IC

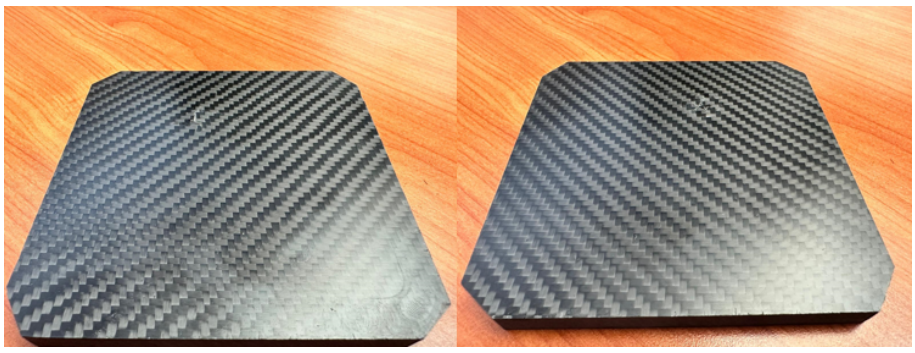

Figure D.6: Impact Specimen 6IC

E | Appendix E

Figure E.1: Impact Specimen IFML1

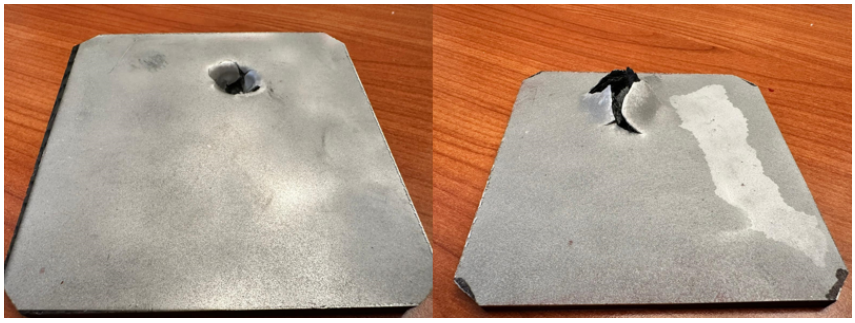

Figure E.2: Impact Specimen IFML2

Figure E.3: Impact Specimen IFML3

Figure E.4: Impact Specimen IFML4

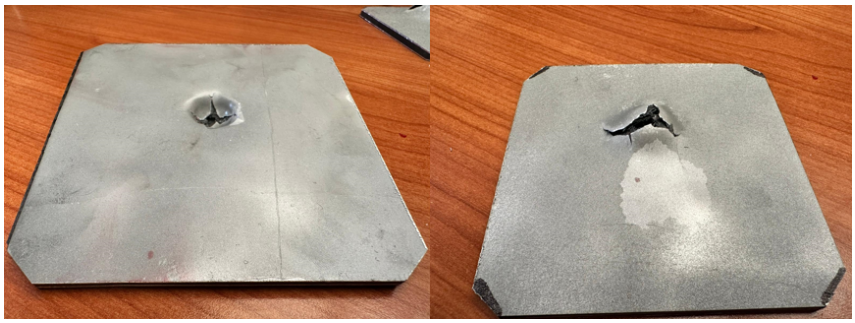

Figure E.5: Impact Specimen IFML5

Figure E.6: Impact Specimen IFML6

F | Appendix F

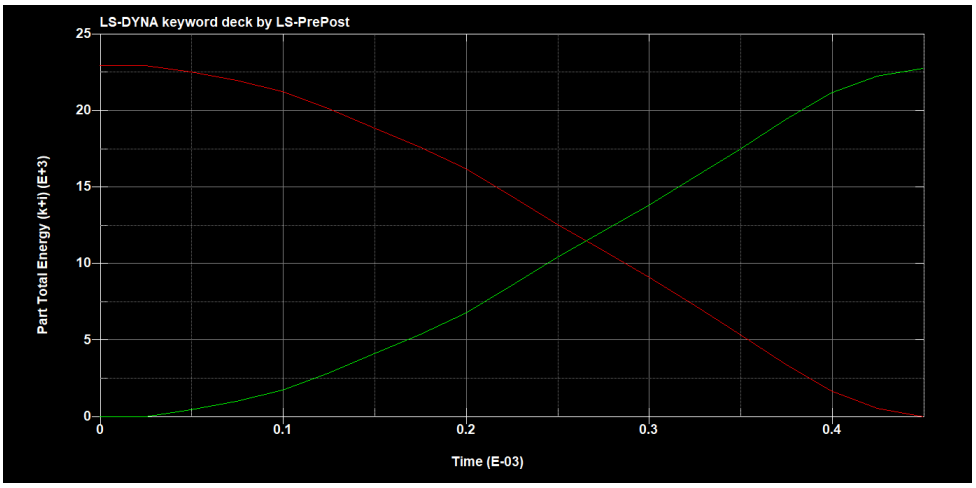

Figure F.1: Energy absorption 1SA

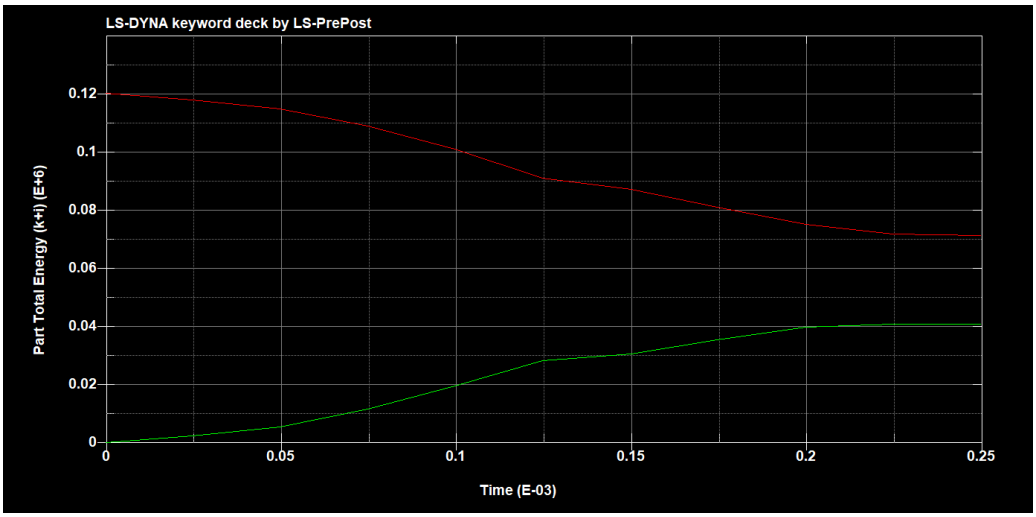

Figure F.2: Energy absorption 2SA

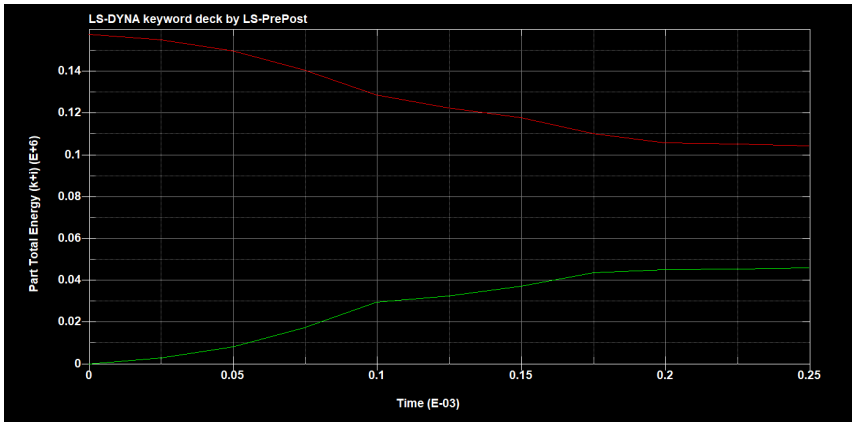

Figure F.3: Energy absorption 3SA

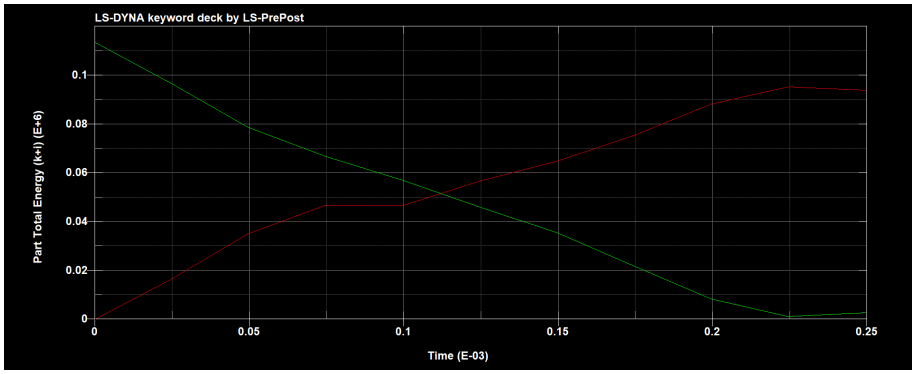

Figure F.4: Energy absorption 4SA

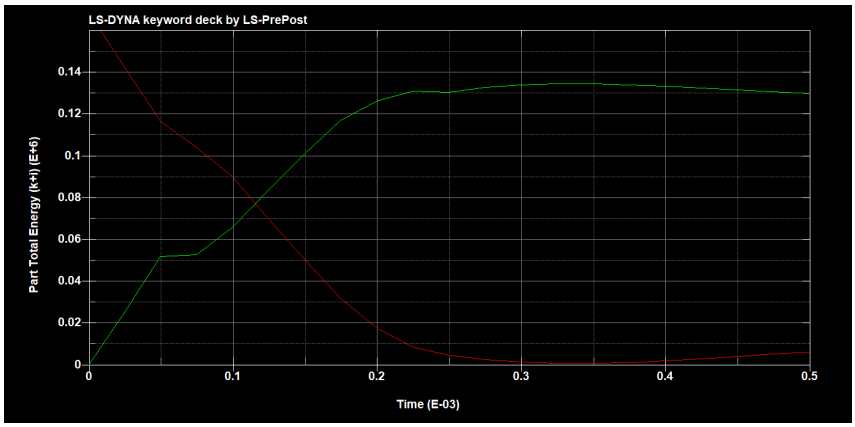

Figure F.5: Energy absorption 5SA

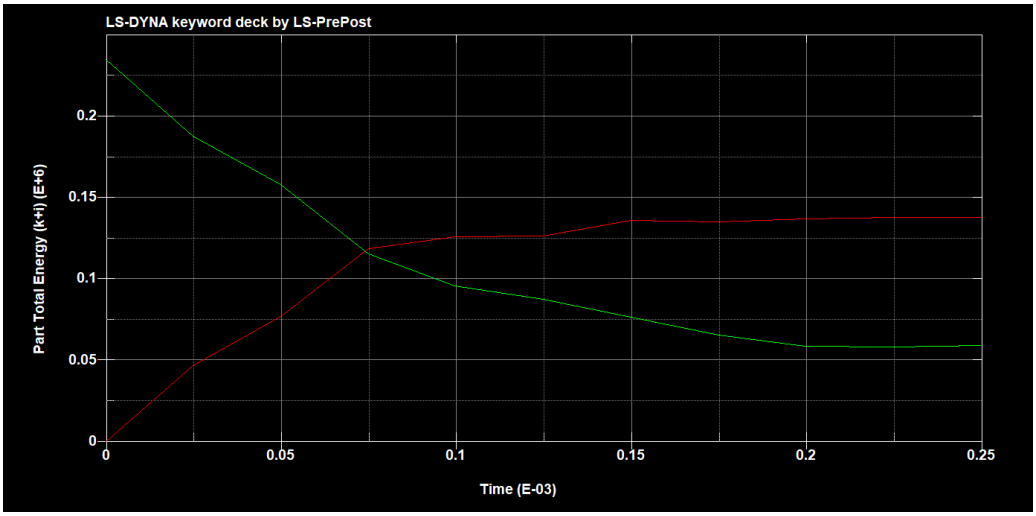

Figure F.6: Energy absorption 6SA

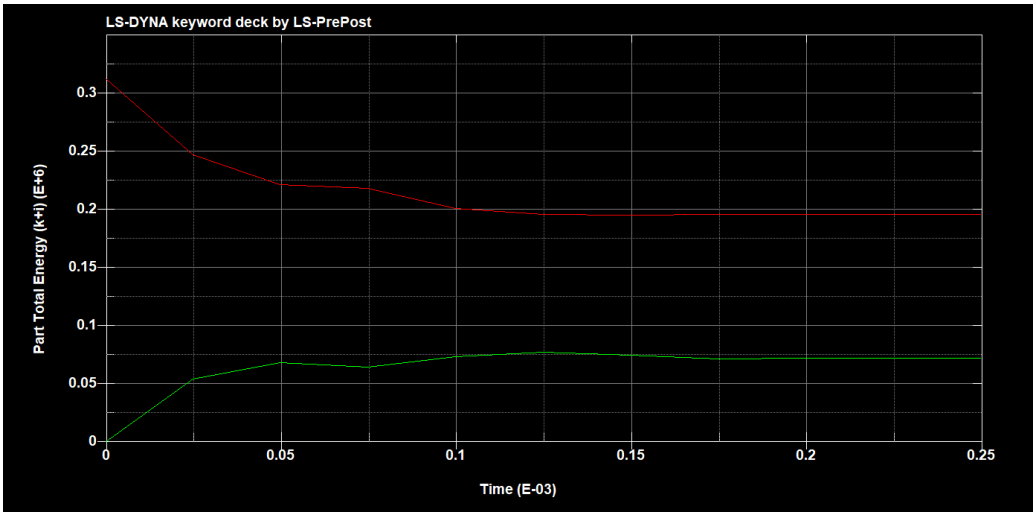

Figure F.7: Energy absorption 7SA

G | Appendix G

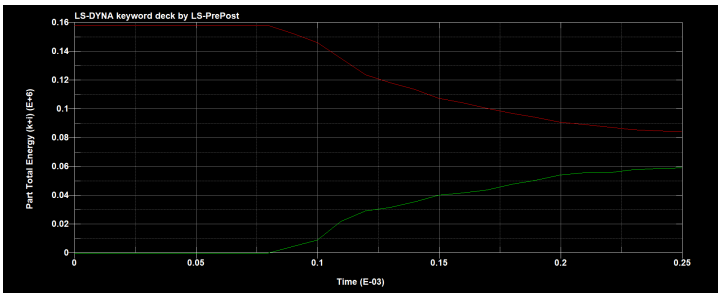

Figure G.1: Energy absorption 1SC

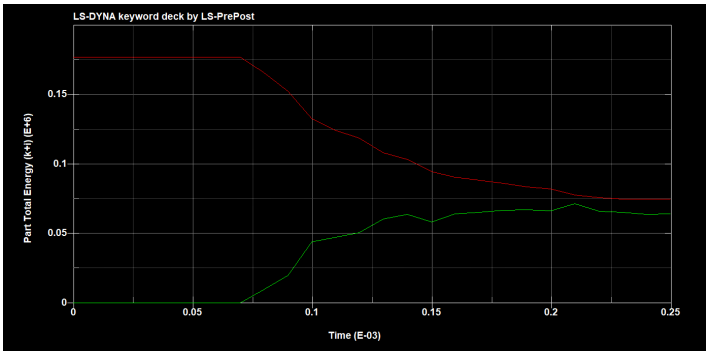

Figure G.2: Energy absorption 2SC

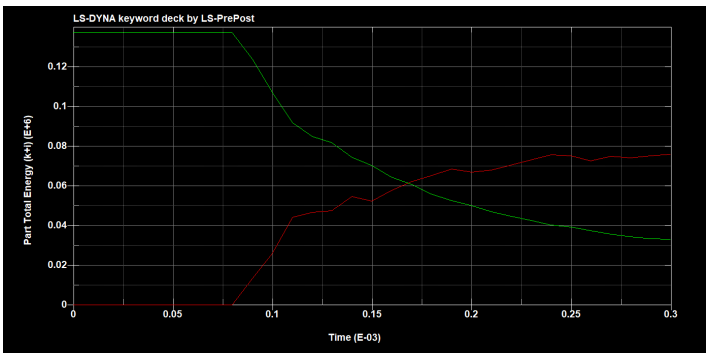

Figure G.3: Energy absorption 3SC

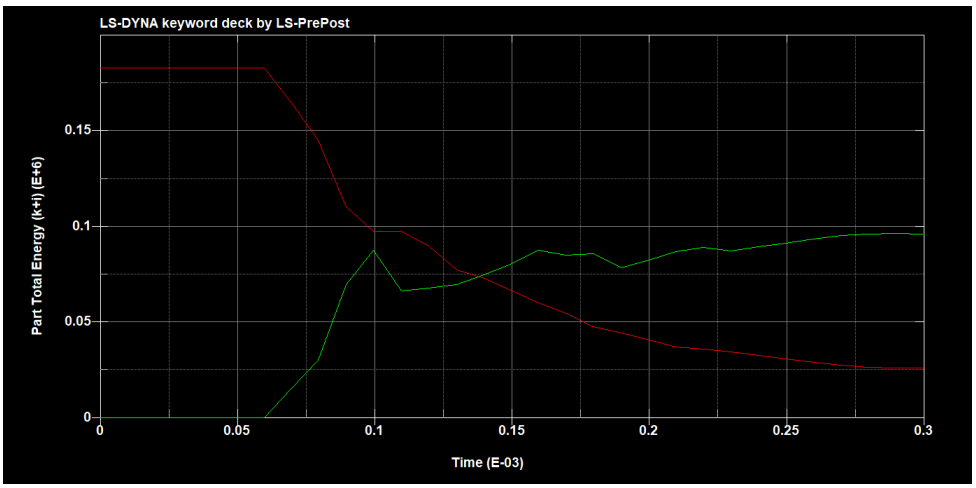

Figure G.4: Energy absorption 4SC

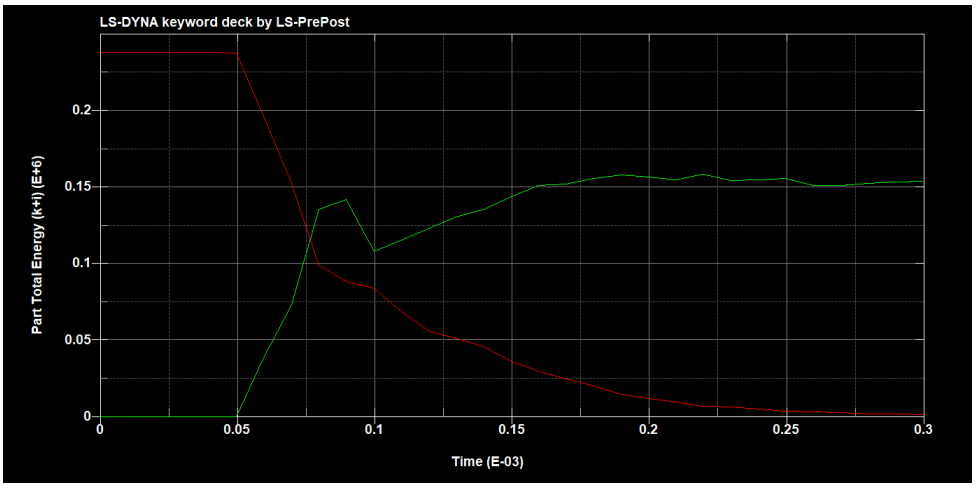

Figure G.5: Energy absorption 5SC

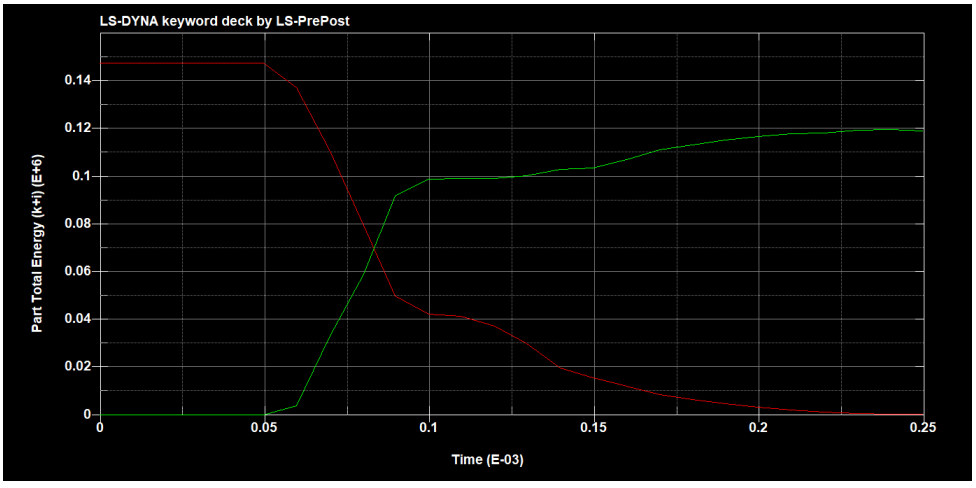

Figure G.6: Energy absorption 6SC

H | Appendix H

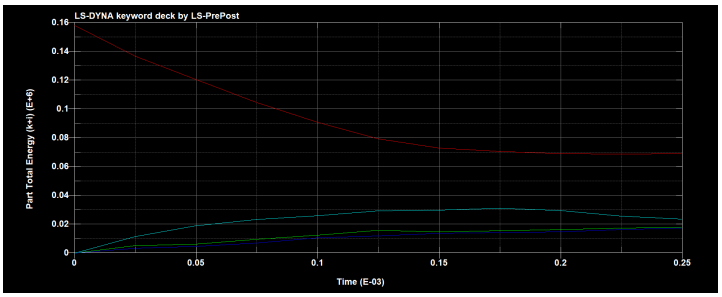

Figure H.1: Energy absorption 1SFML

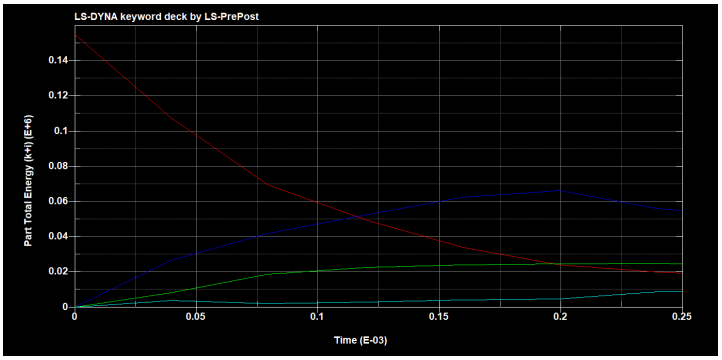

Figure H.2: Energy absorption 2SFML

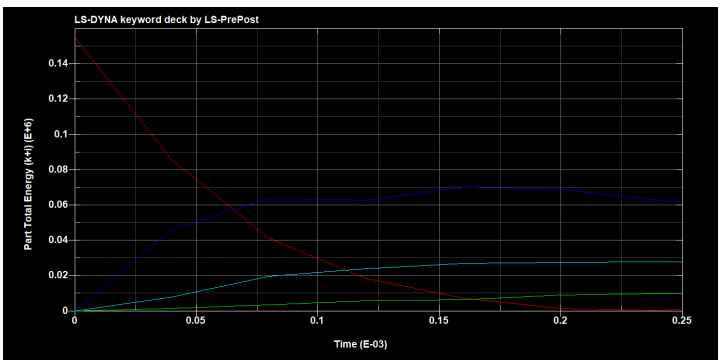

Figure H.3: Energy absorption 3SFML

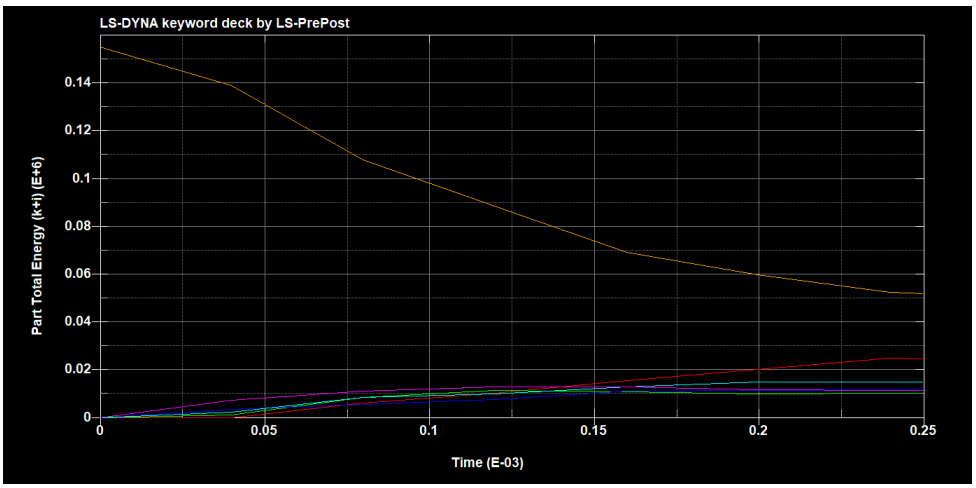

Figure H.4: Energy absorption 4SFML

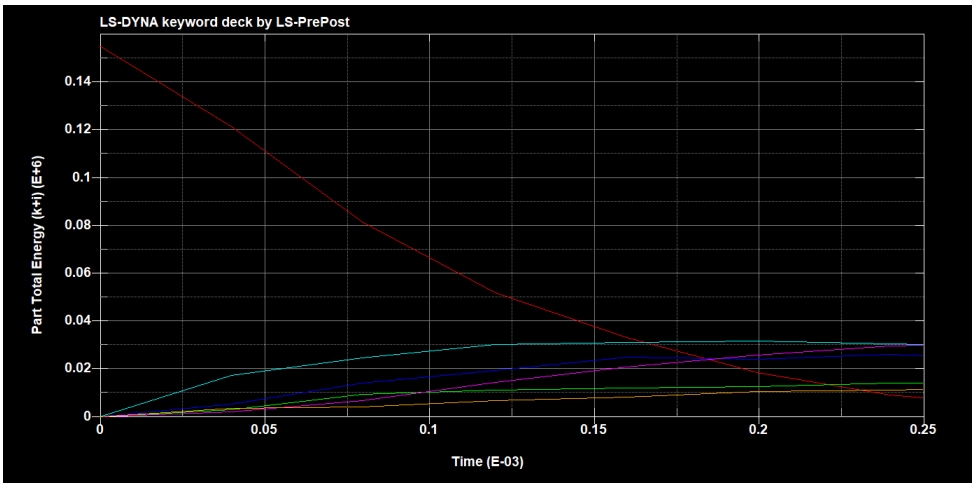

Figure H.5: Energy absorption 5SFML

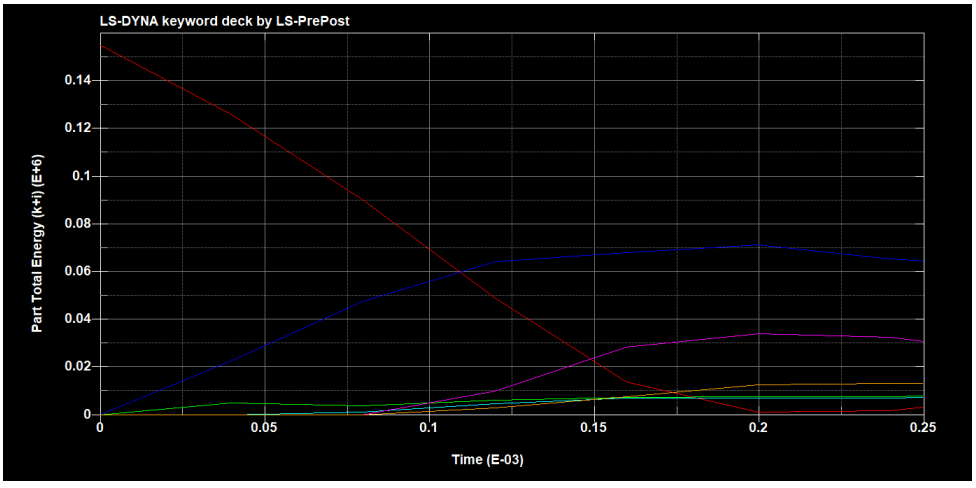

Figure H.6: Energy absorption 6SFML